Earth Surface Processes and Landforms

Aeolian dust accretion outpaces erosion in the formation of Mediterranean alpine soils. New evidence from the periglacial zone of Mount Olympus, Greece

Journal:	*Earth Surface Processes and Landforms*
Manuscript ID	ESP-23-0109.R1
Wiley - Manuscript type:	Case Study
Keywords:	alpine soil, aeolian dust accretion, periglacial erosion, mineral weathering, Mount Olympus

Abstract:	Soil formation in Mediterranean periglacial landscapes remains poorly understood as the interplay between erosion and aeolian dust accretion in providing parent materials, and mineral weathering and pedogenesis, as dominant post depositional processes, depends on a variety of local and regional factors. Herein, we investigate the balance between erosion and aeolian dust accretion in the formation of an alpine soil profile along an erosional gradient in the periglacial zone of Mount Olympus in Greece. We applied a wide range of analytical methods to 23 samples, from a soil profile developed in a glaciokarstic plateau, from colluvial sediment horizons interbedded in postglacial scree slopes and from modern Sahara dust samples deposited on the snowpack. Colluvial sediment horizons exhibit high concentrations of calcite rich sand and represent the local erosion products. The soil B horizon developed on a glaciokarstic plateau contains high amounts of fine earth and is rich in quartz, mica, plagioclase, clays, and Fe-Ti oxides. Based on its physical and textural characteristics the soil profile is partitioned in a surficial weathered Bw and a lower illuvial Bt horizon that overlies the local regolith composed of fragmented glacial till and slope wash deposits. Radiogenic isotope systematics, textural and mineralogical analysis show that the contribution of Sahara and locally sourced dust to the development of the soil B horizon ranges between 50 and 65%. Cryoturbation results in fine earth translocation from Bw to the Bt horizon, whereas weak pedogenetic modifications of aeolian and bedrock-derived minerals result in magnetic mineral weathering and secondary clay formation. Our findings reveal that, aeolian dust accretion is the dominant process in providing alpine soil parent material and that cryoturbation, weak pedogenesis, and clay mineral alteration occur within the Mediterranean periglacial zone of Mount Olympus.

Aeolian dust accretion outpaces erosion in the formation of Mediterranean alpine soils. New evidence from the periglacial zone of Mount Olympus, Greece

Abstract

Soil formation in Mediterranean periglacial landscapes remains poorly understood as the interplay between erosion and aeolian dust accretion in providing parent materials, and mineral weathering and pedogenesis, as dominant post depositional processes, depends on a variety of local and regional factors. Herein, we investigate the balance between erosion and aeolian dust accretion in the formation of an alpine soil profile along an erosional gradient in the periglacial zone of Mount Olympus in Greece. We applied a wide range of analytical methods to 23 samples, from a soil profile developed in a glaciokarstic plateau, from colluvial sediment horizons interbedded in postglacial scree slopes and from modern Sahara dust samples deposited on the snowpack. Colluvial sediment horizons exhibit high concentrations of calcite rich sand and represent the local erosion products. The soil B horizon developed on a glaciokarstic plateau contains high amounts of fine earth and is rich in quartz, mica, plagioclase, clays, and Fe-Ti oxides. Based on its physical and textural characteristics the soil profile is partitioned in a surficial weathered Bw and a lower illuvial Bt horizon that overlies the local regolith composed of fragmented glacial till and slope wash deposits. Radiogenic isotope systematics, textural and mineralogical analysis show that the contribution of Sahara and locally sourced dust to the development of the soil B horizon ranges between 50 and 65%. Cryoturbation results in fine earth translocation from Bw to the Bt horizon, whereas weak pedogenetic modifications of aeolian and bedrock-derived minerals result in magnetic mineral weathering and secondary clay formation. Our findings reveal that, aeolian dust accretion is the dominant process in providing alpine soil parent material and that cryoturbation, weak pedogenesis, and clay mineral alteration occur within the Mediterranean periglacial zone of Mount Olympus.

Keywords: alpine soil; erosion; aeolian dust accretion; mineral weathering; Mediterranean periglacial zone, Mount Olympus

1. INTRODUCTION

Global glacier retreat and the melting of permafrost and ground ice have altered the dynamics of the alpine critical zone by enhancing erosion and by disturbing the production of mountain soils (Haeberli et al., 2006, Egli et al., 2014). During periods of glacial retreat and paraglacial adjustment, alpine soils develop from parent materials sourced through a combination of frost shattering, colluvial activity, and hillslope outwash (Egli and Poullenard, 2016). An equally important factor that affects the formation and evolution of alpine soils is the accretion of local and long-range transported aeolian dust (Muhs and Benedict, 2006; Küfmann 2008; Lawrence et al., 2013; Drewnik et al., 2014; Yang et al., 2016; Gild et al., 2018; Munroe et al., 2019). Thus, the contributions of physical erosion and aeolian dust accretion are fundamental sources of alpine soil parent material and largely define their textural, mineralogical, and geochemical characteristics.

The postglacial adjustment of alpine valleys is inherently linked to high rates of erosion, with frequent rockfalls, debris flows, rock avalanches, and high rates of sediment production especially below steep rockwalls. In such dynamic environments, alpine soil mantles formed on the surface of slope deposits are patchy, often truncated and constantly rejuvenated from rockfall material, whereas the evolution of these soils alternates between progressive and regressive phases (Egli et al., 2018). Similar soil mantles developed on sandy layers deposited on the surface of stratified scree slopes are generally indicative of quiescent periods of slope processes and are thus concise indicators of optimum climatic conditions and alpine landscape stability (Sanders et al., 2010). When the regional climate shifts to a colder regime, intense freeze–thaw activity and frost cracking enhance rockfall activity and result in the erosion and gradual burial of these incipient soil mantles. As hillslope processes and scree slope aggradation diminish away from the alpine steep rockwalls, the development of alpine soils on distal moraines, outwash plains, and glacially scoured plateaus can be considered continuous (*sensu lato*). In these depositional environments, low erosional rates provide ample time for pedogenetic processes such as chemical weathering, mineral alteration, elemental translocation, and illuviation to occur, whereas other physical processes, such as cryoturbation disturb the soil profiles. Alpine soils are an important component of high mountain ecosystems, so a better understanding of the processes that drive their formation in climatically sensitive regions, like the Mediterranean, is required.

Most soils formed in the Mediterranean basin display a distinguishable red color (terra rossa) that derives from high concentrations of ultra-fine pedogenic iron oxides, mainly hematite (Yaalon, 1997; Durn et al., 1999). Terra rossa soils receive significant aeolian dust additions from Sahara and Sahel regions (Yaalon, 1997; Durn, 2003; Stuut et al., 2009). In the Mediterranean alpine hinterland, thin drapes of Sahara-dust-rich soils are found on plateaus, glacial moraines, and outwash plains (e.g., Rellini et al., 2009), whereas aeolian dust accretion in terra rossa soils can also originate from a wide range of alluvial deposits, such as sand dunes, desiccated alluvial planes, and Quaternary loess (Amit et al., 2020; Lehmkuhl et al., 2020). Most of the Mediterranean mountains are built up by carbonate rocks, hence the aeolian input to alpine soil formation occurs in parallel with colluvial deposition of carbonate erosion and dissolution products that form a characteristic insoluble residue incorporated in the soil sequences (Durn 2003; Varga et al., 2016; Kirsten and Heinrich, 2022).

In the present study, we investigate the major processes that drive the postglacial formation of Mediterranean alpine soils in the periglacial landscapes of Mount Olympus, Greece. We follow a combined sedimentological, mineralogical, and isotopic approach, and present a detailed characterization of distinct alpine sediment and soil horizons developed across a geomorphological gradient of decreasing erosive power. Discrete sediment samples from intact sandy layers interbedded in postglacial stratified scree slope deposits that represent *in situ* erosional products of the periglacial zone of Mount Olympus, are compared with samples from a soil profile developed in a glaciokarstic plateau, with a goal to assess the relative contributions of aeolian dust accretion to the fine fraction of an alpine soil. We differentiate between the physical and chemical processes that drive the production of the scree slope sandy layers and of the alpine soil profile, by comparing their respective grain size distributions, and bulk mineralogy. Furthermore, we examine the potential influence of Sahara and locally sourced aeolian dust accretion on the alpine soil profile by comparing the sedimentological, mineralogical, and radiogenic isotope compositions through the application of $^{86}Sr/^{87}Sr$ and $^{143}Nd/^{144}Nd$ ratios between the soil samples and Sahara dust samples collected from the snowpack. We finally measured the magnetic properties of the soil samples and clay mineralogy of bottom and topsoil layers, to assess the potential for weathering of clay minerals and iron oxides within Mount Olympus periglacial zone. Understanding the sources of parent materials and soil formation processes between contrasting geomorphological settings is a fundamental step towards defining the postglacial paleo-environmental history of Mount Olympus alpine landscapes that followed pronounced shifts of the regional climate.

2 BACKGROUND

2.1 Mount Olympus glacial history

Mount Olympus is the highest mountain in Greece, rising 2918 m above the northwest coastline of the Aegean Sea (Figure 1a). It is a precipitous massif with a circular shape composed of Triassic to Cretaceous metacarbonates, uplifted along a frontal fault that runs parallel to the present-day shoreline. Mount Olympus is exhumed from the silicate crystalline bedrock, which dominates the lithology of Pieria Mountains (granites, ophiolites) to the north and east, and Mount Olympus granites to the west (Figure 1B). High uplift rates along with successive Quaternary glaciations have created the present-day rugged terrain. The deglaciation of Mount Olympus since the Last Glacial Maximum (LGM), between 28 and 24 ka BP (Allard et al., 2020), triggered the rapid retreat of an ice cap that was covering the summit area and extended down to elevations of □1800 m (Kuhlemann et al., 2008). The post-LGM glacier retreat was intercepted by a glacier re-advance phase at □15 ka BP that was limited at the highest cirques above 2200 m at □12.5 ka BP (Styllas et al., 2018). This latter phase of glacial expanse is traced in both Megala Kazania (MK) and Throne of Zeus (TZ) cirques (Figure 1C). The absence of absolutely dated glacial features between early- and mid-Holocene (9–4 ka BP) in both cirques suggests reduced glacial activity, whereas Late Holocene (4 ka BP to present) glacier advances have been observed only in the MK cirque (Figure 1C). These include a terminal moraine stabilization phase at □2.5 ka BP followed by a smaller expansion of the MK glacier at the beginning of the Little Ice Age (LIA) at □0.6 ka BP (Styllas, 2020). Late Holocene glacier advances in the MK cirque lack similarly dated glacial landforms in the TZ cirque, but we cannot rule out the possibility that the Late Holocene climatic shifts towards glacial conditions triggered an intensification of glacial and periglacial processes, which in turn affected the late Holocene landscape evolution, scree slope aggradation and alpine soil production.

2.2 Climate

The contemporary maritime conditions and the steep relief of Mount Olympus result in intense precipitation and temperature altitudinal gradients, with the highest peaks constituting an orographic and climatic barrier between the eastern (marine) and western (continental) sides (Figure 1b, Styllas and Kaskaoutis, 2018). The climate in the coastal zone is typically Mediterranean, whereas at higher elevations (1000–2200 m), the climate attains sub-Mediterranean characteristics with average annual precipitation of 1300 mm (Styllas et al., 2016). In the alpine zone above the tree line (2400 m), the climate is characterized by temperate conditions with annual precipitation above 2000 mm and average annual temperatures between 0 and 1.5 °C (Styllas et al., 2016). The periglacial activity in the Mount Olympus alpine zone is likely still active today, as it is situated just above the lower limit of the regional permafrost zone (2700m) of the southern Balkan peninsular (Dobiński, 2005).

2.3 The Plateau of Muses

The Plateau of Muses (PM) is a planar depositional surface located at an elevation of 2600 m with a surface area of 1 km^2. It resembles a typical alpine meadow, partly covered by alpine grass vegetation that shares similar characteristics with plateaus found in the high Balkan Mountains and the European Alps. The PM is bounded to the south by the TZ cirque lateral moraine ridge and by several gentle-sloping glacially eroded peaks along its northern, eastern, and western margins (Figure 1C). The formation of the plateau has resulted from the combined action of glacial scouring and carbonate bedrock dissolution. Its low relief in combination with the circular shape suggest a doline type karstic depression that is filled with glacial till, overlain by colluvial sediments (slope wash) transported from the adjacent slopes. The surface layer of the PM sedimentary sequence comprises a developed soil sequence with variable thickness (30–50 cm) that overlies a layer of outwash sand and fine gravels and/or fragmented till boulders, and exhibits brown-red to yellow color hues, which in the Munsell color scale range between 7.5 and 10 YR (Table 1). Alternating patches of alpine grass vegetation and hummocky soil pans in the center of the plateau are indicative of periglacial activity and cryoturbation. Other periglacial features such as solifluction-terraced stripes below the bare bedrock of the surrounding summits are tentatively considered to have formed during the Late Holocene cold stages, during the observed expansion of small glaciers in the MK cirque.

3 MATERIALS AND METHODS

3.1 Erosional products and alpine soil sampling

To adequately address the question of the relative balance between aeolian dust accretion and local erosion of moraines and scree slopes to the development of the alpine soil on Mount Olympus periglacial zone, a wide range of methods were employed and involved the analyses of 21 discrete soil and sediment samples retrieved along a transect of decreasing hillslope energy and erosional power (Figure 2). Five samples (n=5) were retrieved from clast-free sandy horizons interbedded in the relatively young (Late Holocene) MK and older (early Holocene) TZ stratified scree slopes, and sixteen (n=16) were sampled from the PM soil sequence at 2-cm intervals (Table 1). The specific experimental setting was selected to evaluate the impact of physical weathering on providing the base material for the development of the PM soil. We only sampled naturally exposed clast free sandy layers found within the scree slopes of MK and TZ. We considered that these layers share similar textural, mineralogical, and geochemical characteristics with the PM soil basal horizon, which lies on a layer of outwash sand and gravels. Luckily, we were able to retrieve the samples from two distinct interbedded clast free sediment layers within the TZ scree slope after a torrential rainfall event that opened a deep erosional trench in the scree below the rockwall and reached the basal till layer (Figure 2). The scree slope in the MK is regularly eroded and scoured from a perennial snowfield that is retreating by the end of the summer season, and this made the sampling of distinct soil-sediment horizons straightforward. We manually excavated only one pit for high resolution soil sampling and considered that due to the very small surface area of the surficial soil apron within the PM catchment (0.06 km^2), the specific profile is representative of the PM soil development. We selected a location in the center of a circular soil-sediment pan that was free of vegetation, surface carbonate fragments (Figure 2). After sampling, the pit was closed and refilled with the excavated material in accordance with Mount Olympus National Park directions. In locations with long lasting snowpack, we observed a humic A horizon, but since these locations host several endemic flower species, the Management Unit of Mount Olympus National Park, did not grant permission to excavate a soil pit in these sensitive sites. The PM soil samples were additionally subjected to microscopic and radiogenic isotope analyses and magnetic measurements to investigate the potential chemical alterations processes during PM soil development. Mineralogical and radiogenic isotope analyses were also performed in two (n = 2) samples of aeolian dust that were deposited on the PM snowpack during the spring seasons of 2018 and 2022. The long-range aeolian dust transport episodes occurred on March 22–24, 2018, and March 16–18, 2022. The synoptic conditions of these distinct episodes show that the dust emissions traveled to Mount Olympus from the Sahara Desert and left an orange hue on the snowpack, which later in the spring season formed distinct layers in the snowpack (Figure 3). We therefore consider the samples collected from the PM snowpack as representative of Sahara dust accretion in Mount Olympus alpine soils.

3.2 Grain size analyses

The soil samples were transported to the lab, wet sieved through a 3.5-mm sieve, and treated with 30% hydrogen peroxide (H_2O_2) at 70 °C for 12 h to remove organic matter. The H_2O_2 treatment was repeated three times until the samples were completely bleached and all organic matter was degraded. The samples were washed with distilled water and analyzed with a Mastersizer 3000 laser diffraction particle-size analyzer to define the bulk grain size distributions of the sand, silt, and clay fractions. The samples were run through the automated dispersion unit and sodium hexametaphosphate solution (Calgon) was added as dispersion factor. Statistical analyses of the grain size distributions and derivation of the clay, silt, and sand fractions were realized with MATLAB Curve Fitting Lab (CFLab), which performs curve fitting on sediment grain size distributions using the Weibull probability distribution function (Wu et al., 2020).

3.3 Mineralogy

Identification of the mineral phases of the soil and aeolian dust bulk samples was achieved through X-ray diffraction (XRD, Philips diffractometer PW1800, Co radiation at 40 kV and 40 mA), and two samples from the top and base of the PM soil profile (PM1 and PM15) were additionally analyzed for their clay (<2 µm) mineralogy through ethylene glycolation and heating for 2 h at 550 °C. The PM soil samples semi-quantitative composition of the main mineral phases (e.g., quartz, feldspar, plagioclase, micas, calcite) was determined using MAUD-Material Analysis software applied for full pattern Rietveld refinement (Lutterotti et al. 2007) and is expressed as weight percent (wt %) concentrations.

3.4 Petrographic, magnetic, and isotopic analyses

Additional analytical methods were applied only to the PM soil samples to assess the potential sources of soil-forming material, pedogenesis, and chemical weathering. The fabric configuration of the PM alpine soil was explored through scanning electron microscopy–energy dispersive spectrometry (SEM–EDS) analyses (JEOL JSM-840A equipped with an INCA 250; Oxford) with a 20-kV accelerating voltage and 0.4-mA probe current. Backscattered electron images (BSE) enabled us to detect the shapes of different minerals, and the physical weathering features of specific grains, whereas with the EDS analysis we examined areas of different chemical composition within the same soil aggregates.

We additionally explored the existence of ferromagnetic components and the potential for secondary iron oxides formation in the PM soil profile through magnetic susceptibility measurements. The discrete samples were packed in cubical plastic boxes (2 × 2 × 2 cm) and weighed before the measurements. Volume-specific magnetic susceptibility measurements were performed using both a Bartington dual MS2B sensor at low and high frequencies of 0.465 and 4.65 kHz. The results are expressed as mass-specific magnetic susceptibility (χ; 10^{-8} m^3/kg). During the measuring procedure, every sample was measured at least three times and the average value was assigned as the final measurement. For each sample, two air measurements were performed before and after sample measurement. The frequency-dependent susceptibility (χ_{FD}; %) was calculated according to Dearing et al. (1996):

$$\chi\mathrm{FD}\% = \frac{100(\chi\mathrm{LF} - \chi\mathrm{HF})}{\chi\mathrm{LF}} \quad (1)$$

where χ_{LF}, χ_{HF}, are the magnetic susceptibility at low and high frequency, respectively. Samples PM16 and PM15, which were considered as more representative of the PM soil regolith boundary, were additionally subjected to thermomagnetic analysis to define the origin of the ferromagnetic particles at the base of the PM soil. Measurements of continuous thermomagnetic curves (K–T curves) at low and high temperature were realized with the furnace CS3 of the AGICO MFK1-FA susceptibilimeter.

The potential sources of the PM soil and aeolian dust were evaluated through their Sr and Nd isotopic ratios. Isotopic measurements were performed at the University of Arizona TIMS laboratory following the procedure in Conroy et al. (2013) on soil samples. Samples were not spiked and dissolved in mixtures of ultrapure Hf-HNO3 acid. Elemental separation of dissolved samples was carried out in chromatographic columns via HCl elution in a clean laboratory environment. Conventional cation columns filled with AG50W-X4 resin were used for Sr and REEs separation and anion columns with LN Spec resin for Nd separation following Ducea et al. (2020). Sr cuts were loaded onto Ta single filaments and Nd cuts onto Re filaments. $^{87}Sr/^{86}Sr$ and $^{143}Nd/^{144}Nd$ ratios (Table 3) were measured on a VG Sector 54 thermal ionization mass spectrometer (TIMS) fitted with adjustable 1011 Ω Faraday collectors and Daly photomultipliers. NBS SRM 987 Sr standard and La Jolla Nd standard were analyzed during the samples run to ensure the performance of the instrument and to perform some minor correction on the final reported ratios.

3.5 Erosional potential and aeolian dust accretion proxies

The erosional potential of the three sampling sites, which are distanced along a 2km transect was derived from field estimates of the vertical height of the MK and TZ rocky headwalls and their scree slopes. We evaluated the plateau and scree slope energy distribution and maturity stage from the dimensionless ratio between the vertical height of the scree slope (Ht) to the vertical height of the headwall (Hc) following Statham (1976) (Figure 2).

To assess the potential contribution of distal and local aeolian dust inputs in the PM soil we used the contents of quartz (wt. %). The source of quartz can be local, from the Pieria Mountains silicate bedrock and from the granites to the west of Mount Olympus, or can be transported during Sahara dust episodes, as evidenced from the XRD analyses of the PM snowpack samples, which are in line with Sahara dust samples from the Pyrenees, the European Alps, and the Carpathian Mountains that contain high amounts of quartz (e.g., Rellini et al., 2009; Rodriguez-Navarro, 2018; Marmureanu et al., 2019). Herein, we cannot exclude the possibility of quartz release from the local bedrock through periglacial erosion, but the amount of quartz released from local bedrock dissolution is expected to be small, wt.% concentration of the insoluble residue from carbonates in Greece is less than 1% (MacLeod, 1980; Kantiranis, 2001; Kirsten and Heinrich, 2022). Therefore, it is reasonable to consider quartz (wt. %) as a reliable proxy of aeolian dust accretion.

We selected the ε_{Nd} ratio as a second independent proxy particularly of Sahara dust accretion in the PM soil. We did not use the Sr ratio ($^{87}Sr/^{86}Sr$) as it can be impacted by the dissolution of carbonate particles and replacement of Ca by Sr during pedogenetic alteration of the PM soil (e.g., Shalev et al., 2013). Sr isotopic distributions of PM soil can be further complicated by the accretion of sea-salt Sr through orographic precipitation (Kurtz et al., 2001). Rain is not a significant source of Nd, so the addition of rainwater and snow should not affect the Nd isotopic composition of the aeolian dust, so ε_{Nd} is buffered against these changes (Kurtz et al., 2001). We estimated the fraction of Sahara dust from the ε_{Nd} ratios of the PM soil, the dust deposited on the snowpack, and the local bedrock following the method by Kurtz et al (2001):

$$f = \frac{(\varepsilon\text{Nd PM soil} - \varepsilon\text{Nd bedrock})}{(\varepsilon\text{Nd Sahara dust} - \varepsilon\text{Nd bedrock})} \quad (2)$$

As we had not obtained direct Sr and ε_{Nd} values from Mount Olympus bedrock, we used the value of the basal sample PM 16, which is dominated by bedrock derived calcite and falls in the same value range with basin-average values of terrestrial, coastal, and marine sediments deposited in the Aegean Sea (Weldeab et al., 2001).

4 RESULTS

4.1 Alpine soil formation across a hillslope energy gradient

According to Statham (1976), Ht/Hc values above 0.4 characterize a mature scree slope, which is the case for the TZ (0.6) but not for the MK (0.3) scree slope, and this reflects the older deglaciation age of the TZ cirque (□12.5 ka BP, Section 2.1). The MK scree slope is deposited behind the LIA moraine (Figure 1C), so that the most recent deglaciation processes (□0.6 ka BP to present) has resulted in immature scree development. Conversely, the low-relief, low-erosion PM acts as a long-term depocenter of slope wash and detrital (aeolian and bedrock derived through freeze-thaw action) sediments. For this low-energy setting, we believe that minor colluvial contributions, cryoturbation, aeolian dust accretion, fine earth translocation, and post-depositional mineral alteration are the major drivers of PM soil production. The irregular boundary between the base of the PM soil and the underlying regolith composed of glacial till and outwash gravels, is indicative of cryoturbation, while observations of late-season soil freezing and waterlogging (Figure 4) provide permissive evidence that PM soil development is disturbed by cryogenic processes. The energy gradient along the contrasting environments impacts the soil color. The PM soil basal layer overlying the regolith shares similar color characteristics with the MK samples and with the TZ upper sediment horizon, which have grey to olive green hues (Munsell dry color 2.5– 5 Y; Table 1). Conversely, the lower clast-free sediment horizon of the TZ scree shares similar Munsell dry color characteristics with the PM soil, characterized by red-brown to yellow hues (7.5–10 YR, Table 1), suggesting that these soil samples are more oxidized and are undergoing pedogenetic alterations.

4.2 Grain size variation

The interactions between slope processes, colluvial sediment transport, and aeolian sub additions result in polymodal grain size distributions that display different shapes among MK, TZ, and PM soils. Five grain size modes (M1 to M5) were mathematically derived from the application of the CFLab curve-fitting algorithm. Fitting degrees were >99% and fitting residuals were <0.1%, indicating excellent fits for the raw grain size distribution curves (Figure 5 A, B, C, and D). The fine-earth (clay and silt) fractions resemble grain size modes M1 and M2 with respective mean grain sizes of □2 and □4 µm and M3 with mean grain sizes between 10 and 30 µm. The sand fraction is composed of two modal sub-populations: a fine-sand-grain size mode (M4, mean grain size □80 µm) and a coarse sand-grain size mode (M5, mean grain size 440 µm) (Figure 5 E, F, G, and H; Table 1). The production of coarse sand is transported to the respective interbedded sediment horizons by rockfall activity and colluvial processes, or in the case of the low-sloping PM, through slope wash. The fine sand (M4) subpopulation was not traced in the PM soil samples, and this can be linked to either selective entrainment of M4 or to distortion of the MK and TZ grain size curves and truncation of the coarser modes (Garzanti et al., 2009).

In addition to the distinct color variations, the contrasting slope-energy distribution between the MK, TZ scree slopes and the PM depositional environments also defines their textural compositions. Sediment horizons developed on the surface of the MK scree slope contain higher amounts of sand (□90%) and lower amounts of silt and clay (□10%) compared with their TZ counterparts (□75% and □25%), implying that the dominance of sand in the sediment horizons of the scree slopes derives from freeze-thaw and colluvial activity. The coarse-sand content (M5) of the PM soil basal layer is 6% but is lower within the solum (2%–3%), suggesting either reduced periglacial activity and/or low transport capacity of erosional products from the catchment through slope wash processes during the PM soil formation (Table 1; Figure 2, lower graphs).

The grain size distribution curves of the PM soil present a significant change in shape between soil depths of 14 and 16 cm, which is characterized by a 15% reduction of the clay and very-fine-silt fractions (M1 and M2) and by a similar increase of silt contents (Figure 5A and B). This sharp textural differentiation was not supported from field observations, where the solum appeared homogenous without distinct pedogenetic horizons and without any visual evidence of an erosional layer (Figure 6A), but it is supported by changes in the soil color. The samples above a soil depth of 14–16 cm exhibit red to brown hues (7.5 YR), whereas the samples below this layer have more yellow-red (10 YR) hues (Table 1). We also observed clay coatings in sparse secondary carbonates (calcretes) along the lower part of the PM soil profile, which we interpret as evidence of soil mixing and downward translocation of dissolved Ca and secondary calcite precipitation at the base of the soil profile. Based on these observations, we partitioned the PM soil profile in two horizons: an upper Bw horizon between 0 and 14 cm with red to brown hues, low clay (□25%), and high silt (□75%) contents, and a lower illuvial Bt horizon between 14 and 32 cm with higher (□40%) clay contents, a yellow-red hue, and smaller amounts (□5%) of sand compared with the overlying Bw horizon (Figure 6).

4.3 Soil and aeolian dust mineralogy

XRD analysis of the bulk samples reveals a mineralogy that substantially differs between the MK, TZ, and PM soils and, like the soil colorization and textural variations, follows the erosional slope gradient. The most dominant mineral phase in the clast-free material of the MK and TZ soils is calcite. Other minerals identified include dolomite along with quartz and micas. Conversely, the bulk mineralogical composition of PM soil exhibits a richer matrix of minerals that includes quartz, chlorite and mixed layer clays, mica, potassium feldspars, and plagioclase (Figure 7). Calcite is dominant (□50%) only in basal sample PM16 (Figure 6; Table 2). Quartz, clays, and mica are the most dominant mineral phases in the PM soil (□80%) with low values in basal sample PM16, whereas plagioclase, K-feldspar, and mica represent the remaining 20% (Table 2). Semi-quantitative analysis of the clay mineralogy of two samples retrieved from the surface of the Bw horizon and the base of the Bt horizon (samples PM1 and PM15) revealed high concentrations of smectite and kaolinite (80%) and low contents of chlorite and illite. Surface sample PM1 contains 45% smectite and 35% kaolinite, whereas basal sample PM15 has higher smectite (65%) and lower kaolinite (25%) contents (Table 2).

From the comparison of the XRD spectra (Figure 7), it is obvious that the bulk mineralogy of the PM soil matches that of the Sahara dust samples. Both Sahara dust samples show the presence of clay minerals, quartz, mica, calcite, plagioclase, K-feldspar, and dolomite. The detected mineral phases are typical of Saharan dust deposited in Europe during both dry- and wet-deposition (red rains) events (Scheuvens et al., 2013). Additionally, recent studies of Saharan dust wet deposition in the Iberian Peninsula also indicated the presence of Fe-Ti oxides, such as goethite and hematite, and of Ti oxides, such as rutile (Rodriguez-Navarro et al., 2018), but these were not depicted from our XRD analyses. Despite their overall XRD spectral similarity, a pronounced difference between the contemporary Sahara dust and PM soil samples is the presence of calcite and dolomite in the dust samples and their near absence from the PM soil profile (Figure 7). The smooth and low intensity peaks for calcite and dolomite at 29.43 and 30.7 2ϑ in surface sample PM1 indicate the partial removal of calcite, whereas similarly subdued peaks in basal sample PM16 denote near complete decalcification of the solum (Figure 7).

4.4 Magnetic susceptibility of PM soil

The magnetic susceptibilities of the PM soil bulk samples were measured to provide insight into the ferromagnetic components of the PM soil and their potential alterations. Overall, the low-frequency magnetic susceptibility (χ_{lf}) is higher in the lower Bt horizon, with average values for samples PM8–PM16 of 55 × 10^{-8} m^3 kg^{-1} , and lower χ_{lf} values in the Bw horizon, with average values for samples PM1–PM7 of 36 × 10^{-8} m^3 kg^{-1} (Figure 8A). Similar value ranges were measured for the high-frequency magnetic susceptibility (χ_{hf}). The estimated values of frequency-dependent (χ_{FD}) susceptibility presenting a wide range of values ranging between 0% (sample PM13) and 14%, with significantly higher values in the Bw horizon (Figure 8B). According to Dearing (1999), high χ_{FD} values (>10%) are indicative of the presence of superparamagnetic Fe oxide nanoparticles (< 0.05 µm), suggesting a higher amount of fine ferrimagnetic grains in the surface horizon Bw, which potentially can be of detrital (aeolian and/ eroded bedrock) origin.

The mineral phases responsible for the magnetic enhancement of the Bt horizon were deduced from high-temperature magnetic susceptibility measurements performed during a single heating–cooling cycle to 700 °C (Figure 8C). We estimated the Curie temperature (T_c) of samples PM16 and PM15 to examine the potential existence of superparamagnetic ultrafine particles in the base of the PM soil profile, which is in contact with the regolith. The thermomagnetic analysis of sample PM16 failed completely, likely due to its high calcite content and absence of magnetic phases. On the other hand, sample PM15 resembling the soil-regolith lower boundary, revealed a uniform χ-T behavior that is indicative of the dominance of two magnetic phases (Figure 8C) – one with Tc, or transformation temperature, between 260–320 ◦C, probably maghemite, and a second one around

600 ◦C, which is typical for oxidized magnetite (Jordanova et al., 2022). Since the nano-sized pedogenic magnetite is unstable upon heating (Dunlop and Özdemir, 1997), the identified oxidized magnetite suggests that weak pedogenetic production of ferromagnetic components occurs in the base of PM soil profile.

4.5 Radiogenic isotopes

More information on the provenance of the PM-soil-forming material was derived from the radiogenic isotope analysis of the soil samples and of the 2018 Sahara dust sample. The $^{87}Sr/^{86}Sr$ values of PM soil samples range from 0.71437 to 0.72071 and the ε_{Nd} values from -7.75 to -9.80 (Table 3). Overall, the PM soil $^{87}Sr/^{86}Sr$ – ε_{ND} cluster together apart from sample PM16, which has the lowest value of the PM soil $^{87}Sr/^{86}Sr$ ratio (Figure 9). The analyzed Sahara dust sample exhibits $^{87}Sr/^{86}Sr$ value of 0.71272 that falls within the lower range of North African dust sources between ~0.71200 and 0.74000 (Erel and Torrent, 2010; Grousset and Biscaye, 2005). The Sr isotopic ratio of the Sahara dust sample shows potential mixing with rainwater and local sea salt aerosols during the March 2018 wet deposition event but also with other European aerosol sources, which is validated by the fact that the dust plume of the March 2018 travelled over Europe before it reached Mount Olympus (Figure 3A). The Sahara dust sample has an ε_{Nd} value of –6.80. Plotting the $^{87}Sr/^{86}Sr$ and ε_{Nd} measurements against literature values from terrigenous, coastal, and marine sediments from the Aegean Sea region (Weldeab et al., 2002) reveals an isotopic similarity between the Sahara dust and of sample PM16 with these sediments (Figure 9). A reasonable interpretation of this observation comes from the fact that basal sample PM16 resembles more the soil regolith and plots close to the contemporary and Holocene values of Aegean Sea terrestrial, coastal and marine sediments. The $^{87}Sr/^{86}Sr$ values representing the PM soil regolith show similar values with the Aegean Sea terrestrial and marine sediments and likely represent a mix of Sahara dust with Mesozoic and Cenozoic bedrock carbonates, which are overall characterized by low $^{87}Sr/^{86}Sr$ values of <0.70800 (Capo et al., 1998;

Frank et al., 2021). The two subclusters of PM soil samples have more radiogenic values compared with those of the rest of the samples and clearly correspond to Bw and Bt horizons. The increasing silt contents towards the surface of the PM soil profile (Figure 6, Table 1) occur with $^{87}Sr/^{86}Sr$ and ε_{Nd} values towards more crustal values (color variation in Figure 9) that are representative of the central Sahara province. Therefore, the increases in the silt fraction within the PM soil profile can be directly linked to increases in Sahara dust accretion. This is further supported by range of the silt fraction mean grain size between 14 and 30 μm (Table 1), which is similar to those for modern Sahara dust deposits from Crete, which range 4–8 μm and 16–30 μm (Mattson and Niéhlen, 1996; Goudie and Middleton, 2001). In terms of Sahara dust provenance fingerprinting, the $^{87}Sr/^{86}Sr$ and ε_{Nd} values of the PM soil samples fall within the range (1σ) of the central North African dust source area, which broadly involves the Bodele depression (PSA2; Jewell et al., 2021).

5 DISCUSSION

5.1 PM soil parent material

The mineralogical (XRD) analyses, show that calcite is the dominant mineral phase of MK and TZ interbedded sandy sediment and PM basal layers (Figure 7, lower XRD diagrams TZ01 and Table 2 sample PM 16), which in the periglacial environment of Mount Olympus is expected to dissolve slowly (e.g., Gaillardet et al., 2019) and produce an insoluble residue that comprises the PM soil parent material. MacLeod (1980) analyzed the mineral composition of the insoluble residue of carbonates from western Greece and defined a mineralogical suite of quartz, kaolinite, and mica (illite). Kantiranis (2001) studied the carbonate rocks of northwestern Greece and found insoluble residue □1wt.% consisting mainly of micas, quartz, hematite, chlorite, feldspars, and amphibole, whereas the insoluble residue of carbonate basement rocks from Crete also resembles □1 wt.% of the whole rock samples and is composed of a sandy loam matrix rich in quartz, plagioclase (albite), and mica (illite) (Kirsten and Heinrich, 2022). Thus, the dissolution of the local carbonate parent material within the interbedded sediment layers and in the basal layer of PM soil, can release very small quantities of bedrock-derived impurities such as quartz, plagioclase, illite, and kaolinite that are incorporated in the solum, but cannot explain the □30cm thick PM soil mantle and □60cm thickness of the layers interbedded in the scree slopes.

It has also been proposed that clay in terra rossa soils can derive from isovolumetric replacement of calcite to authigenic clays across a metasomatic front, but this mechanism requires significant input of aeolian dust to provide essential elements such as Al, Si, Fe and K for clay formation (Merino and Banerjee, 2008). Even though we did not estimate the dissolution rate of Mount Olympus bedrock metacarbonates and the elemental composition of the insoluble residue, we consider that the fine earth (silt and clay) contents of MK and TZ interbedded layers, which average 10% and 25%, respectively, cannot be derived only by carbonate dissolution and/or by isovolumetric replacement of calcite. Küfmann (2008), Krklec et al. (2022) and Ott et al. (2023) propose carbonate bedrock dissolution rates between □0.23, 0.15 and 0.4 cm/ka respectively, which for the postglacial (12.5 ka BP to present) alpine soil formation on Mount Olympus imply □5 cm of carbonate loss to soil formation, a value too low to explain the observed thickness of MK, TZ, interbedded layers and PM soil as a result of residual clay accumulation alone. Our direct observations of episodic Sahara dust deposition on the snowpack of Mount Olympus (Figure 3) provide undisputable evidence of Sahara dust accretion on PM soil. The relative contribution of local dust from moraines, outwash plains and from silicate bedrock formations in the vicinity of Mount Olympus is estimated in the following section, but irrespective of the relative dust sources (Saharan and local), the high-energy erosive regime of Mount Olympus alpine critical zone intercepts the formation of extensive aeolian dust mantles, like the one found on the stable Plateau of Muses. We thus suggest that the production of silt, and clay in the PM soil basal layer, partly reflects the contribution of mechanically produced sandy and fine earth carbonate debris and its dissolution products, which together with aeolian dust accretion, comprise the parent materials for the PM soil production.

5.2 Relative contributions of aeolian dust inputs

Studies on terra rossa soils in Greece, with typical bimodal grain size distributions consisting of clay and silt subpopulations with grain size ranges of 2–4 and 10–40 µm, respectively, ascribe the clay fraction, which is rich in illite and kaolinite, to the limestone residue, and the silt fraction, which is made up entirely of quartz, to long-range aeolian transport from variable sources (Russel and Van Andel, 2003). In line with this notion, we considered the quartz wt. % content in the solum, as a proxy for aeolian dust in general and not exclusively of Sahara dust. The rounded shape of quartz grains observed in SEM images (Figure 11D), provides supplementary evidence for the aeolian transport of quartz grains. Furthermore, we consider that the neodymium-derived mass fraction (*f*), solely a proxy of Sahara dust accretion in the PM soil. This is supported by the high statistical correlation between the silt fraction (M3) with the ε_{ND}-derived *f* fraction (R^2= 0.73, P< 0.001) and by the similarity of the grain size ranges between the silt fraction and the modern Sahara dust deposits. The mass fraction (*f*) of Sahara-dust-derived ε_{ND} was calculated based on the highest ε_{Nd} value of sample PM 16 and Aegean Sea sediments (ε_{Nd} = -5.94) and on the lowest value of Sahara dust PSA2 (ε_{Nd} = −13.81) end members. The ε_{Nd} value of Aegean Sea sediments is considered conservative in relation to that of Mount Olympus bedrock due to the mixing of the carbonate bedrock sediments with other sources of silicate bedrock during fluvial transport.

The ε_{ND}-based Sahara dust contributions to the PM soil varies between □35% and □50% (except that of basal sample PM16) (Figure 10). Conversely, the quartz-derived aeolian dust contribution ranges between □45% and 65%, shows a relatively small variation with depth and an abrupt increase (□25%) from sample PM16 to PM15 (Figure 10). The basal sample PM16 exhibits the lowest contributions of quartz concentration, *f* ratio values (Figure 10) and silt concentrations (Table 1, Figure 6) and is considered an outlier representing the regolith-PM soil mix, which agrees with its distinct color and lowest magnetic susceptibility values. The preservation of quartz in the PM soil profile and especially in the lower Bt horizon requires a mechanism of reduced Sahara dust input and/or loss to weathering, with simultaneous inputs of other quartz-rich-derived dust. A pattern that can explain the lower ε_{Nd}-based Sahara dust contributions in the Bt horizon and the near steady quartz contents is a shift in atmospheric circulation patterns that resulted in less-frequent dust transport episodes from north Africa along with steady aeolian quartz accretion from local quartz sources. Aeolian quartz from the silicate bedrock formations of the Pieria mountains, Mount Olympus granites and even from the Katerini alluvial plane (Figure 1) can be deposited on Mount Olympus periglacial zone during periods of regional aridity, associated with thinning of vegetation, desiccation of the Katerini alluvial plane, and immobilization of fine dust grains through convection.

Based on the above, we tentatively attribute the □15% difference between the ε_{Nd}-based estimates and the quartz-based estimates to accretion of quartz-rich dust from local sources during the formation of the Bt horizon, considering that the contribution of bedrock derived quartz from the insoluble residue is □1%. From the ε_{Nd}-based contributions, we estimate that the Sahara dust accretion to PM soil is between □35% to 50%, whereas local sources can potentially accrete another □15%. Our estimated aeolian dust accretion □65% is similar to the one in the North Calcareous Alps, where the local contribution of dust from the periglacial zone of the North Calcareous and Austrian silicate Alps is significant (Küfmann 2008), but our estimated Sahara dust contribution in the PM soil is higher than its respective average contribution (20 – 30%, Varga et al., 2016) in interglacial soils of the Carpathian Basin. We attribute this difference to the closer proximity of Mount Olympus to Sahara Desert than the Carpathian basin. Given that these values are conservative estimates, the aeolian contribution may potentially be higher as, in our calculations, we have not included aeolian transported micas, feldspars, and clays that are integral parts of Sahara dust samples deposited on the snowpack. We thus suggest that the aeolian dust accretion comprises a minimum of □65% of the PM soil parent material and that carbonate bedrock erosion, and pedogenetic production of detrital clays can potentially contribute another □35% to the development of PM soil.

5.3 Pedogenetic alterations

An alternative mechanism that can explain the nearly homogeneous depth distribution of quartz (Figure 10) is soil mixing by cryoturbation and subsequent translocation of fine earth particles from the upper Bw to the lower Bt horizon. The mechanism of illuviation does not necessarily cancel the climatic forcing of Sahara dust reduction and increase of local dust inputs during the development of Bt horizon, but rather can act synergistically. For example, a cold and arid climatic phase that immobilizes quartz-rich dust from the Mount Olympus and Pieria mountains piedmonts can also reactivate the periglacial processes on the Mount Olympus alpine critical zone, which in turn enhance scree slope aggradation, colluvial activity, intensification of freeze–thaw cycles, and cryoturbation of the soils. Cryogenically induced translocation of detrital (aeolian and bedrock derived) silt and clays deposited on the surface of the Bw horizon, distorts the textural composition and soil properties and results in massive structures like the one we observed in the PM soil profile (Figure 4).

Despite the absence of color difference and of distinct layers in the PM soil, the higher magnetic susceptibility values of the Bt compared to the Bw horizon, can result from the enrichment of ferromagnetic minerals during *in situ* weathering of translocated detrital fine earth particles through pedogenesis (Maher, 2011). However, the overall low values of the frequency dependent magnetic susceptibility (χ_{FD}<10), point to weak pedogenetic alteration of soil (Dearing et al., 1996), which in the base of PM soil profile occurs through the oxidation of ultrafine (titano)magnetite to maghemite (Section 4.4). The SEM-EDS analyses show the presence of ultrafine Fe-Ti grains throughout the solum (Figure 11B) apart from basal sample PM16 (Figure 11A), which is representative of the PM soil regolith. This is further supported from the EDS chemical composition of the calcite grains in basal sample PM 16 that have TiO_2 weight % concentration <1%. On the other hand, magnetite is found attached to clay minerals of the Bodéle depression surface sediments (Moskowitz et al., 2016), which is the major source of Sahara dust in PM soil (Figure 10). Also, magnetic susceptibility measurements of Sahara dust modern deposits in SE Bulgaria show a low frequency magnetic susceptibility value of χ_{lf}=97 × 10^{-8} m^3 kg^{-1} (Jordanova et al., 2013), which is close to the values of Bw horizon (χ_{lf}=86 × 10^{-8} m^3 kg^{-1}) and Sahara dust episodes are known to transport Fe-Ti oxides in the Mediterranean region (Rodriguez-Navarro et al., 2018). We can therefore ascribe the observed Fe-Ti oxides and (titano)magnetite an aeolian origin, from either the local igneous silicate outcrops, or the Sahara Desert. Collectively these observations imply that the magnetic enhancement of Bt compared to Bw horizon can result from a combination of fine earth illuviation of aeolian transported ultrafine magnetic particles from the Bw horizon to the Bt horizon through cryoturbation and subsequent weak pedogenetic modifications that result to the oxidation of magnetic minerals like (titano)magnetite and can also explain the reddish to yellow color hues.

5.4 Mineral weathering

In addition to the weak pedogenesis of ferromagnetic minerals in the base of the PM soil profile, we assessed the mineral weathering potential of non-magnetic minerals through the clay mineralogy composition of basal and topsoil samples PM15 and PM1. Both samples show the dominance of smectite with lesser contributions by kaolinite, chlorite, and illite (Table 2). High amounts of smectite in alpine soils result from the alteration of detrital chlorite and micas deposited on glacier surfaces and are found in proglacial fields in the European Alps and Rocky Mountains (Egli et al., 2003; Egli et al., 2011; Munroe et al., 2015), so that the 20% difference in smectite concentration (Table 2) between the basal and topsoil layers of PM soil can be partly related to enhanced mineral chemical weathering in the base of the solum. Similarly, kaolinite observed in the XRD profiles of the MK, TZ and Sahara dust samples (Figure 7), can be released from the dissolution of bedrock carbonates, as are the cases for western Greece (Macleod, 1980) and Crete (Kirsten and Heinrich, 2022), but can also form through the alteration of other detrital minerals, such as plagioclase (albite), a process that is common in glacial and periglacial environments (Anderson, 2000). Finally, high smectite and kaolinite contents can also be transported during Saharan dust transport episodes (e.g., Scheuvens et al., 2013), but specifically they are representative of the western Sahara dust provence (PSA 1, Figure 10; Rodriguez-Navarro et al., 2018). However, smectite and kaolinite are also found in modern Sahara dust samples deposited in Athens, Greece (Remoundaki et al., 2011). Therefore, we consider that the high (>80%) concentration of smectite and kaolinite in the PM soil clay (< 2 μm) fraction reflects the balance between direct aeolian deposition and *in-situ* weathering of detrital (aeolian and/or bedrock derived) micas and plagioclase, but the respective contributions of aeolian-transported versus that of bedrock-derived clay minerals subjected to post-depositional mineral alterations cannot be defined from the existing data.

5.5 Relative timing of PM soil development

Direct observations suggest that cryoturbation is a fundamental pedogenetic process in the development of PM soil and continues today along with the ongoing accretion of the surficial aeolian silt horizon Bw. The occurrence of seasonal soil freezing and lack of vegetation in the PM polygon centers provide evidence that cryoturbation is active, destroying soil horizonation and obscuring pedogenetic and chemical weathering signals. However, magnetic, and mineralogical data indicate the occurrence of weathered Fe-(Ti) oxides such as (titano)maghemite, and the dominance of smectite and kaolinite in the soil basal and topsoil layers, which enable us to conclude that mineral alteration, and pedogenetic modifications of deposited aeolian dust and local erosional products are ongoing processes within the PM soil profile, occurring in tandem with cryoturbation.

In the absence of absolute datings that can constrain temporally the processes driving the production of PM soil, we hypothesized on its age based on the conclusions drawn from the contributions of aeolian dust, and the impacts of cryoturbation. We tentatively ascribe the deposition of the base colluvial layer and/or the *in-situ* fragmentation of the regolith's till boulders to the most recent period of glacial activity on Mount Olympus. Based on the glacial record of the MK and TZ cirques, the best candidates of periglacial activity that have likely resulted in the deposition of outwash sand and gravels postdate the moraine stabilization phases at □12.5, 2.5, and 0.6 ka BP.

However, there is a 10-ka time span between the Holocene–Pleistocene boundary and the late-Holocene glacial expansions on Mount Olympus. Accepting that PM soil formation began after the moraine stabilization phase at □12.5 ka BP that was common to MK and TZ cirques, its production rate would be □3 x 10^{-5} m yr^{-1} assuming that soil erosion in the low-lying PM has been minimal. This rate is considerably lower than respective soil production rates of Alpine and Mediterranean soils formed over the last 10 ka (Egli et al., 2018; Figure 8). In contrast, by considering a late-Holocene age and that the PM soil development postdates the □2.5 ka BP moraine stabilization phase, the soil production rate is □1 x 10^{-4} m yr^{-1} an estimate that is in better agreement with the soil production rates presented by Egli et al. (2018) for both Alpine and Mediterranean soils. Furthermore, a late-Holocene development of PM soil broadly agrees with soil development patterns in diverse geomorphological environments in Crete (Kirsten and Heinrich, 2022). If this scenario is correct, then we can further hypothesize that development of the Bt horizon could have lasted between □2.5 and 1.0 ka BP, before a recorded phase of intense Sahara dust accretion in Mediterranean that resulted from the combined action of an orbitally induced decrease in solar insolation and of increased aridity over North Africa (Sabatier et al., 2020). This shift could potentially explain the sharp textural boundary between the Bt and Bw horizons and the increasing Sahara dust accretion on the upper Bw horizon. The hypothesized development of the Bw horizon over the past 1 ka could have been disturbed by cryoturbation during the LIA (□0.6 ka BP) glacial expansion in the MK and that continues until today. Ongoing work on Mount Olympus alpine critical zone involves efforts to accurately date the MK and TZ scree interbedded layers and the PM soil profile through Optically Stimulated Luminescence dating that is aided by the high concentrations of quartz in the fine earth fraction, as well as additional geochemical analysis and estimates of the local carbonate bedrock dissolution rates and its residual geochemical composition, in an overall attempt to provide a new continuous record of postglacial alpine landscape evolution in the Mediterranean periglacial zone.

6 CONCLUSIONS

In this study, we investigated the local processes that lead to the development of alpine soils on a stable landform on Mount Olympus, considering its regional setting representative of Mediterranean carbonate mountains that became gradually ice-free during the Pleistocene–Holocene transition but that have also been affected by late-Holocene climatic shifts towards glacial and periglacial conditions (Oliva et al., 2018). We discussed the relative contributions of erosion, aeolian dust accretion, and post-depositional pedogenesis and mineral alteration by comparing colluvial sediment layers interbedded in scree slopes with a soil B horizon developed on a regolith composed by slope outwash deposits and fragmented till boulders along a 2km hillslope energy gradient with a northeasterly orientation, which is the main direction of glacial cirque development on Mount Olympus.

Overall, our results suggest that soils developed in stable landforms like the PM show signs of weak pedogenesis and contain higher amounts of aeolian dust than locally eroded and chemically weathered products. Aeolian dust from local and Saharan sources is accreted in alpine soils formed in periglacial hummocky polygons of the PM and comprises □30%–65% of the soil mass weight. This interpretation matches those of several other studies on aeolian dust accretion in alpine soils (e.g., Gild et al., 2018; Kaüfmann, 2008; Munroe et al., 2015; Yang et al., 2016; Kirsten and Heinrich, 2022) and suggests that aeolian dust is the primary parent soil material on Mount Olympus. The major source of Sahara dust deposited on Mount Olympus is the Bodélé depression, which agrees with observations of accreted dust in Crete (Pye, 1992).

In the low-erosional environment of the PM, mineral alteration and weak pedogenetic modifications occur throughout the solum, but their signal is blurred by soil mixing due to ongoing cryoturbation. A sharp textural boundary not visible in the field separates an upper weathered soil Bw horizon from the lower Bt horizon, which is magnetically enhanced and enriched in smectite and kaolinite. Radiogenic isotope systematics, mineralogy, and magnetic susceptibility value range classify the Bw horizon as an aeolian silt layer that was likely formed during a late-Holocene shift of regional atmospheric circulation that resulted in increased Sahara dust accretion in alpine Mediterranean landscapes.

REFERENCES

Allard, J.L., Hughes, P.D., Woodward, J.C., Fink, D., Simon, K.& Wilcken, K.M. (2020) Late Pleistocene glaciers in Greece: A new ^{36}Cl chronology. *Quaternary Science Rev*iews, 245, 106528. Available from: https://doi.org/10.1016/j.quascirev.2020.106528.

Amit, R., Enzel, Y. & Crouvi, O. (2020) Quaternary influx of proximal coarse-grained dust altered circum-Mediterranean soil productivity and impacted early human culture: *Geology*, 49 (1), 61 – 65. Available from: https://doi.org/10.1130/G47708.1.

Anderson, S.P., Drever, J.I., Frost, C.D., Holden, P., 2000. Chemical weathering in the foreland of a retreating glacier. Geochim. Cosmochim. Acta 64 (7), 1173– 1189.

Capo, R.C., Stewart, B.W. & Chadwick, O.A. (1998) Strontium isotopes as tracers of ecosystem processes: theory and methods. *Geoderma,* 82, 197–225. Available from: https://doi.org/10.1016/S0016-7061(97)00102-X

Castorina, F., Magganas, A., Masi, U. & Kyriakopoulos, K. (2020) Geochemical and Sr-Nd isotopic evidence for petrogenesis and geodynamic setting of Lower-Middle Triassic volcanogenic rocks from central Greece: Implications for the Neotethyan Pindos ocean. *Mineralogy & Petrology,* 114, 39–56. Available from: https://doi.org/10.1007/s00710-019-00687-7.

Conroy, J.L., Overpeck, J.T., Cole, J.E., Liu, KB., Wang, D. Ducea, M.D. 2013. Dust and temperature influences on glaciofluvial sediment deposition in southwestern Tibet during the last millennium. *Global and Planetary Change*, 107, 132-144. https://doi.org/10.1016/j.gloplacha.2013.04.009.

Dearing, J., Hay, K., Baban, S., Huddleston, A., Wellington, E. & Loveland, P. (1996) Magnetic susceptibility of soil: an evaluation of conflicting theories using a national data set. *Geophysical Journal International*, 127, 728–734.

Dobiński, W., 2005. Permafrost of the Carpathian and Balkan Mountains, Eastern and Southeastern Europe. *Permafrost and Periglacial Process*, 16, 395–398.

Drewnik, M., Skiba, M., Szymański, W. & Żyla, M. (2014) Mineral composition vs. soil forming processes in loess soils — A case study from Kraków (Southern Poland), *Catena*, 119, 166 - 173. Available from: http://dx.doi.org/10.1016/j.catena.2014.02.012

Ducea, M. N., Barla, A., Stoica, A. M., Panaiotu, C. & Petrescu, L. (2020) Temporal-geochemical evolution of the Persani volcanic field, eastern Transylvanian Basin (Romania): Implications for slab rollback beneath the SE Carpathians. *Tectonics*, 39e2019TC005802. Available from: https://doi.org/10.1029/2019TC005802

Dunlop, D.J. & Özdemir, Ö. (1997) Rock Magnetism: Fundamentals and Frontiers. Cambridge University Press, Cambridge, New York.

Durn, G., Ottner, F. & Slovenec, D. (1999) Mineralogical and geochemical indicators of the polygenetic nature of terra rossa in Istria, Croatia. *Geoderma,* 91, 125–150.

Durn, G. (2003) Terra rossa in the Mediterranean region: parent materials, composition and origin. *Geolgika Croatia*, 56, 83 – 100.

Egli, M., Mirabella, A. & Fitze, P. (2003) Formation rates of smectites derived from two Holocene chronosequences in the Swiss Alps. *Geoderma,* 117, 81–98.

Egli, M., Wernli, M., Burga, C., Kneisel, C., Mavris, C., Valboa, G., Mirabella, A., Plotze, M. & Haeberli, W. (2011) Fast but spatially scattered smectite-formation in the proglacial area Morteratsch: an evaluation using GIS. *Geoderma,* 164, 11–21.

Egli, M., Dahms, D. & Norton, K. (2014) Soil formation rates on silicate parent material in alpine environments: Different approaches–different results? *Geoderma*, 213, 320 – 333.

Egli, M. & Poulenard, J. (2016) Soils of Mountainous Landscapes. In International Encyclopedia of Geography: People, the Earth, Environment and Technology (eds D. Richardson, N. Castree, M.F. Goodchild, A. Kobayashi, W. Liu and R.A. Marston). Available from: https://doi.org/10.1002/9781118786352.wbieg0197

Egli, M., Hunt, A.G., Dahms, D., Raab, G., Derungs, C., Raimondi, S. & Yu, F. (2018) Prediction of Soil Formation as a Function of Age Using the Percolation Theory Approach. *Frontiers in Environmental Science*, 6, 108. Available from: https://doi.org/10.3389/fenvs.2018.00108.

Erel, Y. & Torrent, J. (2010) Contribution of Saharan dust to Mediterranean soils assessed by sequential extraction and Pb and Sr isotopes. *Chemical Geology,* 275, 19–25. Available from: https://doi.org/10.1016/j.chemgeo.2010.04.007.

Frank, A.B., Frei, R., Triantaphyllou, M., Vassilakis, E., Kristiansen, K. & Frei K.M. (2021) Isotopic range of bioavailable strontium on the Peloponnese peninsula, Greece: A multi-proxy approach. *Science of the Total Environment*, 774, 145181, Available from: https://doi.org/10.1016/j.scitotenv.2021.145181.

Gaillardet, J., Calmels, D., Romero-Mujalli, G., Zakharova, E., Hartmann, J. 2019. Global climate control on carbonate weathering intensity. Chemical Geology, 527, 118762. https://doi.org/10.1016/j.chemgeo.2018.05.009.

Garzanti, E., Andò, S. & Vezzoli, G. (2009) Grain-size dependence of sediment composition and environmental bias in provenance studies. *Earth and Planetary Science Letters*, 277, 3–4, 422-432. Available from: https://doi.org/10.1016/j.epsl.2008.11.007.

Gild, C., Geitner, C. & Sanders, D. (2018) Discovery of a landscape-wide drape of late-glacial aeolian silt in the western Northern Calcareous Alps (Austria): First results and implications. *Geomorphology* 301, 39-52. Available from: https://doi.org/10.1016/j.geomorph.2017.10.025.

Goudie, A.S. & Middleton, N.J. (2001) Saharan dust storms: nature and consequences. *Earth Science Reviews*, 56, 179 - 204.

Grousset, F.E. & Biscaye, P.E. (2005) Tracing dust sources and transport patterns using Sr, Nd and Pb isotopes. *Chemical Geo*logy 222, 149–167. Available from: https://doi.org/10.1016/j.chemgeo.2005.05.006.

Haeberli, W., Hallet, B., Arenson, L., Elconin, R., Humlum, O., Kääb, A., Kaufmann, V., Ladanyi, B., Matsuoka, N., Springman, S. & Vonder Mühl, D. (2006) Permafrost creep and rock glacier dynamics. *Permafrost and Periglacial Processes,* 17, 189-214. Available from: http://doi.org/10.1002/ppp.561.

Jewell, A.M., Drake, N., Crocker, A.J., Bakker, N.L., Kunkelova, T., Bristow, C.S., Cooper, M.J., Milton, J.A., Breeze, P.S. & Wilson, P.A. (2021) Three North African dust source areas and their geochemical fingerprint*. Earth Planetary Science Lett*ers, 554, 116645. Available from: https://doi.org/10.1016/j.epsl.2020.116645.

Jordanova, N., Jordanova, D., Qingsong, L., Pengxiang, H., Petrov, P. & Petrovský, E. (2013) Soil formation and mineralogy of a Rhodic Luvisol — insights from magnetic and geochemical studies. *Global and Planetary Change,* 110, 397–413.

Jordanova, D., Georgieva, B., Jordanova, N., Guyodo, Y. & Lagroix, F. (2022) Holocene palaeoenvironmental conditions in NE Bulgaria uncovered by mineral magnetic and paleomagnetic records of an alluvial soil, *Quaternary International*, 631, 47-58. https://doi.org/10.1016/j.quaint.2022.06.009.

Kantiranis N. (2001) Calcination study of the crystalline limestone from Agios Panteleimonas, Florina, Greece. PhD Thesis, School of Geology, Aristotle University of Thessaloniki, 196p.

Küfmann, C. (2008) Are cambisols in alpine karst Autochthonous or eolian in origin*? Arctic Antarctic and Alpine Research*, 40, 506–518.
Kirsten, F. & Heinrich, J. (2022) Soil-sediment-configurations on slopes of Central and Western Crete (Greece) and their implications for late Holocene morphodynamics and pedogenesis – A conceptual approach, *Catena*, 214, 106238, 0341-8162. Available from: https://doi.org/10.1016/j.catena.2022.106238.

Krklec, K., Braucher, R., Perica, D. & Domínguez-Villar, D. (2022) Long-term denudation rate of karstic North Dalmatian Plain (Croatia) calculated from ^{36}Cl cosmogenic nuclides. *Geomorphology*, 413, 108358. https://doi.org/10.1016/j.geomorph.2022.108358.

Kuhlemann, J., Rohling, E., Krumrei, I., Kubik, P., Ivy-Ochs, S. & Kucera, M. (2008) Regional synthesis of Mediterranean atmospheric circulation during the last glacial maximum. *Science,* 321 (5894), 1338 – 1340.
Kurtz, A.C., Derry, L.A. & Chadwick, O.A. (2001) Accretion of Asian dust to Hawaiian soils; isotopic, elemental, and mineral mass balances. *Geochimica Cosmochimica Acta,* 65, 1971–1983.

Lawrence, C.R., Reynolds, R.L., Ketterer, M.E. & Neff, J.C. (2013) Aeolian controls of soil geochemistry and weathering fluxes in high-elevation ecosystems of the Rocky Mountains, Colorado. *Geochimica Cosmochimica Acta,* 107, 27–46.

Lehmkuhl, F., Nett, J.J., Pötter, S., Schulte, P., Sprafke, T., Jary, Z., Antoine, P., Wacha, L., Wolf, D., Zerboni, A., Hošek, J., Marković, S.B., Obreht, I., Sümegi, P., Veres, D., Zeeden, C., Boemke, B., Schaubert, V., Viehweger, J. & Hambach, U.(2020)Loess landscapes of Europe - mapping, geomorphology, and zonal differentiation. *Earth Science Reviews*, 215, 103496. Available from: https://doi:10.1016/j.earscirev.2020.103496.

Lutterotti L., Bortolotti M., Ischia G., Lonardelli I. & Wenk H.R. (2007) Rietvelt texture analysis from diffraction images. *Zeitschrift für Kristallographie*, 26, 125-130.

Maher, B.A. (2011) The magnetic properties of Quaternary aeolian dusts and sediments, and their palaeoclimatic significance. *Aeolian Research,* 3, 87–144.
Marmureanu, L., Marin, C.A., Andrei, S., Antonescu, B., Ene, D., Boldeanu, M., Vasilescu, J., Vitelaru, C., Cadar, O. & Levei, E. (2019) Orange snow: a Saharan dust intrusion over Romania during winter conditions. *Remote Se*nsing, 11, 2466. Available from: https://doi.org/10.3390/rs11212466.

Mattsson, J.O. & Nihlén, T. (1996) The transport of Saharan dust to southern Europe: a scenario. *Journal of Arid Envirnonments,* 32 (2), 111–119. Available from: https://doi.org/10.1006/jare.1996.0011.

Macleod, D.A. (1980) The origin of the red Mediterranean soils in Epirus. Greece. *European Journal of Soil Science,* 31 (1), 125–136.

Merino, E. & Banerjee, A. (2008) Terra rossa genesis, implications for karst, and eolian dust: a geodynamic thread*. Journal of Geology,* 116, 62 – 75.

Moskowitz, B.M., Reynolds, R.L., Goldstein, H.L., Berquó, T.S., Kokaly, R.F. & Bristow, C.S. (2016) Iron oxide minerals in dust-source sediments from the Bodélé Depression, Chad: Implications for radiative properties and Fe bioavailability of dust plumes from the Sahara. *Aeolian Research*, 22, 93-106, Available from: https://doi.org/10.1016/j.aeolia.2016.07.001.

Muhs, D.R. & Benedict, J.B. (2006) Eolian additions to late Quaternary alpine soils, Indian Peaks Wilderness Area, Colorado Front Range. *Arctic Antarctic and Alpine Research*, 38, 120–130.

Munroe, J.S., Attwood, E.C., O'Keefe, S.S. & Quackenbush, P.J. (2015) Eolian deposition in the alpine zone of the Uinta Mountains, Utah, USA. *Catena* 124, 119–129.

Munroe, J.S., Norris, E.D., Carling, G.T., Beard, B.L., Satkoski, A.M. & Liu, L. (2019) Isotope fingerprinting reveals western North American sources of modern dust in the Uinta Mountains, Utah, USA. *Aeolian Research*, 38, 39-47. Available from: https://doi.org/10.1016/j.aeolia.2019.03.005.

Oliva, M., Žebre, M., Guglielmin, M., Hughes, P.D., Çiner, A., Vieira, G., Bodin, X., Andrés, N., Colucci, R.R., García-Hernández, C., Mora, C., Nofre, J., Palacios, D., Pérez-Alberti, A., Ribolini, A., Ruiz-Fernández, J., Sarıkaya, M.A., Serrano, E., Urdea, P., Valcárcel, M., Woodward, J.C. & Yıldırım, C. (2018) Permafrost conditions in the Mediterranean region since the Last Glaciation, *Earth Science Reviews*, 185, 397-436, Available from: https://doi.org/10.1016/j.earscirev.2018.06.018.

Ott, R. F., Gallen, S. F. & Helman, D. (2023) Erosion and weathering in carbonate regions reveal climatic and tectonic drivers of carbonate landscape evolution, EGUsphere [preprint], Available from: https://doi.org/10.5194/egusphere-2022-1376.

Pye, K. (1992) Aeolian dust transport and deposition over Crete and adjacent parts of the Mediterranean sea. *Earth Surface Processes and Landforms,* 17, 271–288. Available from: https://doi.org/10.1002/esp.3290170306.

Rellini, I., Trombino, L., Firpo, M. & Rossi, P.M. (2009) Extending westward the loess basin between the Alps and the Mediterranean region: micromorphological and mineralogical evidence from the northern scope of the Ligurian Alps, Northern Italy. *Geografia Fisica Dinamica Quaternaria,* 32, 103–116.

Remoundaki, E., Bourliva, A., Kokkalis, P., Mamouri, R.E., Papayannis, A., Grigoratos, T., Samara, C., Tsezos, M. (2011) PM10 composition during an intense Saharan dust transport event over Athens (Greece). Science of The Total Environment, 409, 20,4361-4372. Available from: https://doi.org/10.1016/j.scitotenv.2011.06.026.

Rodriguez-Navarro, C., di Lorenzo, F. & Elert, K. (2018) Mineralogy and physicochemical features of Saharan dust wet deposited in the Iberian Peninsula during an extreme red rain event, *Atmospheric Chemistry and Physics* 18, 10089–10122. Available from: https://doi.org/10.5194/acp-18-10089-2018.

Runnels, C. & van Andel, T.J. (2003) The early stone age of the nomos of Preveza: landscape and settlement. In Landscape Archaeology in Southern Epirus, Greece, Vol. I, Wiseman J, Zachos K (eds). *Hesperia Supplement,* 32, 47–13.

Sabatier, P., Nicolle, M., Piot, C., Colin, C., Debret, M., Swingedouw, D., Perrette, Y., Bellingery, M.S., Chazeau, B., Develle, A.L., Leblanc, M., Skonieczny, C., Copard, Y., Reyss, J.L., Malet, E., Jouffroy-Bapicot, I., Kelner, M., Poulenard, J., Didier, J., Arnaud, F. & Vannière, B. (2020) Past African dust inputs in the western Mediterranean area controlled by the complex interaction between the Intertropical Convergence Zone, the North Atlantic Oscillation, and total solar irradiance. *Climate of the Past.* 16 283–298. Available from: https://doi.org/10.5194/cp-16-283-2020.

Sanders, D., Ostermann, M. & Kramers, J. (2010) Meteoric diagenesis of Quaternary carbonate rocky talus slope successions (Northern Calcareous Alps, Austria). *Facies,* 56, 27–46.

Šarić, K., Cvetković, V.,Romer, R.L., Christofides, G. & Koroneos, A (2009) Granitoids associated with East Vardar ophiolites (Serbia, F.Y.R. of Macedonia and northern Greece): Origin, evolution and geodynamic significance inferred from major and trace element data and Sr–Nd–Pb isotopes. *Lithos,* 108, 1–4, 131-150. Available from: https://doi.org/10.1016/j.lithos.2008.06.001.

Scheuvens, D., Schütz, L., Kandler, K., Ebert, M. & Weinbruch, S. (2013) Bulk composition of northern African dust and its source sediments – a compilation. *Earth Science Rev*iews, 116, 170–194. Available from: https://doi.org/10.1016/j.earscirev.2012.08.005

Shalev, N., Lazar, B., Halicz, L., Stein, M., Gavrieli, I., Sandler, A. & Segal, I. (2013) Strontium Isotope Fractionation in Soils and Pedogenic Processes. *Procedia Earth and Planetary Science*, 7, 790-793. Available from: https://doi.org/10.1016/j.proeps.2013.03.074.

Statham, I. (1976) A scree slope rockfall model. *Earth Surface Processe*s, 1, 43–62.

Stuut, J.B., Smalley, I. & O'Hara-Dhand, K. (2009) Aeolian dust in Europe: African sources and European deposits. *Quaternary International,* 198 (1–2), 234–245. Available from: https://doi.org/10.1016/j.quaint.2008.10.007

Styllas, M.N., Schimmelpfennig, I., Ghilardi, M. & Benedetti. L. (2016) Geomorphologic and paleoclimatic evidence of Holocene glaciation on Mount Olympus, Greece. *The Holocene,* 26 (5), 709–721.

Styllas, M. N., Schimmelpfennig, I., Benedetti, L., Ghilardi, M., Aumaître, G., Bourlès, D. & Keddadouche, K. (2018) Late-glacial and Holocene history of the northeast Mediterranean mountain glaciers – New insights from in situ-produced ^{36}Clbased cosmic ray exposure dating of paleo-glacier deposits on Mount Olympus, Greece, *Quaternary Science Rev*iews, 193, 244–265, Available from: https://doi.org/10.1016/j.quascirev.2018.06.020,2018

Styllas, M.N. & Kaskaoutis, D.G. (2018) Relationship between winter orographic precipitation with synoptic and large-scale atmospheric circulation: the case of Mount Olympus, Greece. *Bulletin of Geological Society of Greece,* 52, 45 – 70.

Styllas M. (2020) Tracing a late Holocene glacial climatic signal from source to sink under intensifying human erosion of eastern Mediterranean landscapes. *Mediterranean Geoscience Reviews* 2, 91–101. Available from: https://doi.org/10.1007/s42990-020-00031-8).

Varga, G., Cserhati, C., Kovacs, J. & Szalai, Z. (2016) Saharan dust deposition in the Carpathian Basin and its possible effects on interglacial soil formation. *Aeolian Research*, 22. Available from: https://doi.org/10.1016/j.aeolia.2016.05.004.

Weldeab, S., Emeis, K-C., Hemleben, C. & Siebel, W. (2002) Provenance of lithogenic surface sediments and pathways of riverine suspended matter in the Eastern Mediterranean Sea: evidence from 143Nd/144Nd and 87Sr/86Sr ratios, *Chemical Geology*, 186, 1–2, 139-149, https://doi.org/10.1016/S0009-2541(01)00415-6.

Wu, L., Krijgsman, W., Liu, J., Li, C., Wang, R. & Xiao, W. (2020) CFLab: A MATLAB GUI program for decomposing sediment grain size distribution using Weibull functions. *Sedimentary Geol*ogy, 398, 105590. Available from: https://doi.org/10.1016/j.sedgeo.2020.105590.

Yaalon, D.H. (1997) Soils in the Mediterranean region: what makes them different? *Catena*, 28, 157–169. Available from: https://doi.org/10.1016/S0341-8162(96)00035-5.

Yang, F., Zhang, G.L., Yang, F. & Yang, R.M. (2016) Pedogenetic interpretations of particle-size distribution curves for an alpine environment. *Geoderma*, 282, 9–15

FIGURES

Figure 1. (A) General setting of the study area within the Mediterranean basin. (B) Mount Olympus alpine domain that is considered in the study (yellow box), with the two respective piedmonts on the marine and continental sides, the adjacent Pieria Mountains and Katerini alluvial plane (SRTM 90 DEM Model). (C) The highest cirques and plateau of Mount Olympus with the respective locations of dated moraines (black curved lines from Styllas et al., 2018), the sampling locations considered in this study (yellow circles) and the geomorphological transects described in Figure 2 (yellow lines). MK: Megala Kazania cirque, TZ: Throne of Zeus cirque, PM: Plateau of Muses.

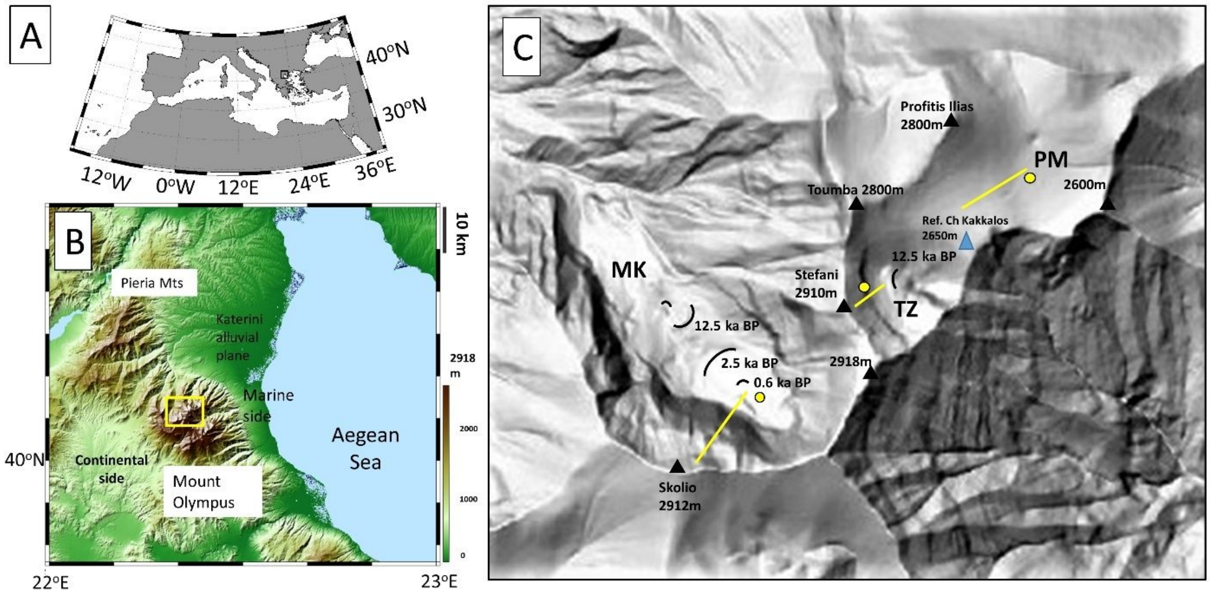

Figure 2. Conceptual diagram of the study, with the sampling sites and their morphological profiles, shown in Figure 1c as yellow lines, and with their respective textural characteristics that resulted from the grain size analysis. The respective heights of the rock cliffs (H_c) and talus slopes (H_t) are shown. The soil samples from the stratified scree clast free horizons in MK cirque are located behind the Little Ice Age moraine (left upper panel, photo, and diagram). The stratified scree slope under the rock wall of Stefani (2910m) in the TZ cirque, with the respective locations of the clast free soil samples (center panel, photo, and diagram) and the soil profile in the PM (right panel, photo, and diagram).

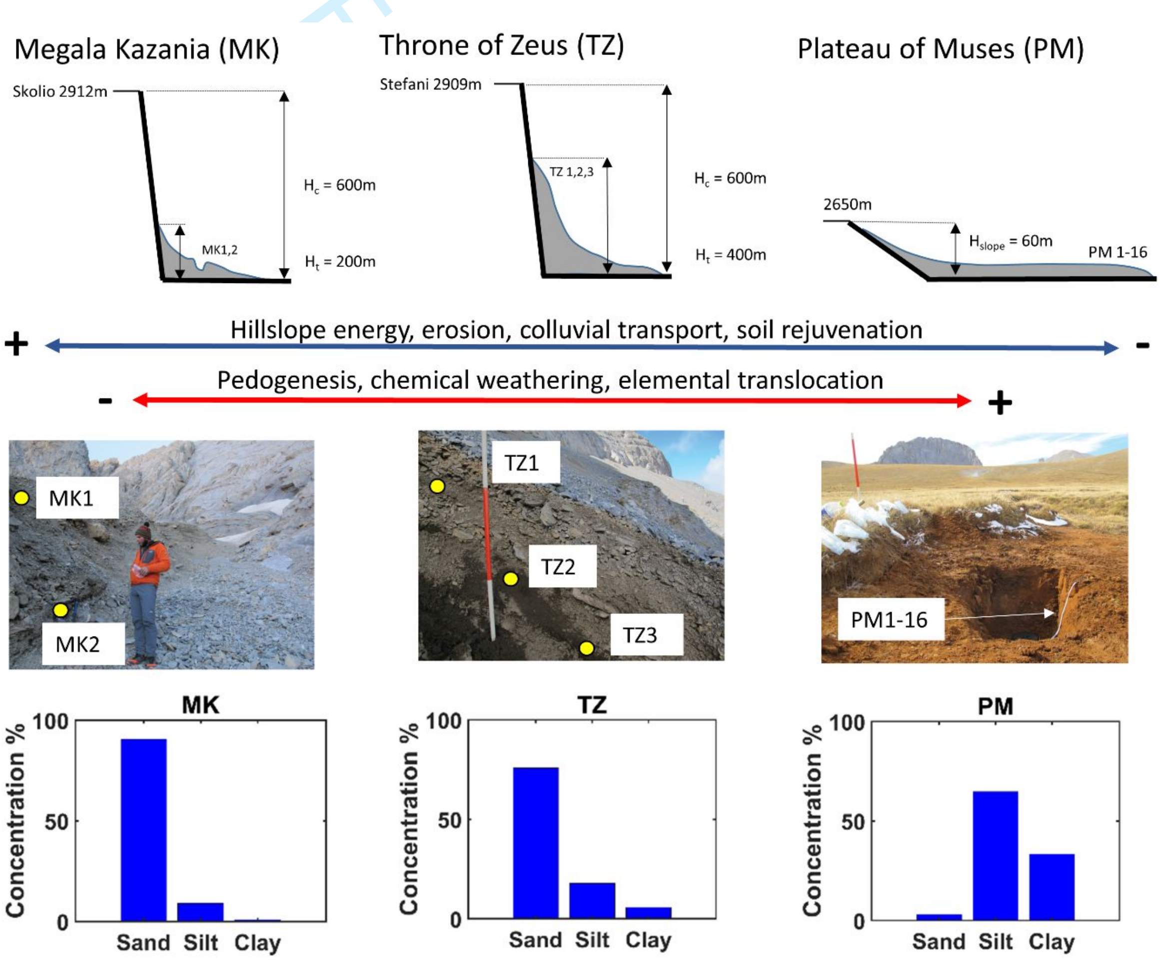

Figure 3. Synoptic maps and direct observations of two Sahara dust episodes on Mount Olympus alpine critical zone (black rectangle). (A). Aerosol Optical Depth (AOD) during March 22, 2018, and (B) and March 16, 2022, showing the trajectory of dust plume from Sahara Desert, and their impacts on the snowpack of the Plateau of Muses (C and D). The PM soil profile was excavated under the black arrow (C), whereas the snow pit (D) with two successive Sahara dust transport episodes in the spring of 2022, has also been excavated on top of the PM soil profile excavated pit. The NASA SUOMI/NNP Aerosol Optical Depth composition product was downloaded from the NASA EOSDIS Worldview platform (worldview.earthdata.nasa.gov).

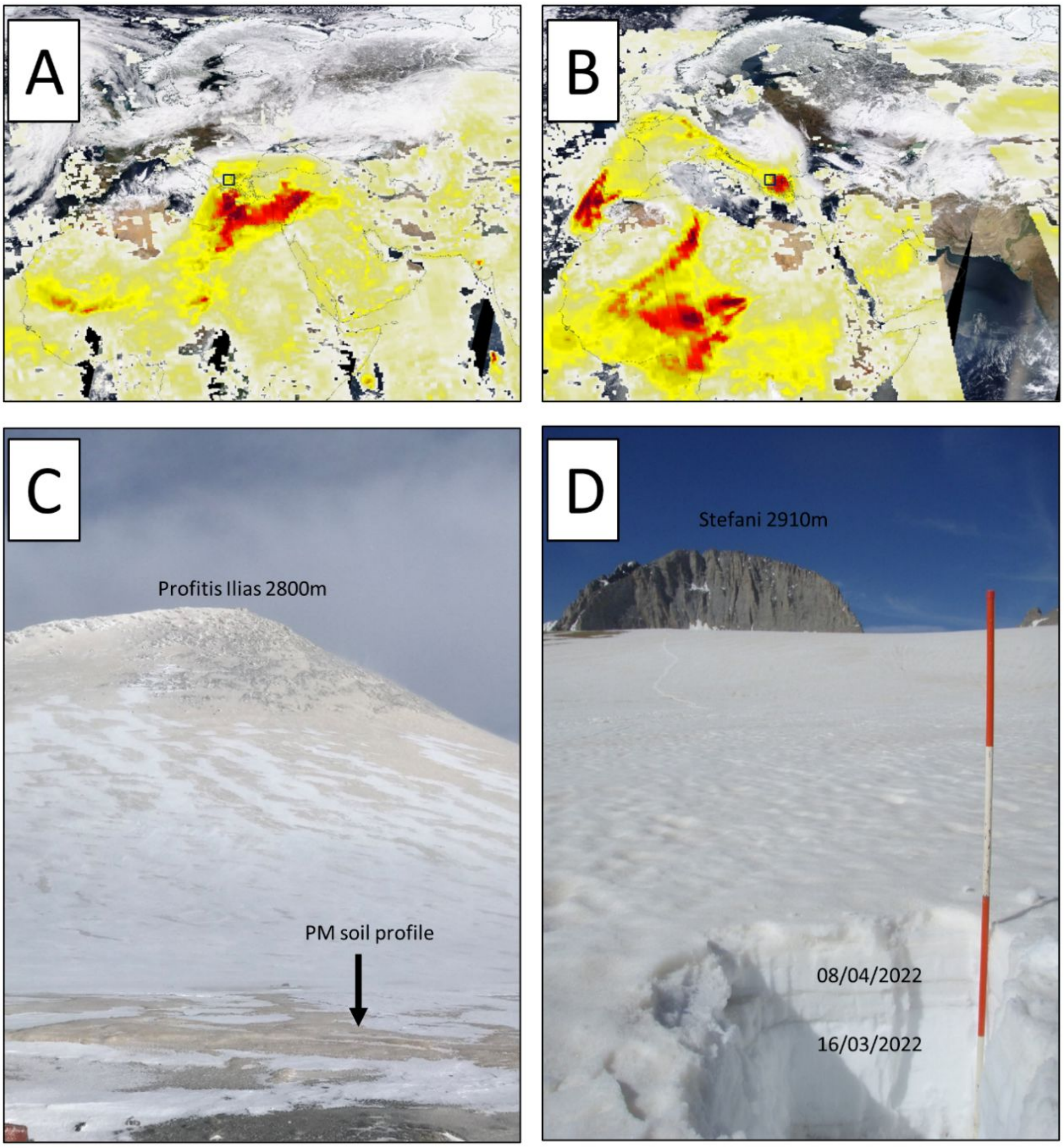

Figure 4. Evidence of soil disturbance on the Plateau of Muses under past and present-day climatic conditions. (A) An irregular gravel layer (blue dashed line) between colluvial gravel and the overlying soil resulting from cryoturbation. (B) Early summer season ongoing freeze of the soil surface layer and subsequent waterlogging (photo taken on June 2012).

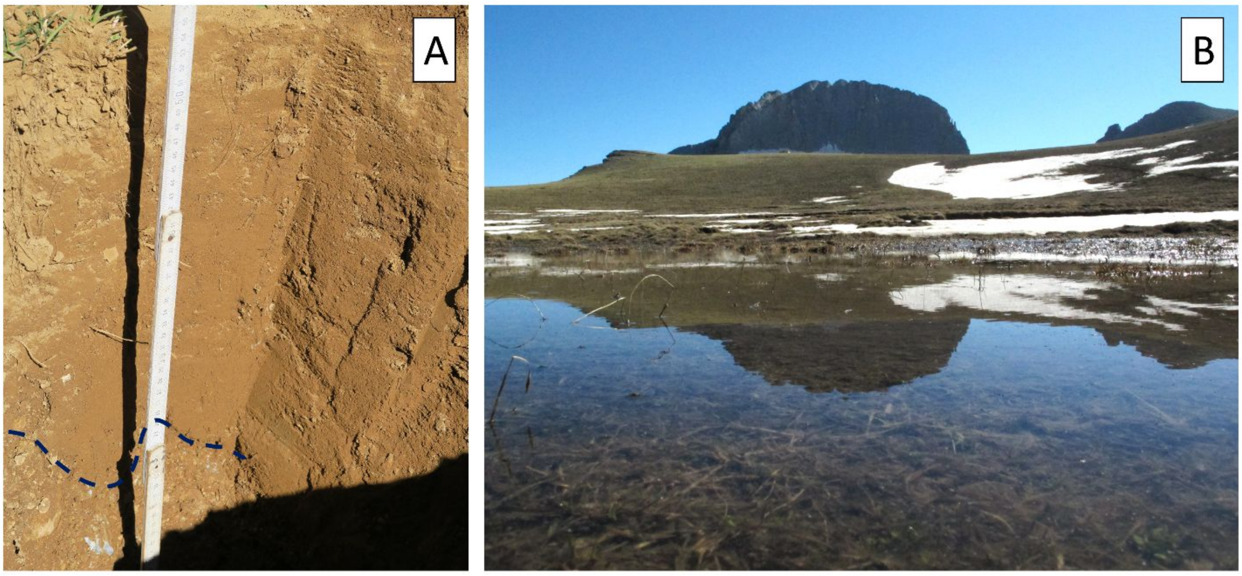

Figure 5. Cumulative grain size distributions of the soil samples from MK, TZ and PM Bw and Bt horizons (A, B, C and D). Surface sample PM1 (A, blue line) shows a distinct grain size distribution from the PM soil upper layer. Subplots E, F, G and H: Results of the CFLab fitting algorithm with the respective grain size distributions (GSD) and extracted grain size modes M1 to M5 (blue curves) of the soil samples PM1, PM15, TZ1 and MK2, represented as distinct sub-populations.

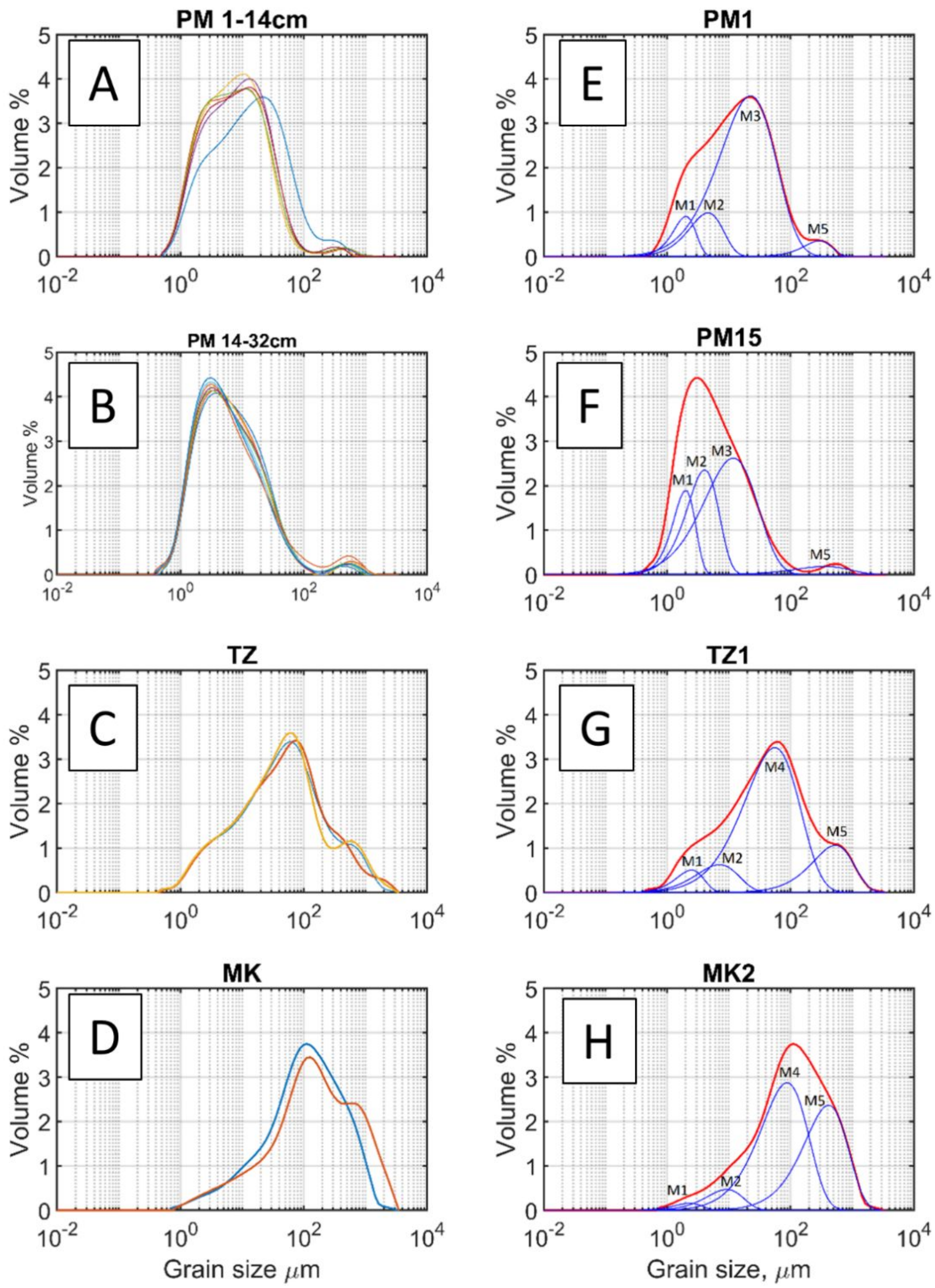

Figure 6. The PM soil profile along with the depth variations main textural classes. A transition layer between 14 and 16 cm of depth marks a substantial decrease in clay and increase in silt contents and a change in the dry soil color. For clarity reasons, it is noted that the direct depth measurement of the PM soil begins at 10 cm along the measurement tape, explaining the discrepancy between the actual and the illustrated depth. The photo was taken one day after the profile excavation, when the upper part had partly dried out.

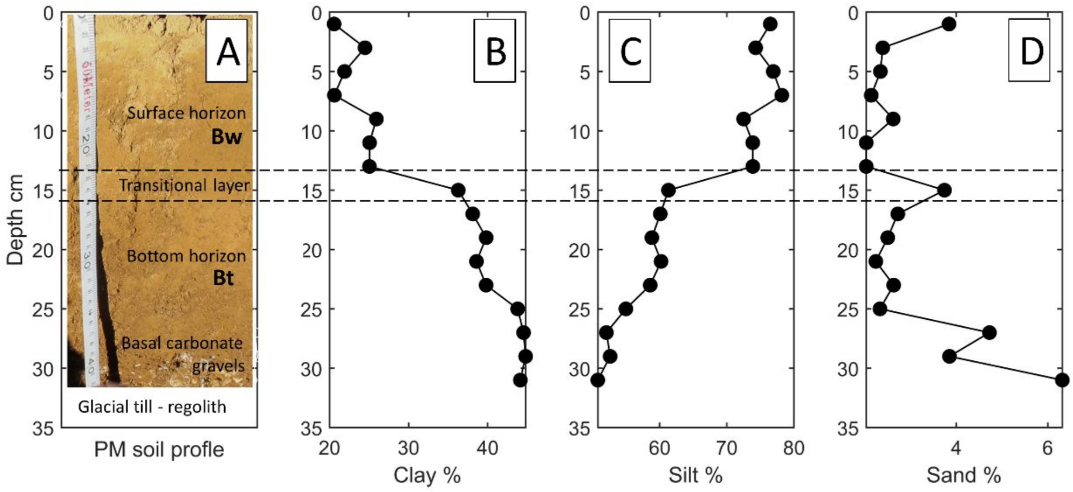

Figure 7. X-ray diffraction patterns of soil samples PM1, PM15, TZ1 and MK2. Soils within the hillslope high energy scree deposits are composed primarily of calcite. In contrast PM soil samples contain quartz, clays, feldspars, and mica. (M: mica, Chl/M: Chlorite and mixed layer clays, likely smectite, Chl/K: chlorite and likely kaolinite, K: K feldspar, Qz: quartz, Pl: plagioclase feldspars, Cc: calcite, Dol: Dolomite).

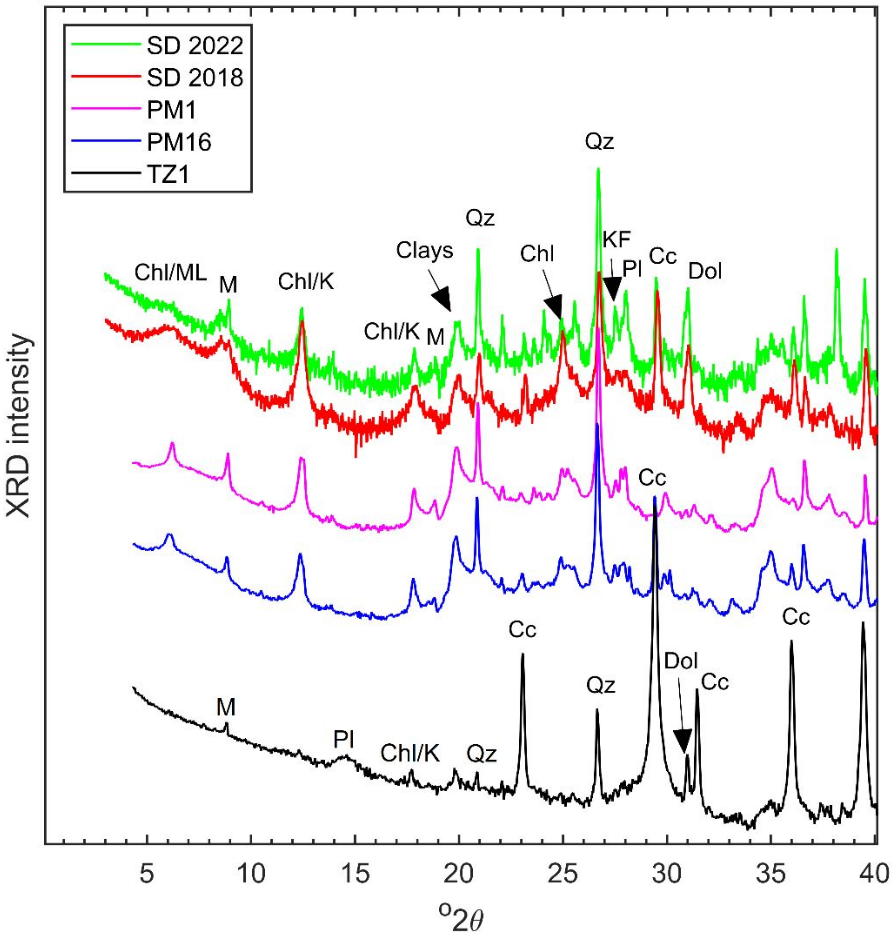

Figure 8. Depth variations of low and high frequency (A) and frequency dependent magnetic susceptibility (B) and (C) thermomagnetic analysis results of sample PM15 (red heating curve, blue cooling curve).

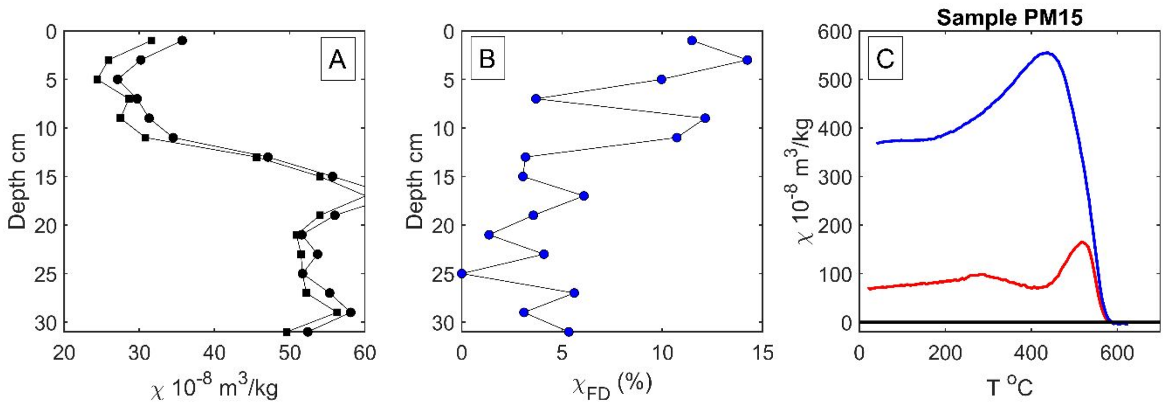

Figure 9. Plot of $^{87}Sr/^{86}Sr$ against ε_{ND} values of the PM soil samples with respective values of Mesozoic and Cretaceous carbonates (Franck et al., 2021), Mount Olympus granites (located on the continental west sides of the massif (Šarić et al., 2009, Castorina et al., 2020), Aegean Sea terrigenous and coastal sediments (Weldeab et al., 2002) and South Aegean marine sediments from Core SL 123 (Ehrmann et al., 2007), along with the three main North African dust source areas (PSA, Jewell et al., 2021). The isotopic enrichment trend for the PM soil samples towards crustal more radiogenic values occurs with a 25% increase in silt contents (colorbar) from the base to the surface of PM soil profile, suggesting the influence of external aeolian dust.

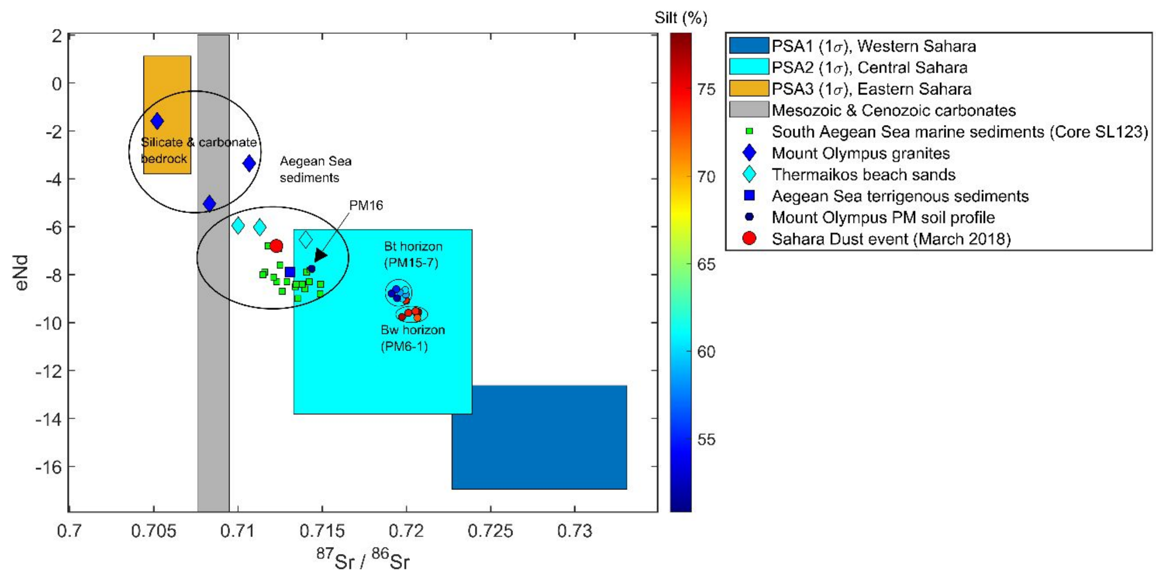

FIGURE 10. Estimates of the relative contributions of aeolian dust accretion to PM soil as calculated by mineralogical, and isotopic proxies.

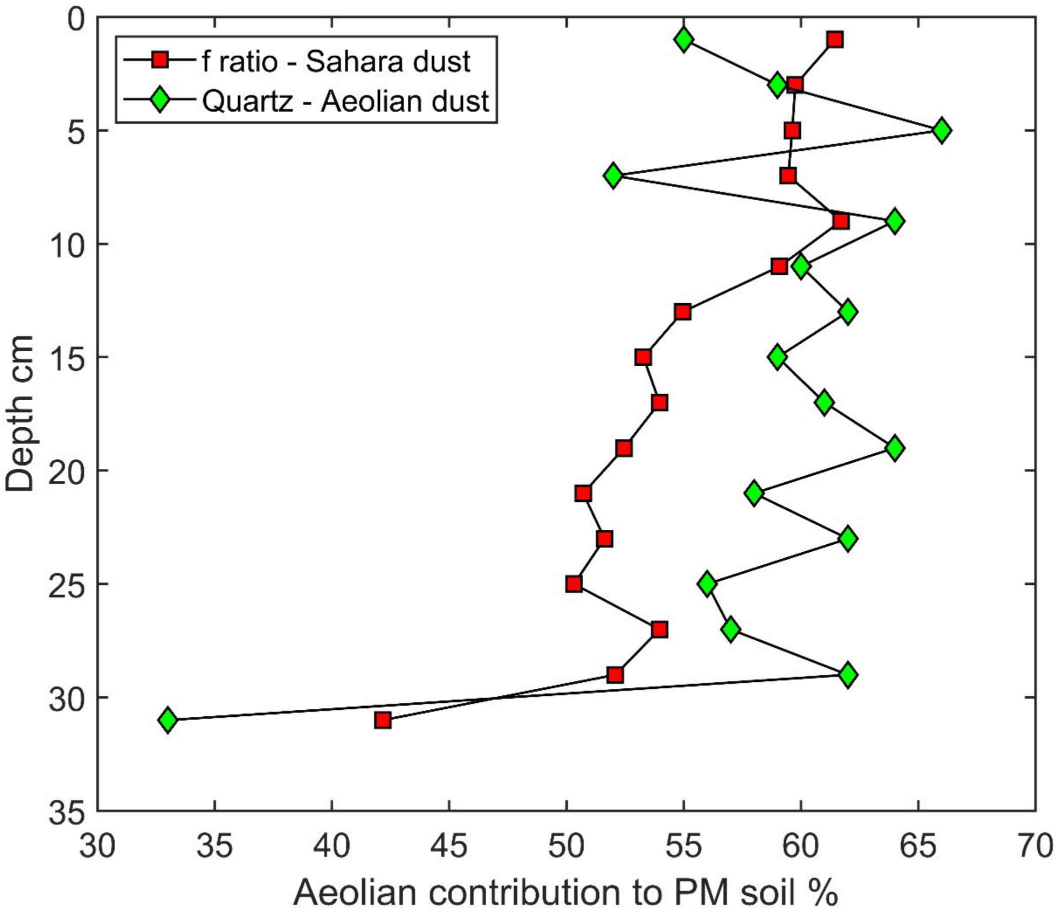

FIGURE 11. SEM backscatter images from selected samples of PM loess profile. (A) Calcite grains from basal sample PM 16. (B) Mixed phase of aluminosilicates with calcite, titanomagnetite and titanite from basal sample PM 16. (C). K-feldspar. (D) Quartz grain with rounded edges as a result of long-range aeolian transport. (E) Surface sample PM1 aggregate of aluminosilicates and Fe-Ti oxides. (F) Quartz grains of variable shapes and grain sizes from sample PM3 along with Fe-Ti oxides.

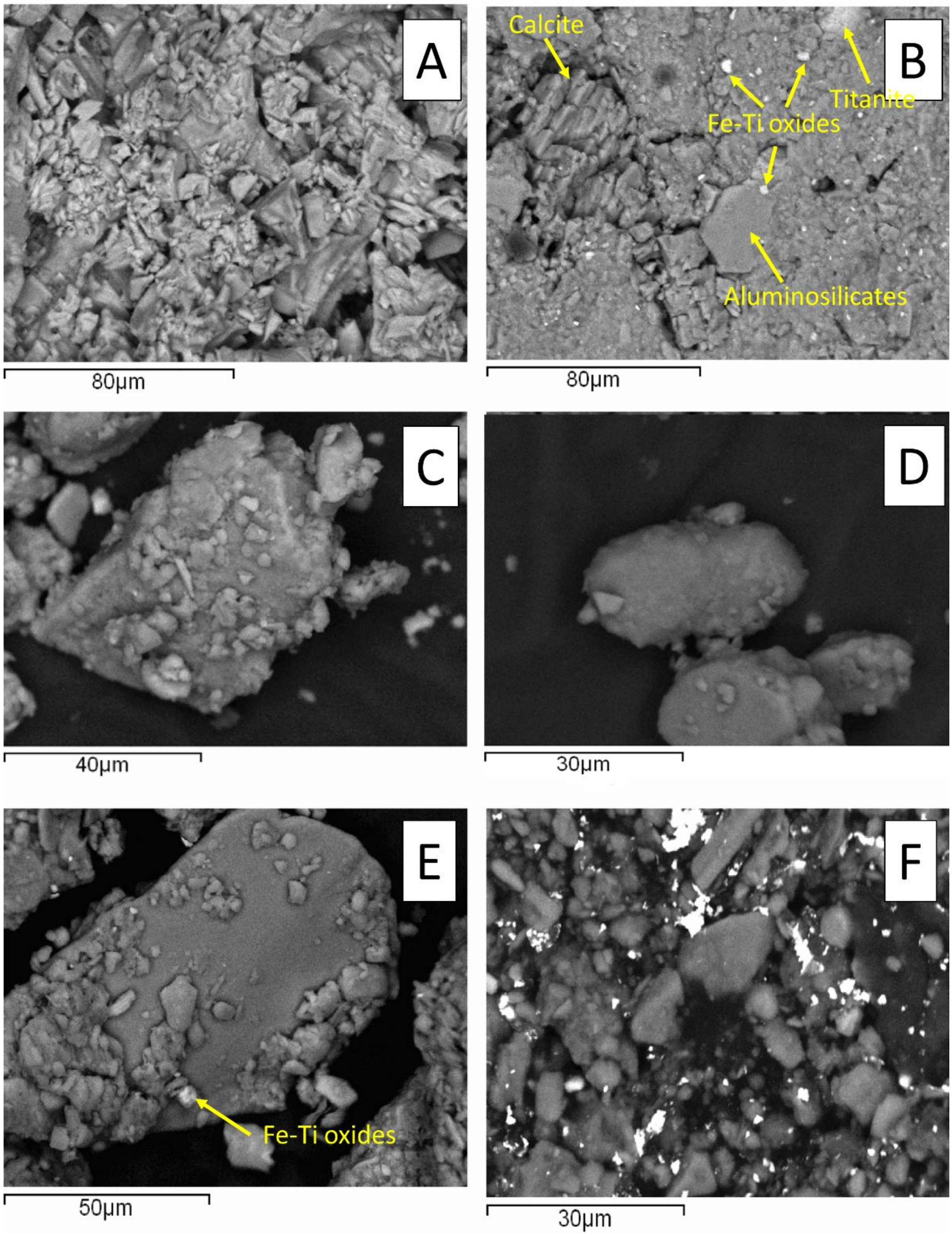

Table 1. Physical characteristics of the soil samples retrieved from the interbedded colluvial soils of the Megala Kazania (MK) and Throne of Zeus (TZ) scree slopes and from the alpine soil formed on the Plateau of Muses (PM).

Sample id	Depth below surface (cm)	Munsell color (dry)	Clay (%) M1 (<2µm)	Fine Silt (%) M2 (3.5-5µm)	Silt (%) M3 (14-30µm)	Fine sand (%) M4 (65-110µm)	Coarse sand (%) M5 (300-800µm)
MK1	30	5Y 6/1	1.7	6.6	0.0	39.8	51.9
MK2	250	5Y 6/1	0.0	11.4	0.0	47.5	41.1
TZ1	50	2.5Y 5/4	5.3	10.0	0.0	67.9	16.8
TZ2	150	10YR 3/4	6.0	25.2	0.0	43.5	25.3
TZ3	120	10YR 3/4	5.8	18.2	0.0	56.9	19.1
PM1	0-2	7.5YR 3/6	7.8	12.7	76.5	0.0	3.0
PM2	2-4	7.5YR 3/6	9.8	14.7	74.5	0.0	1.0
PM3	4-6	7.5YR 3/6	8.5	13.4	76.9	0.0	1.2
PM4	6-8	7.5YR 3/6	8.0	12.6	78.2	0.0	1.2
PM5	8-10	7.5YR 3/6	9.8	16.1	72.5	0.0	1.6
PM6	10-12	7.5YR 2/4	9.3	15.7	73.8	0.0	1.2
PM7	12-14	7.5YR 3/6	9.3	15.7	73.8	0.0	1.2
PM8	14-16	10YR 3/4	13.0	23.3	61.3	0.0	2.4
PM9	16-18	10YR 3/4	13.8	24.2	60.1	0.0	1.9
PM10	18-20	10YR 2/4	14.5	25.2	58.8	0.0	1.5
PM11	20-22	10YR 3/4	14.0	24.5	60.2	0.0	1.3
PM12	22-24	10YR 3/6	14.6	25.1	58.6	0.0	1.7
PM13	24-26	10YR 3/6	16.3	27.5	55.0	0.0	1.2

PM14	26-28	10YR 3/4	16.0	28.5	52.1	0.0	3.4
PM15	28-30	10YR 4/6	16.2	28.6	52.6	0.0	2.6
PM16	30-32	2.5YR 5/6	15.6	28.5	50.8	0.0	5.1

Table 2. Weight percent (wt %) mineralogical semi quantitative composition of the PM soil, along with the clay mineralogy of surface and base samples PM1 and PM15.

Sample id	Qtz	Chl_CC	Plag	KF	Mica	Amph	Cc	Clay mineralogy (<2µm) Sm / Kaol / Chl / Ill
PM1	55	21	14	3	7	0	0	Smectite: 45%, Kaolinite: 35%, Chlorite: 10%, Illite:10%
PM2	59	26	6	1	8	0	0	
PM3	66	21	4	2	7	0	0	
PM4	52	31	7	3	7	0	0	
PM5	64	22	7	0	7	0	0	
PM6	60	24	7	2	7	0	0	
PM7	62	20	4	6	8	0	0	
PM8	59	24	7	3	7	0	0	
PM9	61	24	7	3	5	0	0	
PM10	64	22	8	1	5	0	0	
PM11	58	28	4	3	7	0	0	
PM12	62	22	7	2	7	0	0	
PM13	56	25	5	1	7	6	0	
PM14	57	28	2	7	6	0	0	
PM15	62	24	6	4	4	0	0	Smectite: 65%, Kaolinite: 25%, Chlorite: 5%, Illite:5%
PM16	33	12	1	2	4	0	48	

Table 3. Radiogenic isotope results for the PM soil profile and the 2018 Sahara dust (SD) samples. εND values were calculated

Sample id	$^{87}Sr/^{86}Sr$	$^{87}Sr/^{86}Sr$ std err (%)	$^{143}Nd/^{144}Nd$	$^{143}Nd/^{144}Nd$ std. err. (%)	ε_{ND}
NBS 987 Sr standard	0.7102500	0.0008	-	-	
La Jolla Nd standard	-	-	0.5118500	0.0006	
PM1	0.7197322	0.0008	0.5121292	0.0004	-9.77
PM2	0.7201146	0.0026	0.5121383	0.0006	-9.60
PM3	0.7205816	0.0009	0.5121390	0.0006	-9.58
PM4	0.7207105	0.0010	0.5121399	0.0007	-9.56
PM5	0.7206530	0.0029	0.5121278	0.0009	-9.80
PM6	0.7205393	0.0007	0.5121419	0.0005	-9.52
PM7	0.7199828	0.0008	0.5121641	0.0005	-9.09
PM8	0.7196993	0.0009	0.5121731	0.0006	-8.91
PM9	0.7197594	0.0008	0.5121694	0.0005	-8.98
PM10	0.7199571	0.0007	0.5121775	0.0004	-8.82
PM11	0.7199244	0.0009	0.5121869	0.0006	-8.64
PM12	0.7196162	0.0008	0.5121820	0.0006	-8.74
PM13	0.7193930	0.0008	0.5121890	0.0006	-8.60
PM14	0.7194477	0.0009	0.5121694	0.0005	-8.98
PM15	0.7191162	0.0011	0.5121795	0.0004	-8.79
PM16	0.7143748	0.0016	0.5122328	0.0005	-7.75
SD 2018	0.7122721	0.0009	0.5122813	0.0006	-6.80

Aeolian dust accretion outpaces erosion in the formation of Mediterranean alpine soils. New evidence from the periglacial zone of Mount Olympus, Greece

Commented [A1]: The title has changed as the main question raised by this work is to examine the relative balance of aeolian dust accretion and local erosion in the periglacial zone of Mount Olympus in Greece, following the comments of Reviewr 1

Abstract

Soil formation in Mediterranean periglacial landscapes remains poorly understood as the interplay between erosion and aeolian dust accretion in providing parent materials, and mineral weathering and pedogenesis, as dominant post depositional processes, depends on a variety of local and regional factors. Herein, we investigate the balance between erosion and aeolian dust accretion in the formation of an alpine soil profile along a 2km erosional gradient of decreasing power in the northeastern Mediterranean alpine hinterland and specifically in the periglacial zone of Mount Olympus in Greece. We applied a wide range of analytical methods to 23 samples, from a soil profile developed in a glaciokarstic plateau, from sediment horizons interbedded in postglacial scree slopes and from modern Sahara dust samples deposited on the snowpack. Clast free horizons developed on scree slopes exhibit high concentrations of calcite rich sand and are representative local erosion products. The alpine soil B horizon developed on a glaciokarstic plateau contains high amounts of fine earth and is rich in quartz, mica, plagioclase, clays, and Fe-Ti oxides. Based on its physical and textural characteristics the soil profile is partitioned in a surficial weathered Bw horizon and a lower illuvial Bt horizon that overlies the local regolith composed of fragmented glacial till and slope wash sand and gravels. Radiogenic isotope systematics, grain size and mineralogical analysis show that the contribution of Sahara and locally sourced dust to the development of the soil B horizon ranges between 50 and 65%. Cryoturbation results in fine earth translocation from Bw to the Bt horizon, whereas weak pedogenetic modifications of detrital (aeolian and bedrock-derived) minerals result in magnetic mineral weathering and secondary clay (smectite and kaolinite) formation. Our findings reveal that, in addition to the low dissolution potential of the local regolith, aeolian dust accretion is the dominant process in providing alpine soil parent material and that cryoturbation, weak

pedogenesis, and mineral alteration occur within the Mediterranean periglacial zone of Mount Olympus.

Keywords: alpine soil; erosion; aeolian dust accretion; mineral weathering; Mediterranean periglacial zone, Mount Olympus

1. INTRODUCTION

Global glacier retreat and the melting of permafrost and ground ice have altered the dynamics of the alpine critical zone by enhancing erosion and by disturbing the production of mountain soils (Haeberli et al., 2006, Egli et al., 2014). During periods of glacial retreat and paraglacial adjustment, alpine soils develop from parent materials sourced through a combination of frost shattering, colluvial activity, and hillslope outwash (Egli and Poullenard, 2016). An equally important factor that affects the formation and evolution of alpine soils is the accretion of local and long-range transported aeolian dust (Muhs and Benedict, 2006; Küfmann 2008; Lawrence et al., 2013; Drewnik et al., 2014; Yang et al., 2016; Gild et al., 2018; Munroe et al., 2019). Thus, the contributions of physical erosion and aeolian dust accretion are fundamental sources of alpine soil parent material and largely define their textural, mineralogical, and geochemical characteristics.

The postglacial adjustment of alpine valleys is inherently linked to high rates of erosion, with frequent rockfalls, debris flows, rock avalanches, and high rates of sediment production especially below steep rockwalls. In such dynamic environments, alpine soil mantles formed on the surface of slope deposits are patchy, often truncated and constantly rejuvenated from rockfall material, whereas the evolution of these soils alternates between progressive and regressive phases (Egli et al., 2018). Similar soil mantles developed on sandy layers deposited on the surface of stratified scree slopes are generally indicative of quiescent periods of slope processes and are thus concise indicators of optimum climatic conditions and alpine landscape stability (Sanders et al., 2010). When the regional climate shifts to a colder regime, intense freeze–thaw activity and frost cracking enhance rockfall activity and result in the erosion and gradual burial of these incipient soil mantles. As hillslope processes and scree slope aggradation diminish away from the alpine steep rockwalls, the development of alpine soils on distal moraines, outwash plains, and glacially scoured plateaus can be considered continuous (*sensu lato*). In these depositional environments, low erosional rates provide ample time for pedogenetic processes such as chemical weathering, mineral alteration, elemental translocation, and illuviation to occur, whereas other physical processes, such as cryoturbation

Commented [A2]: Removed 'discontinuous' soil-sediment accumulations (hereafter 'soils') and replaced with 'soils'

Commented [A3]: Illuviation is included to pedogenetic processes disturb the soil profiles. Alpine soils are an important component of high mountain ecosystems, so a better understanding of the processes that drive their formation in climatically sensitive regions, like the Mediterranean, is required.

Most soils formed in the Mediterranean basin display a distinguishable red color (terra rossa) that derives from high concentrations of ultra-fine pedogenic iron oxides, mainly hematite (Yaalon, 1997; Durn et al., 1999). Terra rossa soils receive significant aeolian dust additions from Sahara and Sahel regions (Yaalon, 1997; Durn, 2003; Stuut et al., 2009). In the Mediterranean alpine hinterland, thin drapes of Sahara-dust-rich soils are found on plateaus, glacial moraines, and outwash plains (e.g., Rellini et al., 2009), whereas aeolian dust accretion in terra rossa soils can also originate from a wide range of alluvial deposits, such as sand dunes, desiccated alluvial planes, and Quaternary loess (Amit et al., 2020; Lehmkuhl et al., 2020). Most of the Mediterranean mountains are built up by carbonate rocks, hence the aeolian input to alpine soil formation occurs in parallel with colluvial deposition of carbonate erosion and dissolution products that form a characteristic insoluble residue incorporated in the soil sequences (Durn 2003; Varga et al., 2016; Kirsten and Heinrich, 2022).

In the present study, we investigate the major processes that drive the postglacial formation of Mediterranean alpine soils in the periglacial landscapes of Mount Olympus, Greece. We follow a combined sedimentological, mineralogical, and isotopic approach, and present a detailed characterization of distinct alpine sediment and soil horizons developed across a geomorphological gradient of decreasing erosive power. Discrete sediment samples from intact sandy layers interbedded in postglacial stratified scree slope deposits that represent *in situ* erosional products of the periglacial zone of Mount Olympus, are compared with samples from a soil profile developed in a glaciokarstic plateau, with a goal to assess the relative contributions of aeolian dust accretion to the fine fraction of an alpine soil. We differentiate between the physical and chemical processes that drive the production of the scree slope sandy layers and of the alpine soil profile, by comparing their respective grain size distributions, and bulk mineralogy. Furthermore, we examine the potential influence of Sahara and locally sourced aeolian dust accretion on the alpine soil profile by comparing

Commented [A4]: Hematite is an iron oxide, so the phrase has been changed accordingly

Commented [A5]: Wording is clarified.

Commented [A6]: The sentence has changed, so that it clearly represents the goal of this work, as stated in the new title of the manuscript.

the sedimentological, mineralogical, and radiogenic isotope compositions through the application of $^{86}Sr/^{87}Sr$ and $^{143}Nd/^{144}Nd$ ratios between the soil samples and Sahara dust samples collected from the snowpack. We finally measured the magnetic properties of the soil samples and clay mineralogy of bottom and topsoil layers, to assess the potential for weathering of clay minerals and iron oxides within Mount Olympus periglacial zone. Understanding the sources of parent materials and soil formation processes between contrasting geomorphological settings is a fundamental step towards defining the postglacial paleo-environmental history of Mount Olympus alpine landscapes that followed pronounced shifts of the regional climate.

Commented [A7]: We changed the sentence and replaced the 'potential for pedogenesis' with 'potential weathering of iron oxides', which corresponds directly to the analyses undertaken and to the overall goal of the manuscript

2 BACKGROUND

2.1 Mount Olympus glacial history

Mount Olympus is the highest mountain in Greece, rising 2918 m above the northwest coastline of the Aegean Sea (Figure 1a). It is a precipitous massif with a circular shape composed of Triassic to Cretaceous metacarbonates, uplifted along a frontal fault that runs parallel to the present-day shoreline. Mount Olympus is exhumed from the silicate crystalline bedrock, which dominates the lithology of Pieria Mountains (granites, ophiolites) to the north and east, and Mount Olympus granites to the west (Figure 1B). High uplift rates along with successive Quaternary glaciations have created the present-day rugged terrain. The deglaciation of Mount Olympus since the Last Glacial Maximum (LGM), between 28 and 24 ka BP (Allard et al., 2020), triggered the rapid retreat of an ice cap that was covering the summit area and extended down to elevations of □1800 m (Kuhlemann et al., 2008). The post-LGM glacier retreat was intercepted by a glacier re-advance phase at □15 ka BP that was limited at the highest cirques above 2200 m at □12.5 ka BP (Styllas et al., 2018). This latter phase of glacial expanse is traced in both Megala Kazania (MK) and Throne of Zeus (TZ) cirques (Figure 1C). The absence of absolutely dated glacial features between early- and mid-Holocene (9–4 ka BP) in both cirques suggests reduced glacial activity, whereas Late Holocene (4 ka BP to present) glacier advances have been observed only in the MK cirque (Figure 1C). These include a terminal moraine stabilization phase at □2.5 ka BP followed by a smaller expansion of the MK glacier at the beginning of the Little Ice Age (LIA) at □0.6 ka BP (Styllas, 2020). Late Holocene glacier advances in the MK cirque lack similarly dated glacial landforms in the TZ cirque, but we cannot rule out the possibility that the Late Holocene climatic shifts towards glacial conditions triggered an intensification of glacial and periglacial processes, which in turn affected the late Holocene landscape evolution, scree slope aggradation and alpine soil production.

2.2 Climate

The contemporary maritime conditions and the steep relief of Mount Olympus result in intense precipitation and temperature altitudinal gradients, with the highest peaks constituting an orographic and climatic barrier between the eastern (marine) and western (continental) sides (Figure 1b, Styllas and Kaskaoutis, 2018). The climate in the coastal zone is typically Mediterranean, whereas at higher elevations (1000–2200 m), the climate attains sub-Mediterranean characteristics with average annual precipitation of 1300 mm (Styllas et al., 2016). In the alpine zone above the tree line (2400 m), the climate is characterized by temperate conditions with annual precipitation above 2000 mm and average annual temperatures between 0 and 1.5 °C (Styllas et al., 2016). The periglacial activity in the Mount Olympus alpine zone is likely still active today, as it is situated just above the lower limit of the regional permafrost zone (2700m) of the southern Balkan peninsular (Dobiński, 2005).

2.3 The Plateau of Muses

The Plateau of Muses (PM) is a planar depositional surface located at an elevation of 2600 m with a surface area of 1 km^2. It resembles a typical alpine meadow, partly covered by alpine grass vegetation that shares similar characteristics with plateaus found in the high Balkan Mountains and the European Alps. The PM is bounded to the south by the TZ cirque lateral moraine ridge and by several gentle-sloping glacially eroded peaks along its northern, eastern, and western margins (Figure 1C). The formation of the plateau has resulted from the combined action of glacial scouring and carbonate bedrock dissolution. Its low relief in combination with the circular shape suggest a doline type karstic depression that is filled with glacial till, overlain by colluvial sediments (slope wash) transported from the adjacent slopes. The surface layer of the PM sedimentary sequence comprises a developed soil sequence with variable thickness (30–50 cm) that overlies a layer of outwash sand and fine gravels and/or fragmented till boulders, and exhibits brown-red to yellow color hues, which in the Munsell color scale range between 7.5 and 10 YR (Table 1). Alternating patches of alpine grass vegetation and hummocky soil pans in the center of the plateau are indicative of periglacial activity and cryoturbation. Other periglacial features such as solifluction-terraced stripes below the bare bedrock of the surrounding summits are tentatively considered to have formed during the Late Holocene cold stages, during the observed expansion of small glaciers in the MK cirque.

3 MATERIALS AND METHODS

3.1 Erosional products and alpine soil sampling

To adequately address the question of the relative balance between aeolian dust accretion and local erosion of moraines and scree slopes to the development of the alpine soil on Mount Olympus periglacial zone, a wide range of methods were employed and involved the analyses of 21 discrete soil and sediment samples retrieved along a transect of decreasing hillslope energy and erosional power (Figure 2). Five samples (n=5) were retrieved from clast-free sandy horizons interbedded in the relatively young (Late Holocene) MK and older (early Holocene) TZ stratified scree slopes, and sixteen (n=16) were sampled from the PM soil sequence at 2-cm intervals (Table 1). The specific experimental setting was selected to evaluate the impact of physical weathering on providing the base material for the development of the PM soil. We only sampled naturally exposed clast free sandy layers found within the scree slopes of MK and TZ. We considered that these layers share

Commented [A8]: We elaborate on the study's experimental design and explain the selection of the specific sampling sites.

similar textural, mineralogical, and geochemical characteristics with the PM soil basal horizon, which lies on a layer of outwash sand and gravels. Luckily, we were able to retrieve the samples from two distinct interbedded clast free sediment layers within the TZ scree slope after a torrential rainfall event that opened a deep erosional trench in the scree below the rockwall and reached the basal till layer (Figure 2). The scree slope in the MK is regularly eroded and scoured from a perennial snowfield that is retreating by the end of the summer season, and this made the sampling of distinct soil-sediment horizons straightforward. We manually excavated only one pit for high resolution soil sampling and considered that due to the very small surface area of the surficial soil apron within the PM catchment (0.06 km^2), the specific profile is representative of the PM soil development. We selected a location in the center of a circular soil-sediment pan that was free of vegetation, surface carbonate fragments (Figure 2). After sampling, the pit was closed and refilled with the excavated material in accordance with Mount Olympus National Park directions. In locations with long lasting snowpack, we observed a humic A horizon, but since these locations host several endemic flower species, the Management Unit of Mount Olympus National Park, did not grant permission to excavate a soil pit in these sensitive sites. The PM soil samples were additionally subjected to microscopic and radiogenic isotope analyses and magnetic measurements to investigate the potential chemical alterations processes during PM soil development. Mineralogical and radiogenic isotope analyses were also performed in two (n = 2) samples of aeolian dust that were deposited on the PM snowpack during the spring seasons of 2018 and 2022. The long-range aeolian dust transport episodes occurred on March 22–24, 2018, and March 16–18, 2022. The synoptic conditions of these distinct episodes show that the dust emissions traveled to Mount Olympus from the Sahara Desert and left an orange hue on the snowpack, which later in the spring season formed distinct layers in the snowpack (Figure 3). We therefore consider the samples collected from the PM snowpack as representative of Sahara dust accretion in Mount Olympus alpine soils.

3.2 Grain size analyses

The soil samples were transported to the lab, wet sieved through a 3.5-mm sieve, and treated with 30% hydrogen peroxide (H_2O_2) at 70 °C for 12 h to remove organic matter. The H_2O_2 treatment was repeated three times until the samples were completely bleached and all organic matter was degraded. The samples were washed with distilled water and analyzed with a Mastersizer 3000 laser diffraction particle-size analyzer to define the bulk grain size distributions of the sand, silt, and clay fractions. The samples were run through the automated dispersion unit and sodium hexametaphosphate solution (Calgon) was added as dispersion factor. Statistical analyses of the grain size distributions and derivation of the clay, silt, and sand fractions were realized with MATLAB Curve Fitting Lab (CFLab), which performs curve fitting on sediment grain size distributions using the Weibull probability distribution function (Wu et al., 2020).

Commented [A9]: This has been a typographical error in the previous versions of the manuscript. We sieved the soil and sediment samples through a 3.5mm sieve. We also include an Excel file with the results of the Mastersizer 3000 grain-size analyses to provide further evidence for this error.

3.3 Mineralogy

Identification of the mineral phases of the soil and aeolian dust bulk samples was achieved through X-ray diffraction (XRD, Philips diffractometer PW1800, Co radiation at 40 kV and 40 mA), and two samples from the top and base of the PM soil profile (PM1 and PM15) were additionally analyzed for their clay (<2 µm) mineralogy through ethylene glycolation and heating for 2 h at 550 °C. The PM soil samples semi-quantitative composition of the main mineral phases (e.g., quartz, feldspar, plagioclase, micas, calcite) was determined using MAUD-Material Analysis software applied for full pattern Rietveld refinement (Lutterotti et al. 2007) and is expressed as weight percent (wt %) concentrations.

Commented [A10]: Typo has been corrected

3.4 Petrographic, magnetic, and isotopic analyses

Additional analytical methods were applied only to the PM soil samples to assess the potential sources of soil-forming material, pedogenesis, and chemical weathering. The fabric configuration of the PM alpine soil was explored through scanning electron microscopy–energy dispersive spectrometry (SEM–EDS) analyses (JEOL JSM-840A equipped with an INCA 250; Oxford) with a 20-kV accelerating voltage and 0.4-mA probe current. Backscattered electron images (BSE) enabled us to detect the shapes of different minerals, and the physical weathering features of specific grains, whereas with the EDS analysis we examined areas of different chemical composition within the same soil aggregates.

Commented [A11]: Exotic particles has been removed.

We additionally explored the existence of ferromagnetic components and the potential for secondary iron oxides formation in the PM soil profile through magnetic susceptibility measurements. The discrete samples were packed in cubical plastic boxes (2 × 2 × 2 cm) and weighed before the measurements. Volume-specific magnetic susceptibility measurements were performed using both a Bartington dual MS2B sensor at low and high frequencies of 0.465 and 4.65 kHz. The results are expressed as mass-specific magnetic susceptibility (χ; 10^{-8} m^3/kg). During the measuring procedure, every sample was measured at least three times and the average value was assigned as the final measurement. For each sample, two air measurements were performed before and after sample measurement. The frequency-dependent susceptibility (χ_{FD}; %) was calculated according to Dearing et al. (1996):

Commented [A12]: "Potential for pedogenesis' is replaced and further explained.

$$\chi FD\% = \frac{100(\chi LF - \chi HF)}{\chi LF} \quad (1)$$

where χ_{LF}, χ_{HF}, are the magnetic susceptibility at low and high frequency, respectively. Samples PM16 and PM15, which were considered as more representative of the PM soil regolith boundary, were additionally subjected to thermomagnetic analysis to define the origin of the ferromagnetic particles at the base of the PM soil. Measurements of continuous thermomagnetic curves (K–T curves) at low and high temperature were realized with the furnace CS3 of the AGICO MFK1-FA susceptibilimeter.

The potential sources of the PM soil and aeolian dust were evaluated through their Sr and Nd isotopic ratios. Isotopic measurements were performed at the University of Arizona TIMS laboratory following the procedure in Conroy et al. (2013) on soil samples. Samples were not spiked and dissolved in mixtures of ultrapure Hf-HNO3 acid. Elemental separation of dissolved samples was carried out in chromatographic columns via HCl elution in a clean laboratory environment. Conventional cation columns filled with AG50W-X4 resin were used for Sr and REEs separation and anion columns with LN Spec resin for Nd separation following Ducea et al. (2020). Sr cuts were loaded onto Ta single filaments and Nd cuts onto Re filaments. $^{87}Sr/^{86}Sr$ and $^{143}Nd/^{144}Nd$ ratios (Table 3) were measured on a VG Sector 54 thermal ionization mass spectrometer (TIMS) fitted with adjustable 1011 Ω Faraday collectors and Daly photomultipliers. NBS SRM 987 Sr standard and La Jolla Nd standard were analyzed during the samples run to ensure the performance of the instrument and to perform some minor correction on the final reported ratios.

3.5 Erosional potential and aeolian dust accretion proxies

The erosional potential of the three sampling sites, which are distanced along a 2km transect was derived from field estimates of the vertical height of the MK and TZ rocky headwalls and their scree slopes. We evaluated the plateau and scree slope energy distribution and maturity stage from the dimensionless ratio between the vertical height of the scree slope (Ht) to the vertical height of the headwall (Hc) following Statham (1976) (Figure 2).

Commented [A13]: The paragraph was moved to methods according to Reviewer's 1 suggestion.

To assess the potential contribution of distal and local aeolian dust inputs in the PM soil we used the contents of quartz (wt. %). The source of quartz can be local, from the Pieria Mountains silicate bedrock and from the granites to the west of Mount Olympus, or can be transported during Sahara dust episodes, as evidenced from the XRD analyses of the PM snowpack samples, which are in line with Sahara dust samples from the Pyrenees, the European Alps, and the Carpathian Mountains that contain high amounts of quartz (e.g., Rellini et al., 2009; Rodriguez-Navarro, 2018; Marmureanu et al., 2019). Herein, we cannot exclude the possibility of quartz release from the local bedrock through periglacial erosion, but the amount of quartz released from local bedrock dissolution is expected to be small, wt.% concentration of the insoluble residue from carbonates in Greece is less than 1% (MacLeod, 1980; Kantiranis, 2001; Kirsten and Heinrich, 2022). Therefore, it is reasonable to consider quartz (wt. %) as a reliable proxy of aeolian dust accretion.

Commented [A14]: Responding to Reviwer 1 comment that quartz is not a reliable proxy of aeolian dust, we provide references that the potential contribution of uartz from the local bedrock is minimal and that quartz has been found to dominate Sahara dust deposits on the snowpack of several mountain ranges.

We selected the ε_{Nd} ratio as a second independent proxy particularly of Sahara dust accretion in the PM soil. We did not use the Sr ratio ($^{87}Sr/^{86}Sr$) as it can be impacted by the dissolution of carbonate particles and replacement of Ca by Sr during pedogenetic alteration of the PM soil (e.g., Shalev et al., 2013). Sr isotopic distributions of PM soil can be further complicated by the accretion of sea-salt Sr through orographic precipitation (Kurtz et al., 2001). Rain is not a significant source of Nd, so the addition of rainwater and snow should not affect the Nd isotopic composition of the aeolian dust, so ε_{Nd} is buffered against these changes (Kurtz et al., 2001). We estimated the fraction of Sahara dust from the ε_{Nd} ratios of the PM soil, the dust deposited on the snowpack, and the local bedrock following the method by Kurtz et al (2001):

$$f = \frac{(\varepsilon\text{Nd PM soil} - \varepsilon\text{Nd bedrock})}{(\varepsilon\text{Nd Sahara dust} - \varepsilon\text{Nd bedrock})} \quad (2)$$

As we had not obtained direct Sr and ε_{Nd} values from Mount Olympus bedrock, we used the value of the basal sample PM 16, which is dominated by bedrock derived calcite and falls in the same value range with basin-average values of terrestrial, coastal, and marine sediments deposited in the Aegean Sea (Weldeab et al., 2001).

Commented [A15]: Sample PM 16 is sandy and gravely and is characterized by similar values with the Aegean Sea sediments (see Figure 10), so we considered the average Sr-eNd values representative of the regional carbonates.

4 RESULTS

4.1 Alpine soil formation across a hillslope energy gradient

According to Statham (1976), Ht/Hc values above 0.4 characterize a mature scree slope, which is the case for the TZ (0.6) but not for the MK (0.3) scree slope, and this reflects the older deglaciation age of the TZ cirque (□12.5 ka BP, Section 2.1). The MK scree slope is deposited behind the LIA moraine (Figure 1C), so that the most recent deglaciation processes (☐0.6 ka BP to present) has resulted in immature scree development. Conversely, the low-relief, low-erosion PM acts as a long-term depocenter of slope wash and detrital (aeolian and bedrock derived through freeze-thaw action) sediments. For this low-energy setting, we believe that minor colluvial contributions, cryoturbation, aeolian dust accretion, fine earth translocation, and post-depositional mineral alteration are the major drivers of PM soil production. The irregular boundary between the base of the PM soil and the

Commented [A16]: Sepculative expressions have been chang to affirmative ones.

Commented [A17]: Sentence has been deleted.

underlying regolith composed of glacial till and outwash gravels, is indicative of cryoturbation, while observations of late-season soil freezing and waterlogging (Figure 4) provide permissive evidence that PM soil development is disturbed by cryogenic processes. The energy gradient along the contrasting environments impacts the soil color. The PM soil basal layer overlying the regolith shares similar color characteristics with the MK samples and with the TZ upper sediment horizon, which have grey to olive green hues (Munsell dry color 2.5– 5 Y; Table 1). Conversely, the lower clast-free sediment horizon of the TZ scree shares similar Munsell dry color characteristics with the PM soil, characterized by red-brown to yellow hues (7.5–10 YR, Table 1), suggesting that these soil samples are more oxidized and are undergoing pedogenetic alterations.

4.2 Grain size variation

The interactions between slope processes, colluvial sediment transport, and aeolian sub additions result in polymodal grain size distributions that display different shapes among MK, TZ, and PM soils. Five grain size modes (M1 to M5) were mathematically derived from the application of the CFLab curve-fitting algorithm. Fitting degrees were >99% and fitting residuals were <0.1%, indicating excellent fits for the raw grain size distribution curves (Figure 5 A, B, C, and D). The fine-earth (clay and silt) fractions resemble grain size modes M1 and M2 with respective mean grain sizes of □2 and □4 µm and M3 with mean grain sizes between 10 and 30 µm. The sand fraction is composed of two modal sub-populations: a fine-sand-grain size mode (M4, mean grain size □80 µm) and a coarse sand-grain size mode (M5, mean grain size 440 µm) (Figure 5 E, F, G, and H; Table 1). The production of coarse sand is transported to the respective interbedded sediment horizons by rockfall activity and colluvial processes, or in the case of the low-sloping PM, through slope wash. The fine sand (M4) subpopulation was not traced in the PM soil samples, and this can be linked to either selective entrainment of M4 or to distortion of the MK and TZ grain size curves and truncation of the coarser modes (Garzanti et al., 2009).

Commented [A18]: As previously stated, there has been a typo in the previous versions of the manuscript, as the range of the sieved sediments and soil samples was 3.5mm.

Commented [A19]: Following the comments of Reviewer 1, we removed the sentence "The presence of fine (M4) and coarse (M5) sand is linked to frost weathering of the carbonate bedrock." as we do not have adequate evidence to support this.

In addition to the distinct color variations, the contrasting slope-energy distribution between the MK, TZ scree slopes and the PM depositional environments also defines their textural compositions. Sediment horizons developed on the surface of the MK scree slope contain higher amounts of sand (□90%) and lower amounts of silt and clay (□10%) compared with their TZ counterparts (□75% and □25%), implying that the dominance of sand in the sediment horizons of the scree slopes derives from freeze-thaw and colluvial activity. The coarse-sand content (M5) of the PM soil basal layer is 6% but is lower within the solum (2%–3%), suggesting either reduced periglacial activity and/or low transport capacity of erosional products from the catchment through slope wash processes during the PM soil formation (Table 1; Figure 2, lower graphs).

Commented [A20]: Based on these observation we conclude that the sand populations are highest in the immature scree slope interbedded sediment layers and thus sand can be considered representative of periglacial erosion.

The grain size distribution curves of the PM soil present a significant change in shape between soil depths of 14 and 16 cm, which is characterized by a 15% reduction of the clay and very-fine-silt fractions (M1 and M2) and by a similar increase of silt contents (Figure 5A and B). This sharp textural differentiation was not supported from field observations, where the solum appeared homogenous without distinct pedogenetic horizons and without any visual evidence of an erosional layer (Figure 6A), but it is supported by changes in the soil color. The samples above a soil depth of 14–16 cm exhibit red to brown hues (7.5 YR), whereas the samples below this layer have more yellow-red (10 YR) hues (Table 1). We also observed clay coatings in sparse secondary carbonates (calcretes) along the lower part of the PM soil profile, which we interpret as evidence of soil mixing and downward translocation of dissolved Ca and secondary calcite precipitation at the base of the soil profile. Based on these observations, we partitioned the PM soil profile in two horizons: an upper Bw horizon between 0 and 14 cm with red to brown hues, low clay (□25%), and high silt (□75%) contents, and a lower illuvial Bt horizon between 14 and 32 cm with higher (□40%) clay contents, a yellow-red hue, and smaller amounts (□5%) of sand compared with the overlying Bw horizon (Figure 6).

4.3 Soil and aeolian dust mineralogy

XRD analysis of the bulk samples reveals a mineralogy that substantially differs between the MK, TZ, and PM soils and, like the soil colorization and textural variations, follows the erosional slope gradient. The most dominant mineral phase in the clast-free material of the MK and TZ soils is calcite. Other minerals identified include dolomite along with quartz and micas. Conversely, the bulk mineralogical composition of PM soil exhibits a richer matrix of minerals that includes quartz, chlorite and mixed layer clays, mica, potassium feldspars, and plagioclase (Figure 7). Calcite is dominant (□50%) only in basal sample PM16 (Figure 6; Table 2). Quartz, clays, and mica are the most dominant mineral phases in the PM soil (□80%) with low values in basal sample PM16, whereas plagioclase, K-feldspar, and mica represent the remaining 20% (Table 2). Semi-quantitative analysis of the clay mineralogy of two samples retrieved from the surface of the Bw horizon and the base of the Bt horizon (samples PM1 and PM15) revealed high concentrations of smectite and kaolinite (80%) and low contents of chlorite and illite. Surface sample PM1 contains 45% smectite and 35% kaolinite, whereas basal sample PM15 has higher smectite (65%) and lower kaolinite (25%) contents (Table 2).

From the comparison of the XRD spectra (Figure 7), it is obvious that the bulk mineralogy of the PM soil matches that of the Sahara dust samples. Both Sahara dust samples show the presence of clay minerals, quartz, mica, calcite, plagioclase, K-feldspar, and dolomite. The detected mineral phases are typical of Saharan dust deposited in Europe during both dry- and wet-deposition (red rains) events (Scheuvens et al., 2013). Additionally, recent studies of Saharan dust wet deposition in the Iberian Peninsula also indicated the presence of Fe-Ti oxides, such as goethite and hematite, and of Ti oxides, such as rutile (Rodriguez-Navarro et al., 2018), but these were not depicted from our XRD analyses. Despite their overall XRD spectral similarity, a pronounced difference between the contemporary Sahara dust and PM soil samples is the presence of calcite and dolomite in the dust samples and their near absence from the PM soil profile (Figure 7). The smooth and low intensity peaks for calcite and dolomite at 29.43 and 30.7 2ϑ in surface sample PM1 indicate the partial removal of calcite, whereas similarly subdued peaks in basal sample PM16 denote near complete decalcification of the solum (Figure 7).

4.4 Magnetic susceptibility of PM soil

The magnetic susceptibilities of the PM soil bulk samples were measured to provide insight into the ferromagnetic components of the PM soil and their potential alterations. Overall, the low-frequency magnetic susceptibility (χ_{lf}) is higher in the lower Bt horizon, with average values for samples PM8–PM16 of 55 × 10^{-8} m^3 kg^{-1}, and lower χ_{lf} values in the Bw horizon, with average values for samples PM1–PM7 of 36 × 10^{-8} m^3 kg^{-1} (Figure 8A). Similar value ranges were measured for the high-frequency magnetic susceptibility (χ_{hf}). The estimated values of frequency-dependent (χ_{FD}) susceptibility presenting a wide range of values ranging between 0% (sample PM13) and 14%, with significantly higher values in the Bw horizon (Figure 8B). According to Dearing (1999), high χ_{FD} values (>10%) are indicative of the presence of superparamagnetic Fe oxide nanoparticles (< 0.05 µm), suggesting a higher amount of fine ferrimagnetic grains in the surface horizon Bw, which potentially can be of detrital (aeolian and/ eroded bedrock) origin.

The mineral phases responsible for the magnetic enhancement of the Bt horizon were deduced from high-temperature magnetic susceptibility measurements performed during a single heating–cooling cycle to 700 °C (Figure 8C). We estimated the Curie temperature (T_c) of samples PM16 and PM15 to examine the potential existence of superparamagnetic ultrafine particles in the base of the PM soil profile, which is in contact with the regolith. The thermomagnetic analysis of sample PM16 failed completely, likely due to its high calcite content and absence of magnetic phases. On the other hand, sample PM15 resembling the soil-regolith lower boundary, revealed a uniform χ-T behavior that is indicative of the dominance of two magnetic phases (Figure 8C) – one with Tc, or transformation temperature, between 260–320 ◦C, probably maghemite, and a second one around

600 ◦C, which is typical for oxidized magnetite (Jordanova et al., 2022). Since the nano-sized pedogenic magnetite is unstable upon heating (Dunlop and Özdemir, 1997), the identified oxidized magnetite suggests that weak pedogenetic production of ferromagnetic components occurs in the base of PM soil profile.

4.5 Radiogenic isotopes

More information on the provenance of the PM-soil-forming material was derived from the radiogenic isotope analysis of the soil samples and of the 2018 Sahara dust sample. The $^{87}Sr/^{86}Sr$ values of PM soil samples range from 0.71437 to 0.72071 and the ε_{Nd} values from -7.75 to -9.80 (Table 3). Overall, the PM soil $^{87}Sr/^{86}Sr$ – ε_{ND} cluster together apart from sample PM16, which has the lowest value of the PM soil $^{87}Sr/^{86}Sr$ ratio (Figure 9). The analyzed Sahara dust sample exhibits $^{87}Sr/^{86}Sr$ value of 0.71272 that falls within the lower range of North African dust sources between □0.71200 and 0.74000 (Erel and Torrent, 2010; Grousset and Biscaye, 2005). The Sr isotopic ratio of the Sahara dust sample shows potential mixing with rainwater and local sea salt aerosols during the March 2018 wet deposition event but also with other European aerosol sources, which is validated by the fact that the dust plume of the March 2018 travelled over Europe before it reached Mount Olympus (Figure 3A). The Sahara dust sample has an ε_{Nd} value of –6.80. Plotting the $^{87}Sr/^{86}Sr$ and ε_{Nd} measurements against literature values from terrigenous, coastal, and marine sediments from the Aegean Sea region (Weldeab et al., 2002) reveals an isotopic similarity between the Sahara dust and of sample PM16 with these sediments (Figure 9). A reasonable interpretation of this observation comes from the fact that basal sample PM16 resembles more the soil regolith and plots close to the contemporary and Holocene values of Aegean Sea terrestrial, coastal and marine sediments. The $^{87}Sr/^{86}Sr$ values representing the PM soil regolith show similar values with the Aegean Sea terrestrial and marine sediments and likely represent a mix of Sahara dust with Mesozoic and Cenozoic bedrock carbonates, which are overall characterized by low $^{87}Sr/^{86}Sr$ values of <0.70800 (Capo et al., 1998;

Frank et al., 2021). The two subclusters of PM soil samples have more radiogenic values compared with those of the rest of the samples and clearly correspond to Bw and Bt horizons. The increasing silt contents towards the surface of the PM soil profile (Figure 6, Table 1) occur with $^{87}Sr/^{86}Sr$ and ε_{Nd} values towards more crustal values (color variation in Figure 9) that are representative of the central Sahara province. Therefore, the increases in the silt fraction within the PM soil profile can be directly linked to increases in Sahara dust accretion. This is further supported by range of the silt fraction mean grain size between 14 and 30 µm (Table 1), which is similar to those for modern Sahara dust deposits from Crete, which range 4–8 µm and 16–30 µm (Mattson and Niéhlen, 1996; Goudie and Middleton, 2001). In terms of Sahara dust provenance fingerprinting, the $^{87}Sr/^{86}Sr$ and ε_{Nd} values of the PM soil samples fall within the range (1σ) of the central North African dust source area, which broadly involves the Bodele depression (PSA2; Jewell et al., 2021).

5 DISCUSSION

5.1 PM soil parent material

The mineralogical (XRD) analyses, show that calcite is the dominant mineral phase of MK and TZ interbedded sandy sediment and PM basal layers (Figure 7, lower XRD diagrams TZ01 and Table 2 sample PM 16), which in the periglacial environment of Mount Olympus is expected to dissolve slowly (e.g., Gaillardet et al., 2019) and produce an insoluble residue that comprises the PM soil parent material. MacLeod (1980) analyzed the mineral composition of the insoluble residue of carbonates from western Greece and defined a mineralogical suite of quartz, kaolinite, and mica (illite). Kantiranis (2001) studied the carbonate rocks of northwestern Greece and found insoluble residue □1wt.% consisting mainly of micas, quartz, hematite, chlorite, feldspars, and amphibole, whereas the insoluble residue of carbonate basement rocks from Crete also resembles □1 wt.% of the whole rock samples and is composed of a sandy loam matrix rich in quartz, plagioclase (albite), and mica (illite) (Kirsten and Heinrich, 2022). Thus, the dissolution of the local carbonate parent material within the interbedded sediment layers and in the basal layer of PM soil, can release very small quantities of bedrock-derived impurities such as quartz, plagioclase, illite, and kaolinite that are incorporated in the solum, but cannot explain the □30cm thick PM soil mantle and □60cm thickness of the layers interbedded in the scree slopes.

It has also been proposed that clay in terra rossa soils can derive from isovolumetric replacement of calcite to authigenic clays across a metasomatic front, but this mechanism requires significant input of aeolian dust to provide essential elements such as Al, Si, Fe and K for clay formation (Merino and Banerjee, 2008). Even though we did not estimate the dissolution rate of Mount Olympus bedrock metacarbonates and the elemental composition of the insoluble residue, we consider that the fine earth (silt and clay) contents of MK and TZ interbedded layers, which average 10% and 25%, respectively, cannot be derived only by carbonate dissolution and/or by isovolumetric replacement of calcite. Küfmann (2008), Krklec et al. (2022) and Ott et al. (2023) propose carbonate bedrock dissolution rates between □0.23, 0.15 and 0.4 cm/ka respectively, which for the postglacial (12.5 ka BP to present) alpine soil formation on Mount Olympus imply □5 cm of carbonate loss to soil formation, a value too low to explain the observed thickness of MK, TZ, interbedded layers and PM soil as a result of residual clay accumulation alone. Our direct observations of episodic Sahara dust deposition on the snowpack of Mount Olympus (Figure 3) provide undisputable evidence of Sahara dust accretion on PM soil. The relative contribution of local dust from moraines, outwash plains and from silicate bedrock formations in the vicinity of Mount Olympus is estimated in the following section, but irrespective of the relative dust sources (Saharan and local), the high-energy erosive regime of Mount Olympus alpine critical zone intercepts the formation of extensive aeolian dust mantles, like the one found on the stable Plateau of Muses. We thus suggest that the production of silt, and clay in the PM soil basal layer, partly reflects the contribution of mechanically produced sandy and fine earth carbonate debris and its dissolution products, which together with aeolian dust accretion, comprise the parent materials for the PM soil production.

Commented [A21]: Herein we discarded the section L 480-488 of the previous version of the manuscript as we did not have enough evidence to back up our claims of elemental enrichment and secondary clay formation, in agreement with the comments of Reviewer 1.

5.2 Relative contributions of aeolian dust inputs

Studies on terra rossa soils in Greece, with typical bimodal grain size distributions consisting of clay and silt subpopulations with grain size ranges of 2–4 and 10–40 μm, respectively, ascribe the clay fraction, which is rich in illite and kaolinite, to the limestone residue, and the silt fraction, which is made up entirely of quartz, to long-range aeolian transport from variable sources (Russel and Van Andel, 2003). In line with this notion, we considered the quartz wt. % content in the solum, as a proxy for aeolian dust in general and not exclusively of Sahara dust. The rounded shape of quartz grains observed in SEM images (Figure 11D), provides supplementary evidence for the aeolian transport of quartz grains. Furthermore, we consider that the neodymium-derived mass fraction (*f*), solely a proxy of Sahara dust accretion in the PM soil. This is supported by the high statistical correlation between the silt fraction (M3) with the ε_{ND}-derived *f* fraction (R^2= 0.73, P< 0.001) and by the similarity of the grain size ranges between the silt fraction and the modern Sahara dust deposits. The mass fraction (*f*) of Sahara-dust-derived ε_{ND} was calculated based on the highest ε_{Nd} value of sample PM 16 and Aegean Sea sediments (ε_{Nd} = -5.94) and on the lowest value of Sahara dust PSA2 (ε_{Nd} = −13.81) end members. The ε_{Nd} value of Aegean Sea sediments is considered conservative in relation to that of Mount Olympus bedrock due to the mixing of the carbonate bedrock sediments with other sources of silicate bedrock during fluvial transport.

The ε_{ND}-based Sahara dust contributions to the PM soil varies between □35% and □50% (except that of basal sample PM16) (Figure 10). Conversely, the quartz-derived aeolian dust contribution ranges between □45% and 65%, shows a relatively small variation with depth and an abrupt increase (□25%) from sample PM16 to PM15 (Figure 10). The basal sample PM16 exhibits the lowest contributions of quartz concentration, *f* ratio values (Figure 10) and silt concentrations (Table 1, Figure 6) and is considered an outlier representing the regolith-PM soil mix, which agrees with its distinct color and lowest magnetic susceptibility values. The preservation of quartz in the PM soil profile and especially in the lower Bt horizon requires a mechanism of reduced Sahara dust input and/or loss to weathering, with simultaneous inputs of other quartz-rich-derived dust. A pattern that can explain the lower ε_{Nd}-based Sahara dust contributions in the Bt horizon and the near steady quartz contents is a shift in atmospheric circulation patterns that resulted in less-frequent dust transport episodes from north Africa along with steady aeolian quartz accretion from local quartz sources. Aeolian quartz from the silicate bedrock formations of the Pieria mountains, Mount Olympus granites and even from the Katerini alluvial plane (Figure 1) can be deposited on Mount Olympus periglacial zone during periods of regional aridity, associated with thinning of vegetation, desiccation of the Katerini alluvial plane, and immobilization of fine dust grains through convection.

Based on the above, we tentatively attribute the □15% difference between the ε_{Nd}-based estimates and the quartz-based estimates to accretion of quartz-rich dust from local sources during the formation of the Bt horizon, considering that the contribution of bedrock derived quartz from the insoluble residue is □1%. From the ε_{Nd}-based contributions, we estimate that the Sahara dust accretion to PM soil is between □35% to 50%, whereas local sources can potentially accrete another □15%. Our estimated aeolian dust accretion □65% is similar to the one in the North Calcareous Alps, where the local contribution of dust from the periglacial zone of the North Calcareous and Austrian silicate Alps is significant (Küfmann 2008), but our estimated Sahara dust contribution in the PM soil is higher than its respective average contribution (20 – 30%, Varga et al., 2016) in interglacial soils of the Carpathian Basin. We attribute this difference to the closer proximity of Mount Olympus to Sahara Desert than the Carpathian basin. Given that these values are conservative estimates, the aeolian contribution may potentially be higher as, in our calculations, we have not included aeolian transported micas, feldspars, and clays that are integral parts of Sahara dust samples deposited on the snowpack. We thus suggest that the aeolian dust accretion comprises a minimum of □65% of the PM soil parent material and that carbonate bedrock erosion, and pedogenetic production of detrital clays can potentially contribute another □35% to the development of PM soil.

5.3 Pedogenetic alterations

An alternative mechanism that can explain the nearly homogeneous depth distribution of quartz (Figure 10) is soil mixing by cryoturbation and subsequent translocation of fine earth particles from the upper Bw to the lower Bt horizon. The mechanism of illuviation does not necessarily cancel the climatic forcing of Sahara dust reduction and increase of local dust inputs during the development of Bt horizon, but rather can act synergistically. For example, a cold and arid climatic phase that immobilizes quartz-rich dust from the Mount Olympus and Pieria mountains piedmonts can also reactivate the periglacial processes on the Mount Olympus alpine critical zone, which in turn enhance scree slope aggradation, colluvial activity, intensification of freeze–thaw cycles, and cryoturbation of the soils. Cryogenically induced translocation of detrital (aeolian and bedrock derived) silt and clays deposited on the surface of the Bw horizon, distorts the textural composition and soil properties and results in massive structures like the one we observed in the PM soil profile (Figure 4).

Commented [A22]: We changed the text that cryoturbation can translocate fine particles and not exclusively clays according to the comment of Reviewer 1.

Despite the absence of color difference and of distinct layers in the PM soil, the higher magnetic susceptibility values of the Bt compared to the Bw horizon, can result from the enrichment of ferromagnetic minerals during *in situ* weathering of translocated detrital fine earth particles through pedogenesis (Maher, 2011). However, the overall low values of the frequency dependent magnetic susceptibility (χ_{FD}<10), point to weak pedogenetic alteration of soil (Dearing et al., 1996), which in the base of PM soil profile occurs through the oxidation of ultrafine (titano)magnetite to maghemite (Section 4.4). The SEM-EDS analyses show the presence of ultrafine Fe-Ti grains throughout the solum (Figure 11B) apart from basal sample PM16 (Figure 11A), which is representative of the PM soil regolith. This is further supported from the EDS chemical composition of the calcite grains in basal sample PM 16 that have TiO_2 weight % concentration <1%. On the other hand, magnetite is found attached to clay minerals of the Bodéle depression surface sediments (Moskowitz et al., 2016), which is the major source of Sahara dust in PM soil (Figure 10). Also, magnetic susceptibility measurements of Sahara dust modern deposits in SE Bulgaria show a low frequency magnetic susceptibility value of $\chi_{lf}=97 \times 10^{-8}\ m^3\ kg^{-1}$ (Jordanova et al., 2013), which is close to the values of Bw horizon ($\chi_{lf}=86 \times 10^{-8}\ m^3\ kg^{-1}$) and Sahara dust episodes are known to transport Fe-Ti oxides in the Mediterranean region (Rodriguez-Navarro et al., 2018). We can therefore ascribe the observed Fe-Ti oxides and (titano)magnetite an aeolian origin, from either the local igneous silicate outcrops, or the Sahara Desert. Collectively these observations imply that the magnetic enhancement of Bt compared to Bw horizon can result from a combination of fine earth illuviation of aeolian transported ultrafine magnetic particles from the Bw horizon to the Bt horizon through cryoturbation and subsequent weak pedogenetic modifications that result to the oxidation of magnetic minerals like (titano)magnetite and can also explain the reddish to yellow color hues.

5.4 Mineral weathering

In addition to the weak pedogenesis of ferromagnetic minerals in the base of the PM soil profile, we assessed the mineral weathering potential of non-magnetic minerals through the clay mineralogy composition of basal and topsoil samples PM15 and PM1. Both samples show the dominance of smectite with lesser contributions by kaolinite, chlorite, and illite (Table 2). High amounts of smectite in alpine soils result from the alteration of detrital chlorite and micas deposited on glacier surfaces and are found in proglacial fields in the European Alps and Rocky Mountains (Egli et al., 2003; Egli et al., 2011; Munroe et al., 2015), so that the 20% difference in smectite concentration (Table 2) between the basal and topsoil layers of PM soil can be partly related to enhanced mineral chemical weathering in the base of the solum. Similarly, kaolinite observed in the XRD profiles of the MK, TZ and Sahara dust samples (Figure 7), can be released from the dissolution of bedrock carbonates, as are the cases for western Greece (Macleod, 1980) and Crete (Kirsten and Heinrich, 2022), but can also form through the alteration of other detrital minerals, such as plagioclase (albite), a process that is common in glacial and periglacial environments (Anderson, 2000). Finally, high smectite and

Commented [A23]: We erroneously used a different citation and we correct this. In their work Anderson et al., 2000 emphasize the alteration of plagioclase to kaolinite.

kaolinite contents can also be transported during Saharan dust transport episodes (e.g., Scheuvens et al., 2013), but specifically they are representative of the western Sahara dust provence (PSA 1, Figure 10; Rodriguez-Navarro et al., 2018). However, smectite and kaolinite are also found in modern Sahara dust samples deposited in Athens, Greece (Remoundaki et al., 2011). Therefore, we consider that the high (>80%) concentration of smectite and kaolinite in the PM soil clay (< 2 µm) fraction reflects the balance between direct aeolian deposition and *in-situ* weathering of detrital (aeolian and/or bedrock derived) micas and plagioclase, but the respective contributions of aeolian-transported versus that of bedrock-derived clay minerals subjected to post-depositional mineral alterations cannot be defined from the existing data.

Commented [A24]: The presence of clays in the Sahara Dust samples from the snowpack had not been mentioned in the previous version of the manuscripg and have changed following the comment of Reviewer 1.

5.5 Relative timing of PM soil development

Direct observations suggest that cryoturbation is a fundamental pedogenetic process in the development of PM soil and continues today along with the ongoing accretion of the surficial aeolian silt horizon Bw. The occurrence of seasonal soil freezing and lack of vegetation in the PM polygon centers provide evidence that cryoturbation is active, destroying soil horizonation and obscuring pedogenetic and chemical weathering signals. However, magnetic, and mineralogical data indicate the occurrence of weathered Fe-(Ti) oxides such as (titano)maghemite, and the dominance of smectite and kaolinite in the soil basal and topsoil layers, which enable us to conclude that mineral alteration, and pedogenetic modifications of deposited aeolian dust and local erosional products are ongoing processes within the PM soil profile, occurring in tandem with cryoturbation.

In the absence of absolute datings that can constrain temporally the processes driving the production of PM soil, we hypothesized on its age based on the conclusions drawn from the contributions of aeolian dust, and the impacts of cryoturbation. We tentatively ascribe the deposition of the base colluvial layer and/or the *in-situ* fragmentation of the regolith's till boulders to the most recent period of glacial activity on Mount Olympus. Based on the glacial record of the MK and TZ cirques, the best candidates of periglacial activity that have likely resulted in the deposition of outwash sand and gravels postdate the moraine stabilization phases at □12.5, 2.5, and 0.6 ka BP.

However, there is a 10-ka time span between the Holocene–Pleistocene boundary and the late-Holocene glacial expansions on Mount Olympus. Accepting that PM soil formation began after the moraine stabilization phase at □12.5 ka BP that was common to MK and TZ cirques, its production rate would be □3 x 10^{-5} m yr^{-1} assuming that soil erosion in the low-lying PM has been minimal. This rate is considerably lower than respective soil production rates of Alpine and Mediterranean soils formed over the last 10 ka (Egli et al., 2018; Figure 8). In contrast, by considering a late-Holocene age and that the PM soil development postdates the □2.5 ka BP moraine stabilization phase, the soil production rate is □1 x 10^{-4} m yr^{-1} an estimate that is in better agreement with the soil production rates presented by Egli et al. (2018) for both Alpine and Mediterranean soils. Furthermore, a late-Holocene development of PM soil broadly agrees with soil development patterns in diverse geomorphological environments in Crete (Kirsten and Heinrich, 2022). If this scenario is correct, then we can further hypothesize that development of the Bt horizon could have lasted between □2.5 and 1.0 ka BP, before a recorded phase of intense Sahara dust accretion in Mediterranean that resulted from the combined action of an orbitally induced decrease in solar insolation and of increased aridity over North Africa (Sabatier et al., 2020). This shift could potentially explain the sharp textural boundary between the Bt and Bw horizons and the increasing Sahara dust accretion on the upper Bw horizon. The hypothesized development of the Bw horizon over the past 1 ka could have been disturbed by cryoturbation during the LIA (□0.6 ka BP) glacial expansion in the MK and that continues until today. Ongoing work on Mount Olympus alpine critical zone involves efforts to accurately date the MK and TZ scree interbedded layers and the PM soil profile through Optically Stimulated Luminescence dating that is aided by the high concentrations of quartz in the fine earth fraction, as well as additional geochemical analysis and estimates of the local carbonate bedrock dissolution rates and its residual geochemical composition, in an overall attempt to provide a new continuous record of postglacial alpine landscape evolution in the Mediterranean periglacial zone.

6 CONCLUSIONS

In this study, we investigated the local processes that lead to the development of alpine soils on a stable landform on Mount Olympus, considering its regional setting representative of Mediterranean carbonate mountains that became gradually ice-free during the Pleistocene–Holocene transition but that have also been affected by late-Holocene climatic shifts towards glacial and periglacial conditions (Oliva et al., 2018). We discussed the relative contributions of erosion, aeolian dust accretion, and post-depositional pedogenesis and mineral alteration by comparing colluvial sediment layers interbedded in scree slopes with a soil B horizon developed on a regolith composed by slope outwash deposits and fragmented till boulders along a 2km hillslope energy gradient with a northeasterly orientation, which is the main direction of glacial cirque development on Mount Olympus.

Overall, our results suggest that soils developed in stable landforms like the PM show signs of weak pedogenesis and contain higher amounts of aeolian dust than locally eroded and chemically weathered products. Aeolian dust from local and Saharan sources is accreted in alpine soils formed in periglacial hummocky polygons of the PM and comprises □30%–65% of the soil mass weight. This interpretation matches those of several other studies on aeolian dust accretion in alpine soils (e.g., Gild et al., 2018; Kaüfmann, 2008; Munroe et al., 2015; Yang et al., 2016; Kirsten and Heinrich, 2022) and suggests that aeolian dust is the primary parent soil material on Mount Olympus. The major source of Sahara dust deposited on Mount Olympus is the Bodélé depression, which agrees with observations of accreted dust in Crete (Pye, 1992).

In the low-erosional environment of the PM, mineral alteration and weak pedogenetic modifications occur throughout the solum, but their signal is blurred by soil mixing due to ongoing cryoturbation. A sharp textural boundary not visible in the field separates an upper weathered soil Bw horizon from the lower Bt horizon, which is magnetically enhanced and enriched in smectite and kaolinite. Radiogenic isotope systematics, mineralogy, and magnetic susceptibility value range classify the Bw horizon as an aeolian silt layer that was likely formed during a late-Holocene shift of regional atmospheric circulation that resulted in increased Sahara dust accretion in alpine Mediterranean landscapes.

REFERENCES

Allard, J.L., Hughes, P.D., Woodward, J.C., Fink, D., Simon, K.& Wilcken, K.M. (2020) Late Pleistocene glaciers in Greece: A new ^{36}Cl chronology. *Quaternary Science Rev*iews, 245, 106528. Available from: https://doi.org/10.1016/j.quascirev.2020.106528.

Amit, R., Enzel, Y. & Crouvi, O. (2020) Quaternary influx of proximal coarse-grained dust altered circum-Mediterranean soil productivity and impacted early human culture: *Geology*, 49 (1), 61 – 65. Available from: https://doi.org/10.1130/G47708.1.

Anderson, S.P., Drever, J.I., Frost, C.D., Holden, P., 2000. Chemical weathering in the foreland of a retreating glacier. Geochim. Cosmochim. Acta 64 (7), 1173– 1189.

Capo, R.C., Stewart, B.W. & Chadwick, O.A. (1998) Strontium isotopes as tracers of ecosystem processes: theory and methods. *Geoderma,* 82, 197–225. Available from: https://doi.org/10.1016/S0016-7061(97)00102-X

Castorina, F., Magganas, A., Masi, U. & Kyriakopoulos, K. (2020) Geochemical and Sr-Nd isotopic evidence for petrogenesis and geodynamic setting of Lower-Middle Triassic volcanogenic rocks from central Greece: Implications for the Neotethyan Pindos ocean. *Mineralogy & Petrology,* 114, 39–56. Available from: https://doi.org/10.1007/s00710-019-00687-7.

Conroy, J.L., Overpeck, J.T., Cole, J.E., Liu, KB., Wang, D. Ducea, M.D. 2013. Dust and temperature influences on glaciofluvial sediment deposition in southwestern Tibet during the last millennium. *Global and Planetary Change*, 107, 132-144. https://doi.org/10.1016/j.gloplacha.2013.04.009.

Dearing, J., Hay, K., Baban, S., Huddleston, A., Wellington, E. & Loveland, P. (1996) Magnetic susceptibility of soil: an evaluation of conflicting theories using a national data set. *Geophysical Journal International*, 127, 728–734.

Dobiński, W., 2005. Permafrost of the Carpathian and Balkan Mountains, Eastern and Southeastern Europe. *Permafrost and Periglacial Process*, 16, 395–398.

Drewnik, M., Skiba, M., Szymański, W. & Żyla, M. (2014) Mineral composition vs. soil forming processes in loess soils — A case study from Kraków (Southern Poland), *Catena*, 119, 166 - 173. Available from: http://dx.doi.org/10.1016/j.catena.2014.02.012

Ducea, M. N., Barla, A., Stoica, A. M., Panaiotu, C. & Petrescu, L. (2020) Temporal-geochemical evolution of the Persani volcanic field, eastern Transylvanian Basin (Romania): Implications for slab rollback beneath the SE Carpathians. *Tectonics*, 39e2019TC005802. Available from: https://doi.org/10.1029/2019TC005802

Dunlop, D.J. & Özdemir, Ö. (1997) Rock Magnetism: Fundamentals and Frontiers. Cambridge University Press, Cambridge, New York.

Durn, G., Ottner, F. & Slovenec, D. (1999) Mineralogical and geochemical indicators of the polygenetic nature of terra rossa in Istria, Croatia. *Geoderma,* 91, 125–150.

Durn, G. (2003) Terra rossa in the Mediterranean region: parent materials, composition and origin. *Geolgika Croatia*, 56, 83 – 100.

Egli, M., Mirabella, A. & Fitze, P. (2003) Formation rates of smectites derived from two Holocene chronosequences in the Swiss Alps. *Geoderma,* 117, 81–98.

Egli, M., Wernli, M., Burga, C., Kneisel, C., Mavris, C., Valboa, G., Mirabella, A., Plotze, M. & Haeberli, W. (2011) Fast but spatially scattered smectite-formation in the proglacial area Morteratsch: an evaluation using GIS. *Geoderma,* 164, 11–21.

Egli, M., Dahms, D. & Norton, K. (2014) Soil formation rates on silicate parent material in alpine environments: Different approaches–different results? *Geoderma*, 213, 320 – 333.

Egli, M. & Poulenard, J. (2016) Soils of Mountainous Landscapes. In International Encyclopedia of Geography: People, the Earth, Environment and Technology (eds D. Richardson, N. Castree, M.F. Goodchild, A. Kobayashi, W. Liu and R.A. Marston). Available from: https://doi.org/10.1002/9781118786352.wbieg0197

Egli, M., Hunt, A.G., Dahms, D., Raab, G., Derungs, C., Raimondi, S. & Yu, F. (2018) Prediction of Soil Formation as a Function of Age Using the Percolation Theory Approach. *Frontiers in Environmental Science*, 6, 108. Available from: https://doi.org/10.3389/fenvs.2018.00108.

Erel, Y. & Torrent, J. (2010) Contribution of Saharan dust to Mediterranean soils assessed by sequential extraction and Pb and Sr isotopes. *Chemical Geology,* 275, 19–25. Available from: https://doi.org/10.1016/j.chemgeo.2010.04.007.

Frank, A.B., Frei, R., Triantaphyllou, M., Vassilakis, E., Kristiansen, K. & Frei K.M. (2021) Isotopic range of bioavailable strontium on the Peloponnese peninsula, Greece: A multi-proxy approach. *Science of the Total Environment*, 774, 145181, Available from: https://doi.org/10.1016/j.scitotenv.2021.145181.

Gaillardet, J., Calmels, D., Romero-Mujalli, G., Zakharova, E., Hartmann, J. 2019. Global climate control on carbonate weathering intensity. Chemical Geology, 527, 118762. https://doi.org/10.1016/j.chemgeo.2018.05.009.

Garzanti, E., Andò, S. & Vezzoli, G. (2009) Grain-size dependence of sediment composition and environmental bias in provenance studies. *Earth and Planetary Science Letters*, 277, 3–4, 422-432. Available from: https://doi.org/10.1016/j.epsl.2008.11.007.

Gild, C., Geitner, C. & Sanders, D. (2018) Discovery of a landscape-wide drape of late-glacial aeolian silt in the western Northern Calcareous Alps (Austria): First results and implications. *Geomorphology* 301, 39-52. Available from: https://doi.org/10.1016/j.geomorph.2017.10.025.

Goudie, A.S. & Middleton, N.J. (2001) Saharan dust storms: nature and consequences. *Earth Science Reviews*, 56, 179 - 204.

Grousset, F.E. & Biscaye, P.E. (2005) Tracing dust sources and transport patterns using Sr, Nd and Pb isotopes. *Chemical Geol*ogy 222, 149–167. Available from: https://doi.org/10.1016/j.chemgeo.2005.05.006.

Haeberli, W., Hallet, B., Arenson, L., Elconin, R., Humlum, O., Kääb, A., Kaufmann, V., Ladanyi, B., Matsuoka, N., Springman, S. & Vonder Mühl, D. (2006) Permafrost creep and rock glacier dynamics. *Permafrost and Periglacial Processes,* 17, 189-214. Available from: http://doi.org/10.1002/ppp.561.

Jewell, A.M., Drake, N., Crocker, A.J., Bakker, N.L., Kunkelova, T., Bristow, C.S., Cooper, M.J., Milton, J.A., Breeze, P.S. & Wilson, P.A. (2021) Three North African dust source areas and their geochemical fingerprint*. Earth Planetary Science Lett*ers, 554, 116645. Available from: https://doi.org/10.1016/j.epsl.2020.116645.

Jordanova, N., Jordanova, D., Qingsong, L., Pengxiang, H., Petrov, P. & Petrovský, E. (2013) Soil formation and mineralogy of a Rhodic Luvisol — insights from magnetic and geochemical studies. *Global and Planetary Change,* 110, 397–413.

Jordanova, D., Georgieva, B., Jordanova, N., Guyodo, Y. & Lagroix, F. (2022) Holocene palaeoenvironmental conditions in NE Bulgaria uncovered by mineral magnetic and paleomagnetic records of an alluvial soil, *Quaternary International*, 631, 47-58. https://doi.org/10.1016/j.quaint.2022.06.009.

Kantiranis N. (2001) Calcination study of the crystalline limestone from Agios Panteleimonas, Florina, Greece. PhD Thesis, School of Geology, Aristotle University of Thessaloniki, 196p.

Küfmann, C. (2008) Are cambisols in alpine karst Autochthonous or eolian in origin*? Arctic Antarctic and Alpine Research*, 40, 506–518.

Kirsten, F. & Heinrich, J. (2022) Soil-sediment-configurations on slopes of Central and Western Crete (Greece) and their implications for late Holocene morphodynamics and pedogenesis – A conceptual approach, *Catena*, 214, 106238, 0341-8162. Available from: https://doi.org/10.1016/j.catena.2022.106238.

Krklec, K., Braucher, R., Perica, D. & Domínguez-Villar, D. (2022) Long-term denudation rate of karstic North Dalmatian Plain (Croatia) calculated from ^{36}Cl cosmogenic nuclides. *Geomorphology*, 413, 108358. https://doi.org/10.1016/j.geomorph.2022.108358.

Kuhlemann, J., Rohling, E., Krumrei, I., Kubik, P., Ivy-Ochs, S. & Kucera, M. (2008) Regional synthesis of Mediterranean atmospheric circulation during the last glacial maximum. *Science,* 321 (5894), 1338 – 1340.

Kurtz, A.C., Derry, L.A. & Chadwick, O.A. (2001) Accretion of Asian dust to Hawaiian soils; isotopic, elemental, and mineral mass balances. *Geochimica Cosmochimica Acta,* 65, 1971–1983.

Lawrence, C.R., Reynolds, R.L., Ketterer, M.E. & Neff, J.C. (2013) Aeolian controls of soil geochemistry and weathering fluxes in high-elevation ecosystems of the Rocky Mountains, Colorado. *Geochimica Cosmochimica Acta,* 107, 27–46.

Lehmkuhl, F., Nett, J.J., Pötter, S., Schulte, P., Sprafke, T., Jary, Z., Antoine, P., Wacha, L., Wolf, D., Zerboni, A., Hošek, J., Marković, S.B., Obreht, I., Sümegi, P., Veres, D., Zeeden, C., Boemke, B., Schaubert, V., Viehweger, J. & Hambach, U.(2020)Loess landscapes of Europe - mapping, geomorphology, and zonal differentiation. *Earth Science Reviews*, 215, 103496. Available from: https://doi:10.1016/j.earscirev.2020.103496.

Lutterotti L., Bortolotti M., Ischia G., Lonardelli I. & Wenk H.R. (2007) Rietvelt texture analysis from diffraction images. *Zeitschrift für Kristallographie*, 26, 125-130.

Maher, B.A. (2011) The magnetic properties of Quaternary aeolian dusts and sediments, and their palaeoclimatic significance. *Aeolian Research,* 3, 87–144.

Marmureanu, L., Marin, C.A., Andrei, S., Antonescu, B., Ene, D., Boldeanu, M., Vasilescu, J., Vitelaru, C., Cadar, O. & Levei, E. (2019) Orange snow: a Saharan dust intrusion over Romania during winter conditions. *Remote Se*nsing, 11, 2466. Available from: https://doi.org/10.3390/rs11212466.

Mattsson, J.O. & Nihlén, T. (1996) The transport of Saharan dust to southern Europe: a scenario. *Journal of Arid Envirnonments,* 32 (2), 111–119. Available from: https://doi.org/10.1006/jare.1996.0011.

Macleod, D.A. (1980) The origin of the red Mediterranean soils in Epirus. Greece. *European Journal of Soil Science,* 31 (1), 125–136.

Merino, E. & Banerjee, A. (2008) Terra rossa genesis, implications for karst, and eolian dust: a geodynamic thread*. Journal of Geology,* 116, 62 – 75.

Moskowitz, B.M., Reynolds, R.L., Goldstein, H.L., Berquó, T.S., Kokaly, R.F. & Bristow, C.S. (2016) Iron oxide minerals in dust-source sediments from the Bodélé Depression, Chad: Implications for radiative properties and Fe bioavailability of dust plumes from the Sahara. *Aeolian Research*, 22, 93-106, Available from: https://doi.org/10.1016/j.aeolia.2016.07.001.

Muhs, D.R. & Benedict, J.B. (2006) Eolian additions to late Quaternary alpine soils, Indian Peaks Wilderness Area, Colorado Front Range. *Arctic Antarctic and Alpine Research*, 38, 120–130.

Munroe, J.S., Attwood, E.C., O'Keefe, S.S. & Quackenbush, P.J. (2015) Eolian deposition in the alpine zone of the Uinta Mountains, Utah, USA. *Catena* 124, 119–129.

Munroe, J.S., Norris, E.D., Carling, G.T., Beard, B.L., Satkoski, A.M. & Liu, L. (2019) Isotope fingerprinting reveals western North American sources of modern dust in the Uinta Mountains, Utah, USA. *Aeolian Research*, 38, 39-47. Available from: https://doi.org/10.1016/j.aeolia.2019.03.005.

Oliva, M., Žebre, M., Guglielmin, M., Hughes, P.D., Çiner, A., Vieira, G., Bodin, X., Andrés, N., Colucci, R.R., García-Hernández, C., Mora, C., Nofre, J., Palacios, D., Pérez-Alberti, A., Ribolini, A., Ruiz-Fernández, J., Sarıkaya, M.A., Serrano, E., Urdea, P., Valcárcel, M., Woodward, J.C. & Yıldırım, C. (2018) Permafrost conditions in the Mediterranean region since the Last Glaciation, *Earth Science Reviews*, 185, 397-436, Available from: https://doi.org/10.1016/j.earscirev.2018.06.018.

Ott, R. F., Gallen, S. F. & Helman, D. (2023) Erosion and weathering in carbonate regions reveal climatic and tectonic drivers of carbonate landscape evolution, EGUsphere [preprint], Available from: https://doi.org/10.5194/egusphere-2022-1376.

Pye, K. (1992) Aeolian dust transport and deposition over Crete and adjacent parts of the Mediterranean sea. *Earth Surface Processes and Landforms,* 17, 271–288. Available from: https://doi.org/10.1002/esp.3290170306.

Rellini, I., Trombino, L., Firpo, M. & Rossi, P.M. (2009) Extending westward the loess basin between the Alps and the Mediterranean region: micromorphological and mineralogical evidence from the northern scope of the Ligurian Alps, Northern Italy. *Geografia Fisica Dinamica Quaternaria,* 32, 103–116.

Remoundaki, E., Bourliva, A., Kokkalis, P., Mamouri, R.E., Papayannis, A., Grigoratos, T., Samara, C., Tsezos, M. (2011) PM10 composition during an intense Saharan dust transport event over Athens (Greece). Science of The Total Environment, 409, 20,4361-4372. Available from: https://doi.org/10.1016/j.scitotenv.2011.06.026.

Rodriguez-Navarro, C., di Lorenzo, F. & Elert, K. (2018) Mineralogy and physicochemical features of Saharan dust wet deposited in the Iberian Peninsula during an extreme red rain event, *Atmospheric Chemistry and Physics* 18, 10089–10122. Available from: https://doi.org/10.5194/acp-18-10089-2018.

Runnels, C. & van Andel, T.J. (2003) The early stone age of the nomos of Preveza: landscape and settlement. In Landscape Archaeology in Southern Epirus, Greece, Vol. I, Wiseman J, Zachos K (eds). *Hesperia Supplement,* 32, 47–13.

Sabatier, P., Nicolle, M., Piot, C., Colin, C., Debret, M., Swingedouw, D., Perrette, Y., Bellingery, M.S., Chazeau, B., Develle, A.L., Leblanc, M., Skonieczny, C., Copard, Y., Reyss, J.L., Malet, E., Jouffroy-Bapicot, I., Kelner, M., Poulenard, J., Didier, J., Arnaud, F. & Vannière, B. (2020) Past African dust inputs in the western Mediterranean area controlled by the complex interaction between the Intertropical Convergence Zone, the North Atlantic Oscillation, and total solar irradiance. *Climate of the Past.* 16 283–298. Available from: https://doi.org/10.5194/cp-16-283-2020.

Sanders, D., Ostermann, M. & Kramers, J. (2010) Meteoric diagenesis of Quaternary carbonate rocky talus slope successions (Northern Calcareous Alps, Austria). *Facies,* 56, 27–46.

Šarić, K., Cvetković, V.,Romer, R.L., Christofides, G. & Koroneos, A (2009) Granitoids associated with East Vardar ophiolites (Serbia, F.Y.R. of Macedonia and northern Greece): Origin, evolution and geodynamic significance inferred from major and trace element data and Sr–Nd–Pb isotopes. *Lithos,* 108, 1–4, 131-150. Available from: https://doi.org/10.1016/j.lithos.2008.06.001.

Scheuvens, D., Schütz, L., Kandler, K., Ebert, M. & Weinbruch, S. (2013) Bulk composition of northern African dust and its source sediments – a compilation. *Earth Science Rev*iews, 116, 170–194. Available from: https://doi.org/10.1016/j.earscirev.2012.08.005

Shalev, N., Lazar, B., Halicz, L., Stein, M., Gavrieli, I., Sandler, A. & Segal, I. (2013) Strontium Isotope Fractionation in Soils and Pedogenic Processes. *Procedia Earth and Planetary Science*, 7, 790-793. Available from: https://doi.org/10.1016/j.proeps.2013.03.074.

Statham, I. (1976) A scree slope rockfall model. *Earth Surface Process*es, 1, 43–62.

Stuut, J.B., Smalley, I. & O'Hara-Dhand, K. (2009) Aeolian dust in Europe: African sources and European deposits. *Quaternary International,* 198 (1–2), 234–245. Available from: https://doi.org/10.1016/j.quaint.2008.10.007

Styllas, M.N., Schimmelpfennig, I., Ghilardi, M. & Benedetti. L. (2016) Geomorphologic and paleoclimatic evidence of Holocene glaciation on Mount Olympus, Greece. *The Holocene,* 26 (5), 709–721.

Styllas, M. N., Schimmelpfennig, I., Benedetti, L., Ghilardi, M., Aumaître, G., Bourlès, D. & Keddadouche, K. (2018) Late-glacial and Holocene history of the northeast Mediterranean mountain glaciers – New insights from in situ-produced ^{36}Clbased cosmic ray exposure dating of paleo-glacier deposits on Mount Olympus, Greece, *Quaternary Science Rev*iews, 193, 244–265, Available from: https://doi.org/10.1016/j.quascirev.2018.06.020,2018

Styllas, M.N. & Kaskaoutis, D.G. (2018) Relationship between winter orographic precipitation with synoptic and large-scale atmospheric circulation: the case of Mount Olympus, Greece. *Bulletin of Geological Society of Greece,* 52, 45 – 70.

Styllas M. (2020) Tracing a late Holocene glacial climatic signal from source to sink under intensifying human erosion of eastern Mediterranean landscapes. *Mediterranean Geoscience Reviews* 2, 91–101. Available from: https://doi.org/10.1007/s42990-020-00031-8).

Varga, G., Cserhati, C., Kovacs, J. & Szalai, Z. (2016) Saharan dust deposition in the Carpathian Basin and its possible effects on interglacial soil formation. *Aeolian Research*, 22. Available from: https://doi.org/10.1016/j.aeolia.2016.05.004.

Weldeab, S., Emeis, K-C., Hemleben, C. & Siebel, W. (2002) Provenance of lithogenic surface sediments and pathways of riverine suspended matter in the Eastern Mediterranean Sea: evidence from 143Nd/144Nd and 87Sr/86Sr ratios, *Chemical Geology*, 186, 1–2, 139-149, https://doi.org/10.1016/S0009-2541(01)00415-6.

Wu, L., Krijgsman, W., Liu, J., Li, C., Wang, R. & Xiao, W. (2020) CFLab: A MATLAB GUI program for decomposing sediment grain size distribution using Weibull functions. *Sedimentary Geology*, 398, 105590. Available from: https://doi.org/10.1016/j.sedgeo.2020.105590.

Yaalon, D.H. (1997) Soils in the Mediterranean region: what makes them different? *Catena*, 28, 157–169. Available from: https://doi.org/10.1016/S0341-8162(96)00035-5.

Yang, F., Zhang, G.L., Yang, F. & Yang, R.M. (2016) Pedogenetic interpretations of particle-size distribution curves for an alpine environment. *Geoderma*, 282, 9–15

FIGURES

Figure 1. (A) General setting of the study area within the Mediterranean basin. (B) Mount Olympus alpine domain that is considered in the study (yellow box), with the two respective piedmonts on the marine and continental sides, the adjacent Pieria Mountains and Katerini alluvial plane (SRTM 90 DEM Model). (C) The highest cirques and plateau of Mount Olympus with the respective locations of dated moraines (black curved lines from Styllas et al., 2018), the sampling locations considered in this study (yellow circles) and the geomorphological transects described in Figure 2 (yellow lines). MK: Megala Kazania cirque, TZ: Throne of Zeus cirque, PM: Plateau of Muses.

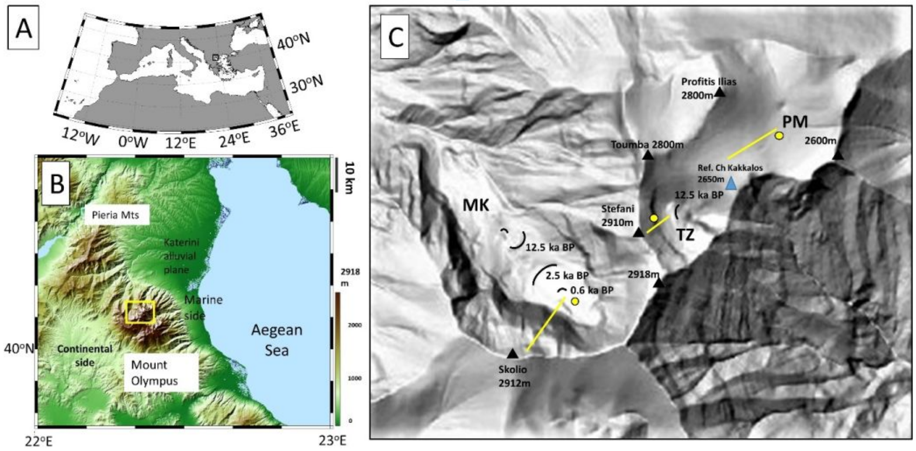

Figure 2. Conceptual diagram of the study, with the sampling sites and their morphological profiles, shown in Figure 1c as yellow lines, and with their respective textural characteristics that resulted from the grain size analysis. The respective heights of the rock cliffs (H_c) and talus slopes (H_t) are shown. The soil samples from the stratified scree clast free horizons in MK cirque are located behind the Little Ice Age moraine (left upper panel, photo, and diagram). The stratified scree slope under the rock wall of Stefani (2910m) in the TZ cirque, with the respective locations of the clast free soil samples (center panel, photo, and diagram) and the soil profile in the PM (right panel, photo, and diagram).

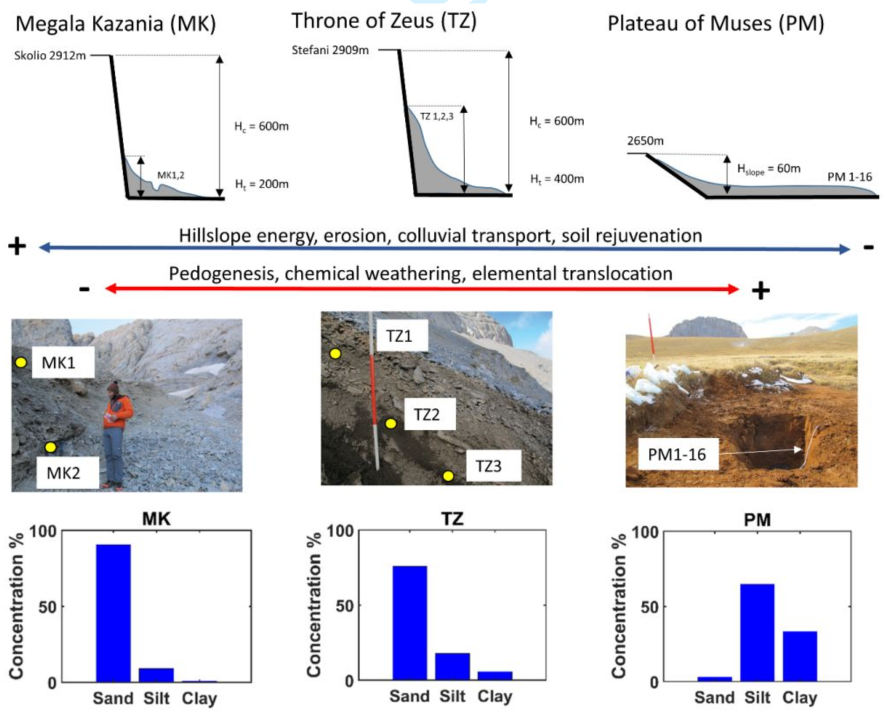

Figure 3. Synoptic maps and direct observations of two Sahara dust episodes on Mount Olympus alpine critical zone (black rectangle). (A). Aerosol Optical Depth (AOD) during March 22, 2018, and (B) and March 16, 2022, showing the trajectory of dust plume from Sahara Desert, and their impacts on the snowpack of the Plateau of Muses (C and D). The PM soil profile was excavated under the black arrow (C), whereas the snow pit (D) with two successive Sahara dust transport episodes in the spring of 2022, has also been excavated on top of the PM soil profile excavated pit. The NASA SUOMI/NNP Aerosol Optical Depth composition product was downloaded from the NASA EOSDIS Worldview platform (worldview.earthdata.nasa.gov).

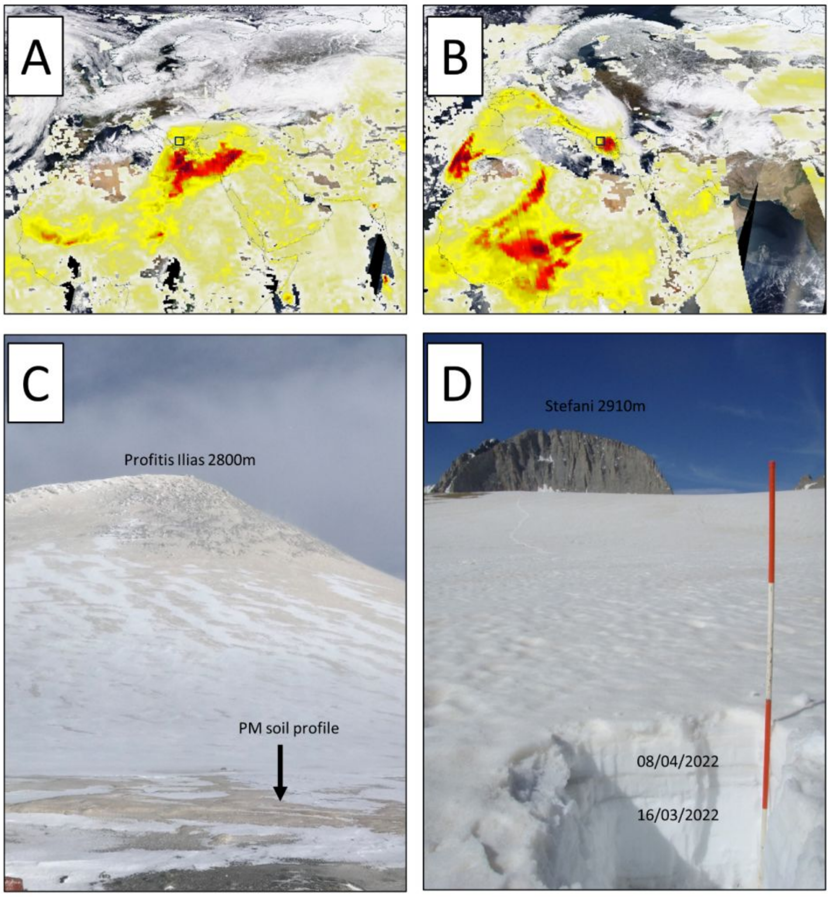

Figure 4. Evidence of soil disturbance on the Plateau of Muses under past and present-day climatic conditions. (A) An irregular gravel layer (blue dashed line) between colluvial gravel and the overlying soil resulting from cryoturbation. (B) Early summer season ongoing freeze of the soil surface layer and subsequent waterlogging (photo taken on June 2012).

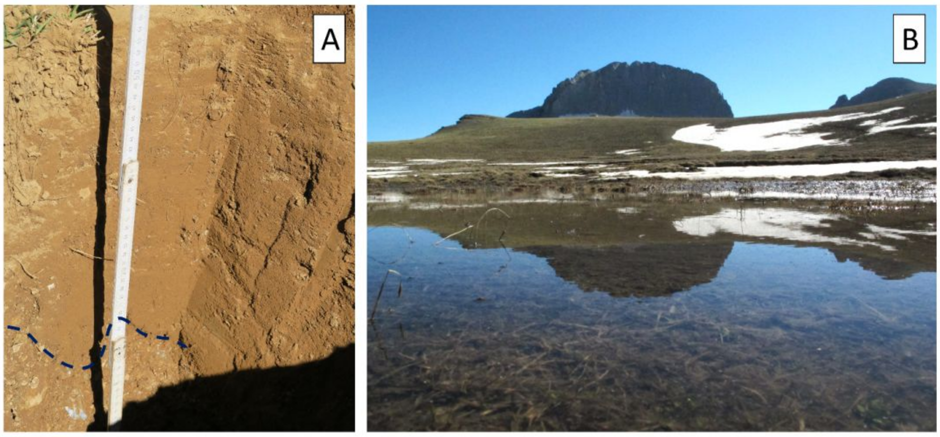

Figure 5. Cumulative grain size distributions of the soil samples from MK, TZ and PM Bw and Bt horizons (A, B, C and D). Surface sample PM1 (A, blue line) shows a distinct grain size distribution from the PM soil upper layer. Subplots E, F, G and H: Results of the CFLab fitting algorithm with the respective grain size distributions (GSD) and extracted grain size modes M1 to M5 (blue curves) of the soil samples PM1, PM15, TZ1 and MK2, represented as distinct sub-populations.

Commented [A25]: We clarify the use of separate grain size modes following the comment of Reviewer 2.

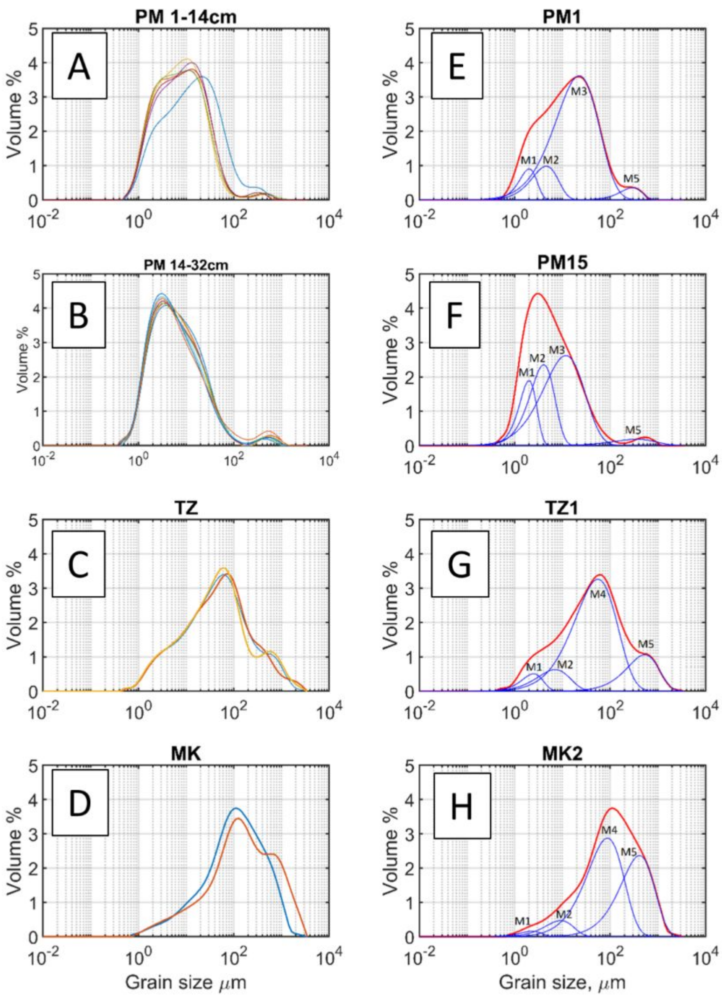

Figure 6. The PM soil profile along with the depth variations main textural classes. A transition layer between 14 and 16 cm of depth marks a substantial decrease in clay and increase in silt contents and a change in the dry soil color. For clarity reasons, it is noted that the direct depth measurement of the PM soil begins at 10 cm along the measurement tape, explaining the discrepancy between the actual and the illustrated depth. The photo was taken one day after the profile excavation, when the upper part had partly dried out.

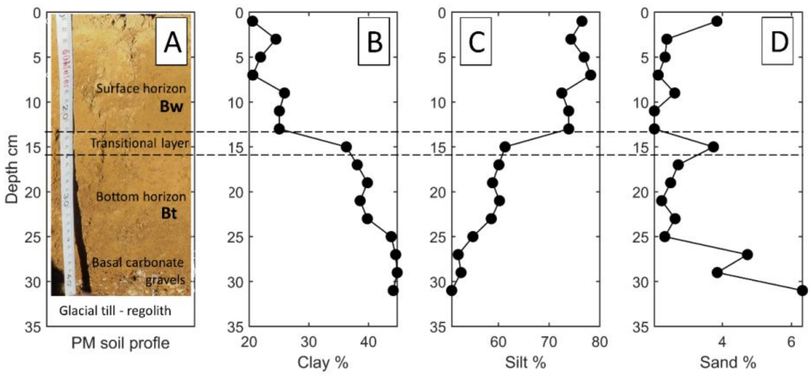

Figure 7. X-ray diffraction patterns of soil samples PM1, PM15, TZ1 and MK2. Soils within the hillslope high energy scree deposits are composed primarily of calcite. In contrast PM soil samples contain quartz, clays, feldspars, and mica. (M: mica, Chl/M: Chlorite and mixed layer clays, likely smectite, Chl/K: chlorite and likely kaolinite, K: K feldspar, Qz: quartz, Pl: plagioclase feldspars, Cc: calcite, Dol: Dolomite).

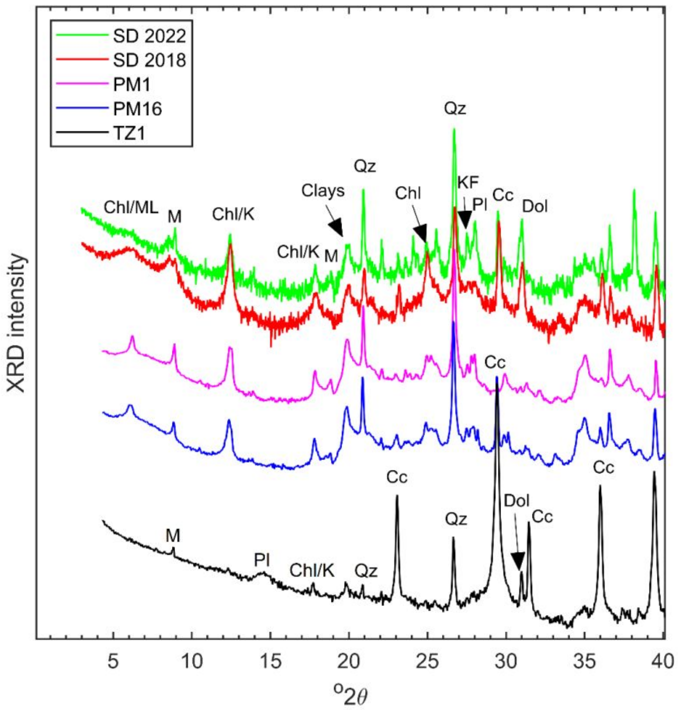

Figure 8. Depth variations of low and high frequency (A) and frequency dependent magnetic susceptibility (B) and (C) thermomagnetic analysis results of sample PM15 (red heating curve, blue cooling curve).

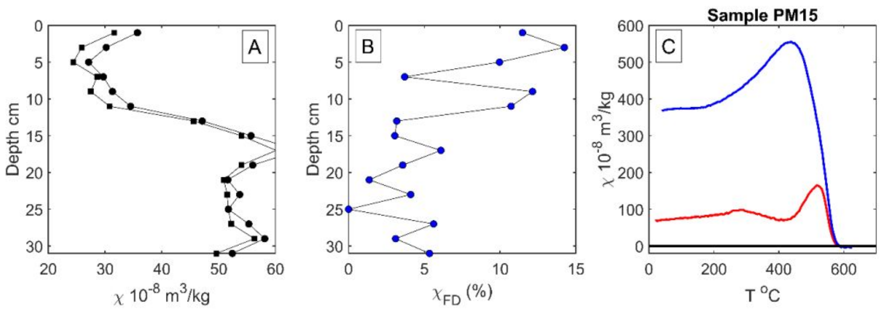

Figure 9. Plot of $^{87}Sr/^{86}Sr$ against ε_{ND} values of the PM soil samples with respective values of Mesozoic and Cretaceous carbonates (Franck et al., 2021), Mount Olympus granites (located on the continental west sides of the massif (Šarić et al., 2009, Castorina et al., 2020), Aegean Sea terrigenous and coastal sediments (Weldeab et al., 2002) and South Aegean marine sediments from Core SL 123 (Ehrmann et al., 2007), along with the three main North African dust source areas (PSA, Jewell et al., 2021). The isotopic enrichment trend for the PM soil samples towards crustal more radiogenic values occurs with a 25% increase in silt contents (colorbar) from the base to the surface of PM soil profile, suggesting the influence of external aeolian dust.

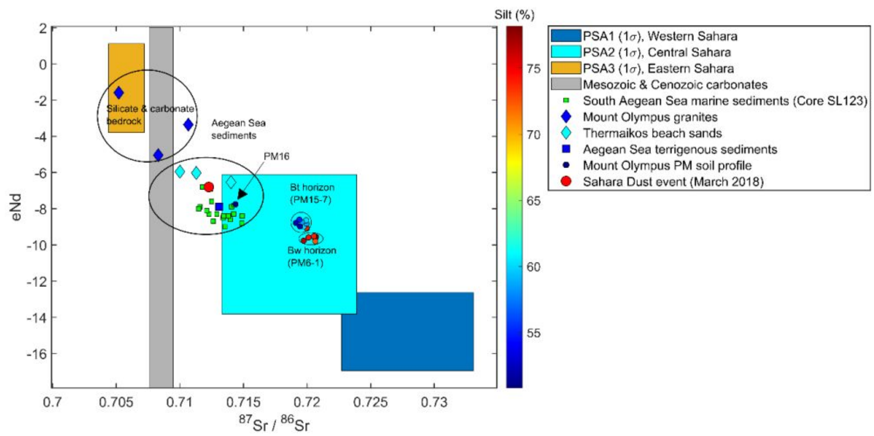

FIGURE 10. Estimates of the relative contributions of aeolian dust accretion to PM soil as calculated by mineralogical, and isotopic proxies.

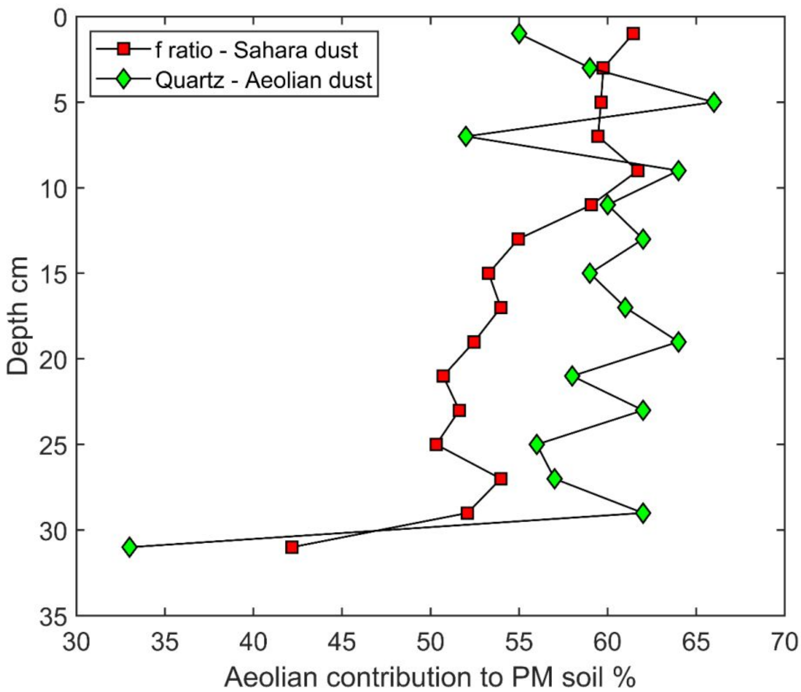

FIGURE 11. SEM backscatter images from selected samples of PM loess profile. (A) Calcite grains from basal sample PM 16. (B) Mixed phase of aluminosilicates with calcite, titanomagnetite and titanite from basal sample PM 16. (C). K-feldspar. (D) Quartz grain with rounded edges as a result of long-range aeolian transport. (E) Surface sample PM1 aggregate of aluminosilicates and Fe-Ti oxides. (F) Quartz grains of variable shapes and grain sizes from sample PM3 along with Fe-Ti oxides.

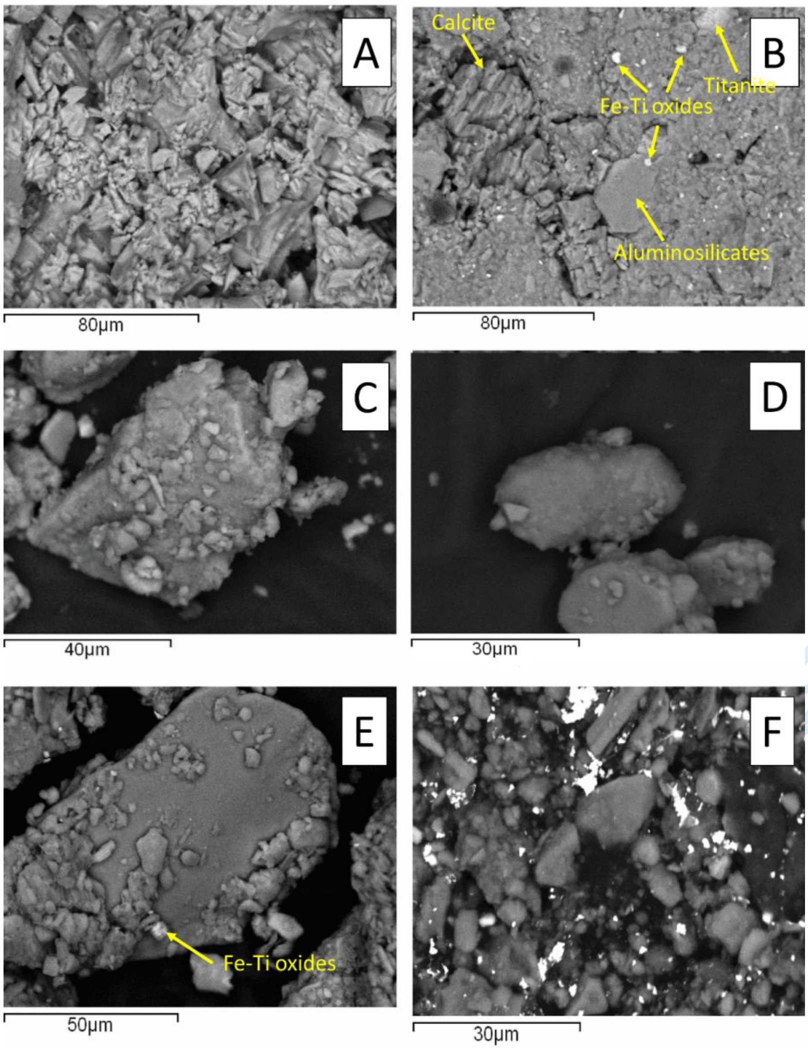

Table 1. Physical characteristics of the soil samples retrieved from the interbedded colluvial soils of the Megala Kazania (MK) and Throne of Zeus (TZ) scree slopes and from the alpine soil formed on the Plateau of Muses (PM).

Sample id	Depth below surface (cm)	Munsell color (dry)	Clay (%) M1 (<2μm)	Fine Silt (%) M2 (3.5-5μm)	Silt (%) M3 (14-30μm)	Fine sand (%) M4 (65-110μm)	Coarse sand (%) M5 (300-800μm)
MK1	30	5Y 6/1	1.7	6.6	0.0	39.8	51.9
MK2	250	5Y 6/1	0.0	11.4	0.0	47.5	41.1
TZ1	50	2.5Y 5/4	5.3	10.0	0.0	67.9	16.8
TZ2	150	10YR 3/4	6.0	25.2	0.0	43.5	25.3
TZ3	120	10YR 3/4	5.8	18.2	0.0	56.9	19.1
PM1	0-2	7.5YR 3/6	7.8	12.7	76.5	0.0	3.0
PM2	2-4	7.5YR 3/6	9.8	14.7	74.5	0.0	1.0
PM3	4-6	7.5YR 3/6	8.5	13.4	76.9	0.0	1.2
PM4	6-8	7.5YR 3/6	8.0	12.6	78.2	0.0	1.2
PM5	8-10	7.5YR 3/6	9.8	16.1	72.5	0.0	1.6
PM6	10-12	7.5YR 2/4	9.3	15.7	73.8	0.0	1.2
PM7	12-14	7.5YR 3/6	9.3	15.7	73.8	0.0	1.2
PM8	14-16	10YR 3/4	13.0	23.3	61.3	0.0	2.4
PM9	16-18	10YR 3/4	13.8	24.2	60.1	0.0	1.9
PM10	18-20	10YR 2/4	14.5	25.2	58.8	0.0	1.5
PM11	20-22	10YR 3/4	14.0	24.5	60.2	0.0	1.3
PM12	22-24	10YR 3/6	14.6	25.1	58.6	0.0	1.7
PM13	24-26	10YR 3/6	16.3	27.5	55.0	0.0	1.2

PM14	26-28	10YR 3/4	16.0	28.5	52.1	0.0	3.4
PM15	28-30	10YR 4/6	16.2	28.6	52.6	0.0	2.6
PM16	30-32	2.5YR 5/6	15.6	28.5	50.8	0.0	5.1

Table 2. Weight percent (wt %) mineralogical semi quantitative composition of the PM soil, along with the clay mineralogy of surface and base samples PM1 and PM15.

Sample id	Qtz	Chl_CC	Plag	KF	Mica	Amph	Cc	Clay mineralogy (<2µm) Sm / Kaol / Chl / Ill
PM1	55	21	14	3	7	0	0	Smectite: 45%, Kaolinite: 35%, Chlorite: 10%, Illite:10%
PM2	59	26	6	1	8	0	0	
PM3	66	21	4	2	7	0	0	
PM4	52	31	7	3	7	0	0	
PM5	64	22	7	0	7	0	0	
PM6	60	24	7	2	7	0	0	
PM7	62	20	4	6	8	0	0	
PM8	59	24	7	3	7	0	0	
PM9	61	24	7	3	5	0	0	
PM10	64	22	8	1	5	0	0	
PM11	58	28	4	3	7	0	0	
PM12	62	22	7	2	7	0	0	
PM13	56	25	5	1	7	6	0	
PM14	57	28	2	7	6	0	0	
PM15	62	24	6	4	4	0	0	Smectite: 65%, Kaolinite: 25%, Chlorite: 5%, Illite:5%
PM16	33	12	1	2	4	0	48	

Table 3. Radiogenic isotope results for the PM soil profile and the 2018 Sahara dust (SD) samples. εND values were calculated

Sample id	$^{87}Sr/^{86}Sr$	$^{87}Sr/^{86}Sr$ std err (%)	$^{143}Nd/^{144}Nd$	$^{143}Nd/^{144}Nd$ std. err. (%)	ε_{ND}
NBS 987 Sr standard	0.7102500	0.0008	-	-	
La Jolla Nd standard	-	-	0.5118500	0.0006	
PM1	0.7197322	0.0008	0.5121292	0.0004	-9.77
PM2	0.7201146	0.0026	0.5121383	0.0006	-9.60
PM3	0.7205816	0.0009	0.5121390	0.0006	-9.58
PM4	0.7207105	0.0010	0.5121399	0.0007	-9.56
PM5	0.7206530	0.0029	0.5121278	0.0009	-9.80
PM6	0.7205393	0.0007	0.5121419	0.0005	-9.52
PM7	0.7199828	0.0008	0.5121641	0.0005	-9.09
PM8	0.7196993	0.0009	0.5121731	0.0006	-8.91
PM9	0.7197594	0.0008	0.5121694	0.0005	-8.98
PM10	0.7199571	0.0007	0.5121775	0.0004	-8.82
PM11	0.7199244	0.0009	0.5121869	0.0006	-8.64
PM12	0.7196162	0.0008	0.5121820	0.0006	-8.74
PM13	0.7193930	0.0008	0.5121890	0.0006	-8.60
PM14	0.7194477	0.0009	0.5121694	0.0005	-8.98
PM15	0.7191162	0.0011	0.5121795	0.0004	-8.79
PM16	0.7143748	0.0016	0.5122328	0.0005	-7.75
SD 2018	0.7122721	0.0009	0.5122813	0.0006	-6.80